Nanoscale Photodetector and Optical Modulator for Future Optical Interconnect Systems

by

Ugo Otuonye

A dissertation submitted in partial fulfillment
of the requirement for the degree of
Doctor of Philosophy
(Electrical Engineering)
in The University of Michigan
2016

Doctoral Committee:

Professor Wei Lu, Chair
Professor L. Jay Guo
Professor Xiaogan Liang
Professor Zhaohui Zhong

Table of Contents

List of figures ... v

Abstract ... x

Chapter 1 ... 1

Overview ... 1

1.1 Physics of photo detection ... 2
1.1.1 Photoconductors ... 4
1.1.2 P-N Junction Photodetectors ... 9
1.1.3 Schottky Junction Photodetector ... 11
1.1.4 Phototransistors ... 13
1.2 Optical Modulators ... 16
1.2.1 Electro-refraction Modulators ... 16
1.2.2 Electro-absorption modulators ... 18
1.2.3 Modulators based on plasma dispersion effect ... 19
1.2.4 Memristor based modulators ... 23

Chapter 2 ... 25

Germanium Nanowire Growth ... 25

2.1 Why Germanium? ... 25
2.2 Ge Nanowire Growth Mechanism ... 27
2.3 Integration of free standing Ge nanowires on silicon substrate ... 28
2.4 Epitaxial growth of Ge nanowires on (111) silicon ... 29
2.4.1 Au nanoparticles adhesion to substrate to enable high growth yield ... 30
2.4.2 Effect of chamber pressure on nanowire growth ... 31
2.4.3 Effect of temperature on nanowire growth ... 31
2.4.4 Effect of nanowire diameter on growth ... 32
2.4.5 Nanowire nucleation and growth ... 32

2.5 Summary 32

Chapter 3 34

Ge nanowire photodetector on silicon substrate 34

3.1 Introduction 34
3.2 Substrate Preparation 34
3.3 Trench Patterning and VLS Growth 35
3.4 Post Growth 36
3.5 Optical Measurement Setup 38
3.6 Ge core nanowires on n-type Si substrate 39
3.6.1 Single nanowire device 39
3.6.2 Array Ge nanowire device results 47
3.6.3 Optical field enhancement around standing nanowires 50
3.6.4 Photocurrent enhancement as a result electron trapping 55
3.6.5 High dark current 56
3.6.6 Nanowire size dependent gain 58
3.6 Ge/Si core/shell nanowire array device 59
3.6.1 High dark current in core/shell nanowire detector 61
3.7 p+Ge/p+Si/Au nanowire array device 63
3.8 Hybrid Schottky Ge/Si heterojunction photodetector 66
3.9 Nanowire solar cell 69
3.10 Effect of Substrate Absorption 71
3.10.1 Substrate Shielding 71
3.10.2 Schottky diode structure 72
3.11 Summary 75

Chapter 4 77

Multi-level memristive optical modulator/encoder 77

4.1 Introduction 77
4.2 Modulator/encoder simulation 81
4.2.1 Grating coupler design 82
4.2.2 Photonic crystal simulation 84

4.3 Modulator/encoder fabrication 87
4.4 Modulator physics 88
4.5 Simulation results of full modulator/encoder 91
4.5.1 Nanoparticle absorption 91
4.5.2 Effect of filament size on modulator response 92
4.5.3 Effect of filament separation on modulator response 94
4.5.4 Effect of photonic crystal waveguide on state decoupling 96
4.7 Electrical and optical measurement 97
4.8 Summary 100

Chapter 5 101

Conclusion and future work 101

5.1 Nanowire photodetector summary 102
5.2 Future work 104
5.2.1 Site controlled nanowire growth 104
5.2.2 Ge nanowire modulator 105

References 106

List of figures

Figure 1: a) Shows a semiconductor material transparent to the incoming photon. No absorption occurrs because Ephoton < Ebandgap. b) Shows absorption process with generation of electron-hole pair and anihalation of the photon.. 3

Figure 2: (a) Schematic diagram of a photoconductor based on the $n+-i-n+$ structure. (b) Band diagram under electrical bias and optical excitation. 5

Figure 3. a) Plot of photocurrent versus excitation intensity for ZnO nanowire (Insert: effect of surface states on optical absorption). b) Photoconductive gain versus absorbed photons. Reprinted with permission from ref[33]. Copyright 2007 American Chemical Society................................ 9

Figure 4. Show the schematic diagram of a p-n junction photodetector. The electron-hole pairs are generated due to optical excitation. The electrons are swept to the n-side while the holes are swept to the p-side. The field is greatest at the junction and band edges bend due to the field [1]....... 10

Figure 5: a) n-type Schottky diode energy band diagram. b) I-V characteristics of silicon based Schottky photodetector. c) Reverse bias I-V curve for NIR wavelengths. d) Responsivity measurement at 1.55um wavelength and 0.1V reverse bias. Reprinted with permission from ref[35]. Copyright 2011 American Chemical Society. 13

Figure 6: (a) Schematic drawing of an n-p-n BJT phototransistor, normally the base width is made very small for higher current gain. (b) Band diagram showing the operation of the of phototransistor and carrier movement under optical excitation.. 15

Figure 7: A Mach-Zehnder interferometric modulator showing enhancement of fundamental mode optical signal from a Y-junction waveguide through constructive interference and an attenuation of the same signal through destructive interference [15]... 17

Figure 8: Modulator based on carrier accumulation at the capacitive plate which changes the refractive index of the material and induces an optical phase shift on the optical beam passing through the waveguide. Reprinted by permission from Macmillan Publishers Ltd: Nature Photonics ref[41], copyright 2010 21

Figure 9: Modulator based on carrier injection into the intrinsic silicon waveguide when the device is forward biased. Reprinted by permission from Macmillan Publishers Ltd: Nature Photonics ref[41], copyright 2010 21

Figure 10: Modulator based on carrier depletion from the p-n junction at the middle of the silicon waveguide when the device is reverse biased. Reprinted by permission from Macmillan Publishers Ltd: Nature Photonics ref[41], copyright 2010 ... 22

Figure 11: a) Schematic drawing showing CB-RRAM device with optical readout. b) Multiple cycling of a CB-RRAM with optical readout. c) On state of CB-RRAM with optical readout showing attenuation of Surface Plasmon Polaritons (SPP) waves. d) Off state with no optical attenuation. Reprinted with permission from ref[44]. Copyright 2013 American Chemical Society. ... 24

Figure 12: Band structure of Germanium showing the direct and indirect bandgaps and the Split-off band [49]. ... 26

Figure 13: An illustration of the Vapor-Liquid-Solid (VLS) process for Ge nanowire growth using gold nanoparticles as catalyst. The eutectic point for this process occurs at 28% Ge content and 361°C [50] ... 27

Figure 14: a) Growth of Ge on silicon substrate beyond the critical thickness which results in dislocation defects. (b) Due to strain relaxation in 1D structures allows for defect free growth of lattice mismatched materials like Ge nanowires grown on Silicon. Reprinted from ref [50]. ... 29

Figure 15: Scanning electron micrograph of Ge nanowires grown in a pattern trench. Aluminum oxide was patterned to define the active area and nanowires were grown using the VLS method. ... 36

Figure 16: Schematic drawing showing the nanowire photodetector fabrication process from initial Au colloid deposition (A) to the last step of nickel deposition (F) ... 37

Figure 17: SEM images for the various fabrication stages. (a) Single nanowire after selective SOG and $Al2O3$ etching (b) Side view of a single nanowire device after Nickel deposition and lift-off process ... 38

Figure 18: Optical setup for photocurrent measurement at 1.55um wavelength. The alignment for the setup was completed using the confocal microscopy. ... 38

Figure 19: (a) Device schematic for single vertical Ge core only nanowire photodetector. (b) Band diagram for Si/Ge p-n heterojunction at no applied bias ... 39

Figure 20: I-V plot of single nanowire photodetector excited at 1.55um with an optical power of 800Mw. ... 40

Figure 21: Plot of photocurrent versus optical power varied from 0W to 0.8W. The photocurrent increased linearly without any observable saturation. ... 42

Figure 22: Pulsed response of photodiode excited with a modulated optical source at 10 KHz and 0.8W optical power. 43

Figure 23: I-V plot of single Ge nanowire photodetector with a marked region showing Io and I at -1V bias. 45

Figure 24: Schematic drawing of nanowire array photodetector. Some of the wires in actual device may be angled instead of vertical........ 47

Figure 25: a) I-V plot of arrays of nanowire photodetector excited at 1.55um with an optical power of 800mW. 48

Figure 26: Plot of photocurrent versus optical power varied from 0W to 0.8W 49

Figure 27: Pulsed response of photodiode excited with a modulated optical source at 10 KHz and 0.8W optical power. 50

Figure 28: (a) 2D plot of electric field along a bare Ge nanowire length (nanowire standing in Si substrate surrounded by air). The input excitation is a plane wave with initial amplitude of 1V/m and excited from the bottom side of the Si substrate. (b) ID plot of electric field along the nanowire length........ 52

Figure 29: (a) 2D plot of electric field along a bare Ge nanowire length (nanowire standing in Si substrate surrounded by air). The input excitation is a plane wave with initial amplitude of 1V/m and excited from the bottom side of the Si substrate. (b) ID plot of electric field along the nanowire length........ 54

Figure 30: (a) Illustration of the band diagram of a core only Ge nanowire clearly showing the p-type behavior due to Fermi level pining close to valance band at the surface. (b) Illustration of light absorption creating electron-hole pairs (c) Schematic showing electron trapping at the surface states and holes being pulled close to the surface due to the effect of field. (d) Complete band diagram showing he p-n heterojunction........ 55

Figure 31: (a) I-V plot from the device simulation for Ge core only structure. (b) Band diagram showing the narrow region from which tunneling could occur. 57

Figure 32: Plot of photoconductivity versus absorbed power density for Ge wires with different diameter. (b) Plot of photoconductive gain versus absorbed power density. Reprinted with permission from ref[63]. Copyright 2010 American Chemical Society. 58

Figure 33: (a) Schematic drawing of core/shell Ge/Si nanowire grown on n-type Si substrate. (b) Band diagram for the core/shell hetero structure. (c) I-V plot of core/shell nanowire in dark and under laser illumination at 1.55um wavelength in log scale (d) I-V plot of core/shell nanowire in dark and under laser illumination at 1.55um wavelength in linear scale. 60

Figure 34: (a) I-V plot showing single Ge nanowire with no shell (red line) and Si shell (blue line). (b) Band diagram of the Ge core/shell nanowire device showing a very narrow barrier at reverse bias of 1V. 62

Figure 35: Schematic showing a possible method of creating a reduced doping region between the Si substrate and core/shell nanowire to reduce tunneling current. (a) Ge core only nanowire is grown. (b) Aluminum oxide is deposited. (c) Part of the aluminum oxide is etched away. (d) Si shell is deposited. 63

Figure 36: (a) Schematic drawing of p-Ge nanowire grown on p+ Si substrate. (b) I-V plot of p-Ge nanowire in dark and under laser illumination at 1.55um wavelength. (b) Band diagram for the p+/p Si/Ge heterojunction with no bias and under positive/negative bias. (d) Band diagram showing the Schottky junction formed between p-Ge and Au top contact. Figures (c) and (d) are Reprinted with permission from ref[52]. Copyright 2013 American Chemical Society. 64

Figure 37: (a) Plot of the band diagram of p+Si/p+Ge/Au device at zero bias. (b) Repeat of the plot of p+Si/p+Ge/Au under -1V bias. Note the Ge/Au contact is biased to –1V while the Si side is grounded. 66

Figure 38: (a) The device schematic with an indication of the multiple junctions formed between the Ge nanowire and the Si substrate and between the Ni and Si substrate. (b) Shows the I-V plot of the hybrid Ge/Ni/Si device in dark and under 1.55um laser excitation. (c) Shows the I-V plot of the Ni/Si schottky device in dark and under 1.55um laser excitation. 67

Figure 39: I-V plot of Si/Ge core/shell nanowire array solar cell. The device shows a short circuit current of 2.66e-4A, open circuit voltage of 0.3V and a fill factor of 30% 70

Figure 40: (a) I-V plot of arrays of nanowire photodetector excited at 1.55um with and without the optical back shield with a beam size of 300um diameter. (b) IR image of a back shielded device showing a 50um by 50um opening through which optical excitation of the active region of the device is carried out. The rest of the substrate is completely shielded and should not have any photon absorption 72

Figure 41: a) I-V plot of Si/Pt Schottky diode in dark and under photo excitation at 1.55um. b) A schematic showing Si/Pt Schottky diode structure. c) Schematic showing band bending due to the formation of Schottky junction and possible carrier absorption mechanisms. 73

Figure 42: Schematic showing the encoding of multiple digital signal channels into optical signals. The encoder is used to directly drive the laser diode producing optically modulated signal. 78

Figure 43: A circuit implementation of a signal summer using an inverting amplifier. The output of the amplifier is the sum of V1, V2 and V3 plus an amplifying factor determined by RfR. 79

Figure 44: Schematic showing a modulating/encoding optical device that operates with multiple electrical input signals. For each combination of the input electrical signals, a discreet optical state is outputted. 80

Figure 45: (a) Schematic of grating coupler. (b) 2D simulation of 2D grating coupler. (c) Output transmission versus wavelength of 2D grating coupler. 83

Figure 46: Band structure of a photonic crystal with a lattice constant of 0.5um, etched hole radius of 0.11um and a slab thickness of 0.12um. 85

Figure 47: (a) SEM image of fabricated Si photonic crystal waveguide. The left side is the input of the waveguide (0.5um wide). (b) Simulation image of the same photonic crystal waveguide. The fundamental mode is clearly well confined to the waveguide path. 86

Figure 48: (a) SEM image after photonic crystal waveguide and memristor fabrication (waveguide input from right). (b) SEM image after the addition of external contacts. (c) Zoomed out image of the full fabricated device. (d) Zoomed out image showing the grating coupler and the output waveguide. 87

Figure 49: 2D plots of field coupling around 5nm particles embedded in a photonic crystal waveguide. The number of nanoparticles range from 1 to 1000. 91

Figure 50: (a) Device schematic showing how the filament size is controlled by the diameter of the silver electrodes. The spacing indicated as "a" corresponds to one lattice length of the photonic crystal. (b)-(f) Plots of the simulated transmitted light through the modulator with respect to wavelength for each of the possible states using a 100nm, 200nm, 300nm, 400nm and 500nm filament sizes. 94

Figure 51: (a), (b), (c) and (d) Plots of transmitted power for different device states (00, 01, 10 and 11) for a filament separation of 1 to 2.5 lattice constant. The 01 and 10 are almost completely coupled for the 1a separation but shows stronger decoupling for the 2a separation. 1a and 2a separations have similar response and the same for 1.5a and 2.5a separations. 95

Figure 52: (a) Schematic of the photo crystal waveguide based device. (b) Schematic of the planar rectangular waveguide simulated device. (c) Plot of transmitted power versus wavelength for the photonic crystal waveguide based memristive modulator/encoder. (d) Plot of transmitted power versus wavelength for a rectangular waveguide based modulator/encoder. 97

Figure 53: (a)-(d) Plot of measure optical output after each set and reset cycle of the memristor. The measured optical output was converted to current output by the photodetector and measured as voltage levels on the oscilloscope. 98

Figure 54: (a) and (c) I-V plot of filament formation for the Memristor which signifies the "01" and "10" state. They show clear hysteresis. (b) I-V plot showing the erase of the two memristor devices. 99

Abstract

Nanoscale Photodetector and Optical Modulator for Future Optical Interconnect Systems

by

Ugo Otuonye

Chair: Prof. Wei Lu

As the demand for cheaper and faster computing continues to increase, the semiconductor industry has relied on transistor scaling to meet this demand. With transistor size approaching the atomic limit, there needs to be a fundamental change from the traditional improvement methods employed in the past. Improvement of data transfer between the microprocessor and other peripheral units could provide an immediate boost to computing in general. The bus lines connecting the CPU to other components are made up of metal interconnects. The speed of metal interconnects are highly limited due to parasitic effects. Switching to optical interconnects will eliminate most of the parasitic effects experienced with metal interconnects and will provide an

immediate improvement in computing speed. Implementation of optical interconnect system will require nanoscale photodetectors and modulators.

At 20nm scale and using a CMOS compatible process, Ge nanowire photodetectors could be integrated at the transistor level for interconnect applications. We have demonstrated a single 20nm diameter Ge nanowire photodetector with current gain of more than 10^3 and responsivity of 25A/W operating at 1.55um wavelength. Our device is based on the formation of an abrupt heterojunction between Ge nanowire and Si substrate. The device photocurrent is highly scalable based on the number of active nanowires connected in a parallel formation.

We have also demonstrated a multilevel modulating device based on the integration of two memristors on a photonic crystal waveguide. Our device enabled the modulation of an optical channel by multiple electrical signals with distinct optical output for every combination of the modulating input signals. The device operation is based on the creation of optical extinction centers within the waveguide through the injection of silver clusters. By using a photonic crystal waveguide instead of traditional waveguide structure to build the device, we exploited the local resonances within the photonic crystal waveguide to tune the waveguide response and optical output characteristics of the device. The demonstrated device operates at the telecommunication wavelength of 1.55um and it is fabricated using CMOS compatible process.

Integration of nanowire photodetector and nanoscale modulator as a single device using CMOS compatible process will potentially enable high-speed and high-density optical interconnect link between the microprocessor and other peripheral units, and provide immediate boost to the speed of computers.

Chapter 1

Overview

As transistor scaling trends towards the sub 20nm gate length, the development of low power nanoscale optical interconnects will be crucial to realize the full potential in terms of speed and overall performance of systems built from such transistors. For example, optical interconnects might be used for communication between circuit blocks within the Central Processing Unit (CPU) or between the CPU and memory. The idea of using optical interconnects instead of metal interconnects has been an area of intense research for the last decade[1]–[13]. This is because optical interconnects are expected to outperform metal based transmission lines because of the lack of parasitic effects that limit the frequency response of the later.

In order to achieve functioning, high-density and high-speed optical interconnect links that could be integrated into a CMOS based platform, the critical components which are photodetectors and modulators must be within the nanoscale. It is also important that such detectors and modulators be very low power devices and be made using CMOS compatible materials and process. While micron scale photodetectors have been very well demonstrated in the past, nanoscale detectors are still early in the developmental stage. Modulators demonstrated so far are in hundreds of micrometer to millimeter scale. The development of efficient nanoscale modulators and detectors will be crucial to the implementation of an on-chip integrated optical interconnect link.

In this chapter, we will review the physics of photodetector devices and modulators. The focus will be on silicon and germanium based devices that are relevant to the research work presented in the thesis. Photoconductors, p-n junction photodiodes, Schottky junction photodiodes and surface plasmon-enhanced detectors are the photodetectors that will be covered in detail. The operation of electro-optic modulators, electro-absorption modulators and memristive modulators will be explained as well.

1.1 Physics of photo detection

Photodetectors are devices that convert optical energy into electrical energy. This is done through the absorption of photons which in turn generates electron-hole pairs that could be collected to generate current in an external circuit. For semiconductor based photodetectors, the absorption of photons is dependent on the band structure of the semiconductor material. Semiconductor materials could be either transparent or opaque to photons of a particular energy. When the energy of the incoming photon is smaller than the bandgap of the semiconductor, the photon is not absorbed and the material could be described as transparent at that photon energy. However, when the incoming photon energy is higher than the bandgap of the material, the photon is absorbed and the material is referred to as opaque to photons of that energy.

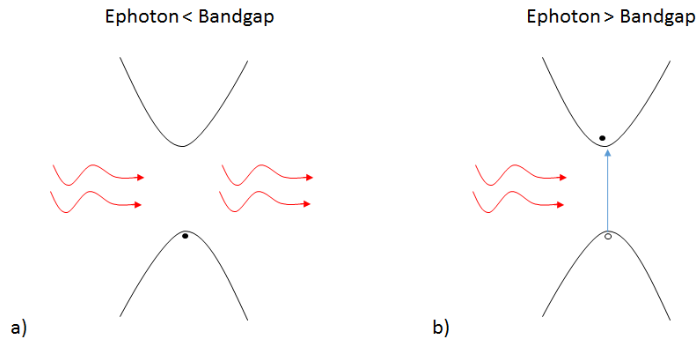

Figure 1: a) Shows a semiconductor material transparent to the incoming photon. No absorption occurrs because Ephoton < Ebandgap. b) Shows absorption process with generation of electron-hole pair and anihalation of the photon.

The idea of absorption is based on the fact that electrons are scattered from the valence band to the conduction band of the semiconductor and creating a hole in the process[14]. However, for these transitions or scattering processes to occur, the energy as well as the momentum must be conserved. It is worth noting that photon momentum is extremely small on the momentum scale[14]. For this reason, scattering process involving photon absorption is more favored when electrons make vertical transitions from valence band to the conduction band. This is more likely to happen in direct bandgap semiconductors (materials where the valence band edge and conduction band edge occur at the same K point). When vertical transitions are not possible because the material is of the indirect bandgap type, optical absorptions can still occur with the assistance of phonons. Due to the momentum required for transitions to occur in indirect bandgap materials, photon absorption is not as efficient as in the case of direct bandgap semiconductors. Most semiconductors fall into two distinct groups, direct and indirect bandgap materials. Few semiconductors like germanium have both direct and indirect bandgap.

For photodetectors to work, both photon absorption and carrier extraction process must be efficient. If photons are absorbed and the photo generated carriers recombine before reaching the contacts, no photocurrent will be measured in the external circuit. In order to ensure effective collection of carrier, photodetectors are electrically biased to produce electric field gradient that separate the carriers (electron-hole pairs) and move them to the contacts. Carriers can also diffuse over short distances without the influence of electric field.

1.1.1 Photoconductors

Photoconductors are the most basic form of semiconductor photodetectors. They are made up of a semiconductor region with two Ohmic contacts. When photons with energy greater than the bandgap of the semiconductor material are incident in the semiconductor region, electron-hole pairs are generated within this region [14]. Under a voltage bias, an electric field is created inside the semiconductor which drives the optically generated electrons and holes to the contacts, creating a photo current which can be detected by an external circuit. A typical example of a photoconductor is the $n^+ - n - n^+$ structure. The n^+ regions help create Ohmic contacts with the intrinsic semiconductor for carrier extraction while the n region is the light absorption layer.

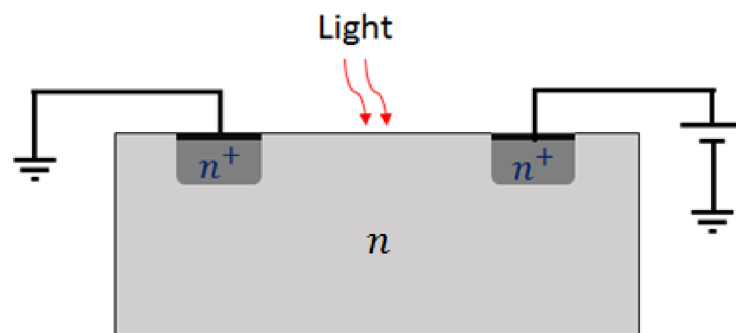

a)

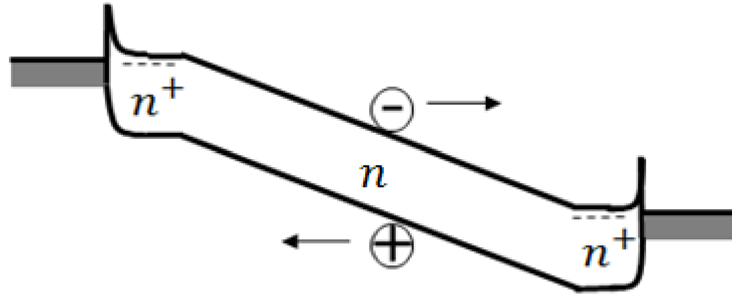

b)

Figure 2: (a) Schematic diagram of a photoconductor based on the $n^+ - i - n^+$ structure. (b) Band diagram under electrical bias and optical excitation.

When light of uniform intensity is incident on the intrinsic region of the photoconductor, the carrier population within this region will increase because of the creation of extra electron-hole pairs from optical absorption. We can represent this change in carrier population with the equation below:

$$n_o + \Delta n \qquad p = p_o + \Delta p \tag{1}$$

$$\Delta n = \Delta p \tag{2}$$

Δn and Δp represent the extra carriers generated from photon absorption and they are equal because electron and hole carriers are created in pairs for each photon absorbed.

The generated carriers will either recombine or be driven by the electric field to the contacts where they are collected. The recombination rate is then given as:

$$R_{eh} = \frac{\Delta n}{\tau_{eh}} = G_L \tag{3}$$

Where

τ_{eh} is the recombination time for the optically generated excess carriers.

If we consider the substrate to be very lightly n-type doped as is usually the case for most photoconductors, the total conductivity of the material will change to account for the generated excess carriers as:

$$\Delta\sigma = q(\mu_n \Delta n + \mu_p \Delta p) = q(\mu_n + \mu_p)\Delta n \quad (4)$$

$$\sigma = q[\mu_n(n + \Delta n) + \mu_p(p + \Delta p)] \quad (5)$$

The current density and photocurrent resulting from the collection of the generated carriers under the influence of the electric field will be:

$$J = (\sigma + \Delta\sigma)E \quad (6)$$

$$I = q\Delta n(\mu_n + \mu_p)AE = qG_L\tau_{eh}(\mu_n + \mu_p)AE \quad (7)$$

Considering that the electron and hole mobility will be different due to the different effective masses of each of these carriers, we can express the photocurrent in terms of transit time and extract a photoconductive gain. Due to the lighter mass of electrons and higher mobility, electron current will dominate because the holes will not have enough time to make it to the contacts before they combined with electrons injected from the contacts [15]. For this reason, we will consider only the transit time of electrons. For a photoactive region defined by length L, the transit time of electrons and the photoconductive gain are defined as

$$t_{tr} = \frac{L}{\mu_n E} \quad (8)$$

$$G_g = \frac{\tau_{eh}}{t_{tr}}(1 + \frac{\mu_p}{\mu_n}) \quad (9)$$

In general, certain figures of merit are used to quantify the performance of photodetectors. Among them are optical generation rate(G_o), quantum efficiency(η), injected photocurrent(I_{ph}), actual photocurrent(I) and responsivity(R). Optical generation rate is defined as the photon flux per unit volume while quantum efficiency is the number of electron-hole pairs produced per absorbed photon (intrinsic quantum efficiency(η_i)) multiplied by the absorbance [2]. The equations for G_o, η, I_{ph}, I, R and photoconductive gain are written as:

$$G_o = \eta(\frac{1}{lA})(\frac{P_{opt}}{\hbar\omega}) \tag{10}$$

$$\eta = \eta_i(1 - R)(1 - e^{-\alpha x}) \tag{11}$$

$$I_{ph} = \eta q \frac{P_{opt}}{\hbar\omega} \tag{12}$$

$$I = I_{ph}\frac{\tau_n}{t_{tr}} \tag{13}$$

$$R = \frac{I}{P_{opt}} \tag{14}$$

$$\text{Photoconductive Gain} = \frac{I}{I_{ph}} = \frac{\tau_n}{t_{tr}} \tag{15}$$

Photoconductive gain is solely dependent on the number of round trips that carriers make before combining with other carriers[15]. Designing the device length in such a way that carriers can make multiple round trips before recombination can lead to very high gain in photoconductors, as discussed below for ZnO nanowire photodetectors and in Section 3.5 for the case of the Ge nanowire photodetector.

As an example, we examine the operation of ZnO nanowire photoconductor which has already been extensively studied. Nanowire photoconductors offer unique properties because of

the one dimensional geometry which allows for very high photoconductive gain and faster photo response compared to two dimensional (2D) and three dimensional (3D) geometries[16]–[20]. The properties of nanowire photoconductors are strongly dependent on the radial diameter of the wires and the effect of surface traps[21]–[27]. The surface traps can cause Fermi level pining and depending on the location of the pining, the nanowire can exhibit n-type or p-type behavior. The charge difference between the surface and the core will lead to significant band bending and for very small geometries (below the critical diameter (d_c)), the wire can be fully depleted[21], [28]–[32]. These effects could cause profound changes to the performance of nanowire photoconductors.

As shown in Figure 3, the photoconductive gain in a ZnO nanowire photoconductor could be as high as 10^8[33]. Such a high gain arises from the long life time of photo generated electrons. As photons are absorbed in the nanowire, electron-hole pairs are generated. Due to the band bending, photo generated electrons are confined to the middle of the nanowire while holes migrate to the surface and are trapped. At low optical generation rates, these electrons can have very long life time since there are no available holes to recombine with, leading to a very high photoconductive gain. However, at very high generation rate, electrons that are closer to the surface can recombine with holes through the trap sites, thereby reducing the photoconductive gain. These effects are evident in the plot of the photoconductive gain versus absorbed photons.

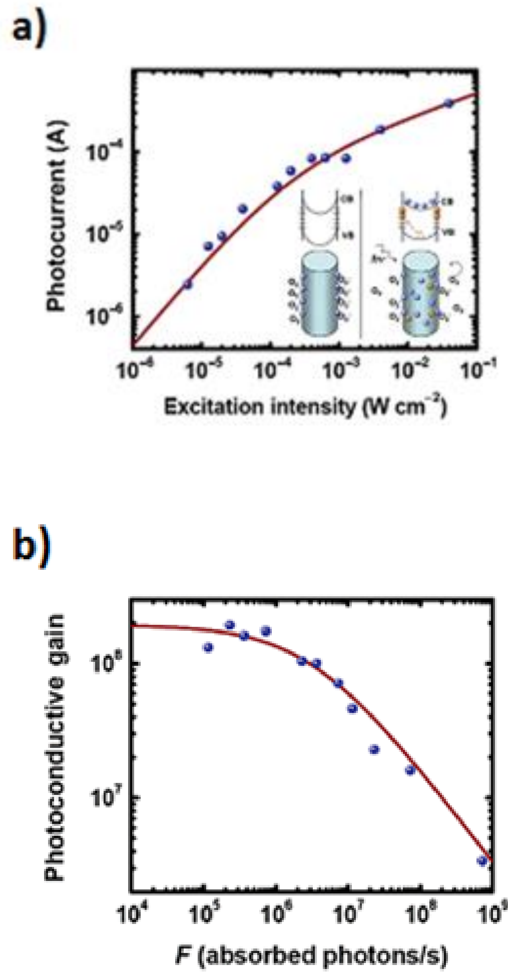

Figure 3. a) Plot of photocurrent versus excitation intensity for ZnO nanowire (Insert: effect of surface states on optical absorption). b) Photoconductive gain versus absorbed photons. Reprinted with permission from ref[33]. Copyright 2007 American Chemical Society.

While photoconductors are important devices mainly due to their easy fabrication, they are prone to very high dark current which limits the signal to noise ratio [14]. Minority carrier recombination time could also limit the speed of photoconductors [14].

1.1.2 P-N Junction Photodetectors

The majority of semiconductor devices are based on p-n junctions. These include Bipolar Junction Transistors (BJTs), metal-oxide semiconductor field-effect transistors (MOSFETs)

homo-junction and heterojunction photodetectors, to name a few. Modifying the barrier height of the p-n junction allows us to change the operating condition of our devices at will. For instance, in MOSFETs, we can create a conducting channel that turns the transistor on by lowering the barrier height at the p-n junctions. Photodetectors based on p-n junction structures offer lots of advantages over the previously discussed photoconductors. Among these are dark current suppression and high frequency operation. The later advantage being the result of reduced junction capacitance which can be achieved by making the junction area small.

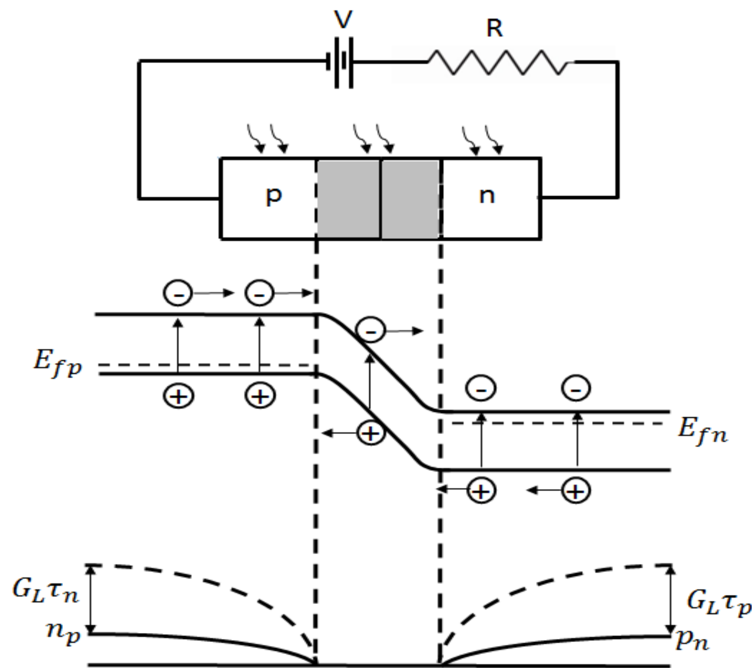

Figure 4. Show the schematic diagram of a p-n junction photodetector. The electron-hole pairs are generated due to optical excitation. The electrons are swept to the n-side while the holes are swept to the p-side. The field is greatest at the junction and band edges bend due to the field [1].

The difference between the p-n photodiode and a regular p-n diode performance is the presence of the extra carriers generated due to the optical absorption within the junction area and one diffusion length away from the junction. The photocurrent arising from generated carriers can be modelled using the equation

$$I_L = eG_L\left(L_p + L_n + W\right)A \qquad (16)$$

Where

L_p and L_n are the diffusion length of the minority carriers, W is the diode depletion width, G_L is the carrier generation rate and A is the effective diode area.

The photocurrent flows in the opposite direction to the forward current of the diode and will have the same sign as the dark current. Modifying the regular diode equation to account for the photocurrent, we can model the total current with the following equation:

$$I = I_L + I_o(1 - e^{\frac{e(V+R_S I)}{nk_B T}}) \qquad (17)$$

Where

I_L is the photocurrent, $I_o$is the dark current, R_s is the series resistance and n is the ideality factor of the diode.

Sometimes it might be necessary to add an intrinsic layer at the p-n junction to enhance optical absorption as is the case with solar cell devices. Devices with such intrinsic layer are referred to as p-i-n photodiodes. The physics of p-n photodiodes and p-i-n photodiodes are very similar. We only need to account for the difference in field profile of added intrinsic layer in p-i-n structures.

1.1.3 Schottky Junction Photodetector

Schottky photodetectors are some of the simplest photodetectors to fabricate. While Schottky junctions behave similarly to p-n junctions in terms of electrical characteristics, the mechanism of operation is quite different. The barrier in Schottky diodes is formed at the metal/semiconductor interface. The height of this barrier is dependent on the metal work function

and varies from metal to metal. In practical Schottky diodes, the barrier height is also dependent on surface states which have the tendency to pin the Fermi level inside the semiconductor bandgap [34]. The Schottky diode current in the forward bias configuration is due to thermionic emission of electrons from the semiconductor into the metal [34]. The current is based on majority carriers unlike p-n junctions which are based on minority carriers.

For photodetector applications, Schottky diodes are operated in the reverse bias configuration just like the p-n photodiodes. There are two mechanisms responsible for the generation of photocurrent. If the energy of the photons is greater than the energy required to overcome the metal-semiconductor barrier ($E_{photons} > E_{\phi_B}$), electrons in the metal gain enough energy to jump over the barrier creating a photocurrent. Also, when the photon energy is greater than the bandgap of the semiconductor ($E_{photon} > E_g$), electron-hole pairs are generated within the semiconductor side of the junction and are separated by the electric field within the junction to contribute to photocurrent. These two detection mechanisms can occur concurrently when the photon energy is greater than both the barrier height and the semiconductor bandgap.

The device characteristics plotted in Figure 5 is for a Schottky junction photodetector built to detect photons with energy higher than the Schottky barrier but lower than the semiconductor bandgap. Photon energy is absorbed by electrons in the metal which enable them to overcome the barrier and get swept by the high junction field into the semiconductor. This device utilizes the strong optical enhancement provided by the coupling of surface plasmon waves on the metal side of the junction to increase the number of electrons excited from the metal into the semiconductor. The tight confinement of light within the Schottky junction in the form of surface plasmons allows the miniaturization of the photodetector making them attractive for integration with other devices.

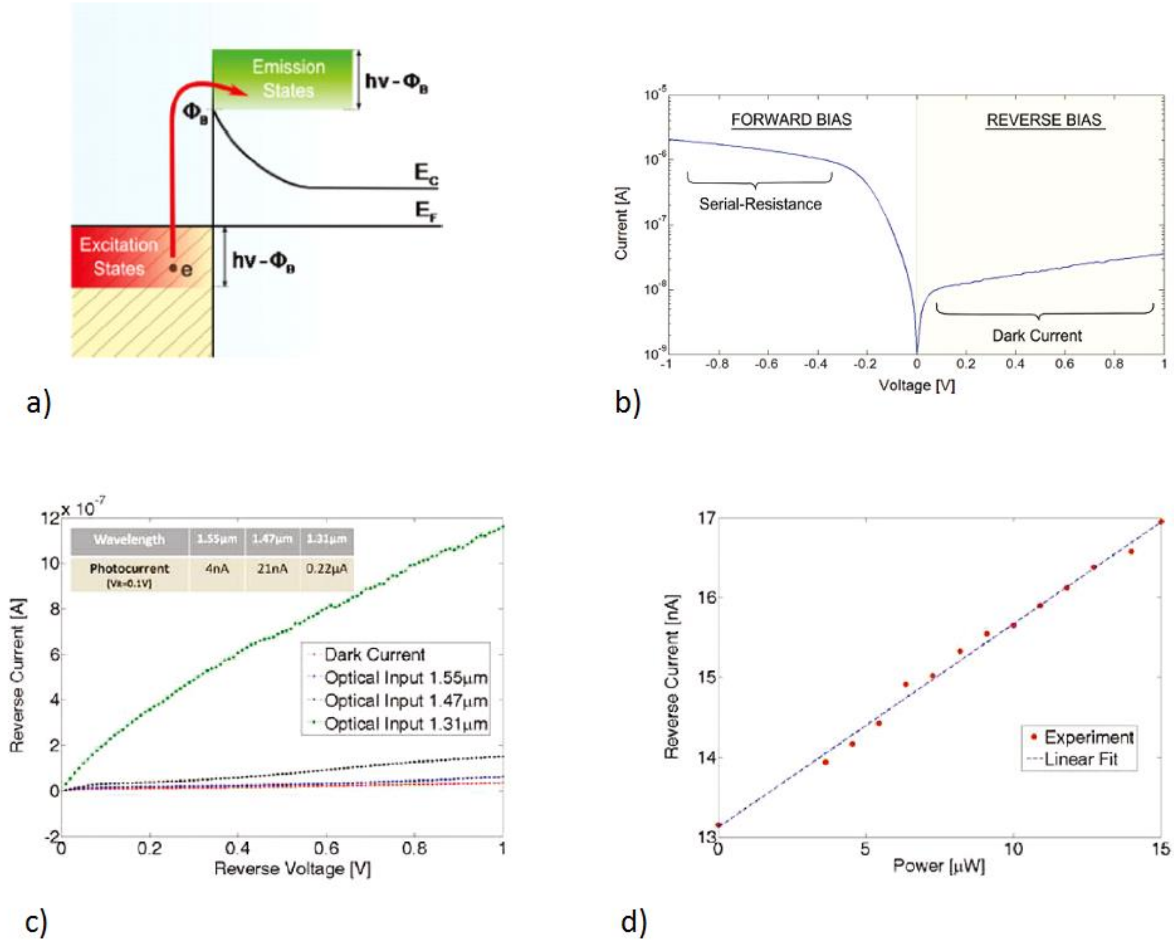

Figure 5: a) n-type Schottky diode energy band diagram. b) I-V characteristics of silicon based Schottky photodetector. c) Reverse bias I-V curve for NIR wavelengths. d) Responsivity measurement at 1.55um wavelength and 0.1V reverse bias. Reprinted with permission from ref[35]. Copyright 2011 American Chemical Society.

1.1.4 Phototransistors

The majority of commercially available phototransistors are made from Bipolar Junction Transistors (BJTs). BJTs are 3 terminal devices consisting of base, collector and emitter regions. For photo detection applications, the base is made up of photosensitive material which absorbs light and produces a photo-induced base current which controls the transistor. Depending on the

biasing mode of the transistor and the gain, the photo-induced base current could be amplified by many orders of magnitude making the phototransistor very sensitive to light.

BJT phototransistors typically have an open circuited base [14]. Most of the photon absorption takes place at the reverse-biased base-collector junction due to the larger depletion width and generate electron-hole pairs. Due to the junction field, electrons are swept to the collector side of the junction (using NPN BJT phototransistor as an example) while holes are swept to the base side. The separation of carriers is responsible for the observed photocurrent just like in regular p-n junction photodetectors. Additionally, the holes injected into the base from the base-collector junction (responsible for the base current) causes more electrons to be injected into the base from the emitter side. The common base current gain (α) in this case will be close to unity. Some of the electrons injected into the base will recombine with holes but the majority of them will make it to the base-collector junction and are swept to the collector side contributing to the overall current. It is easy to observe that in this case the current through the base will be equal to the emitter current since the base is not biased. We can write the transistor equations as follows:

$$\frac{I_E}{I_L} = \frac{1}{1-\alpha} \tag{18}$$

$$I_E = I_C \tag{19}$$

Where

I_E is the emitter current, I_C is the collector current and I_L is the photocurrent.

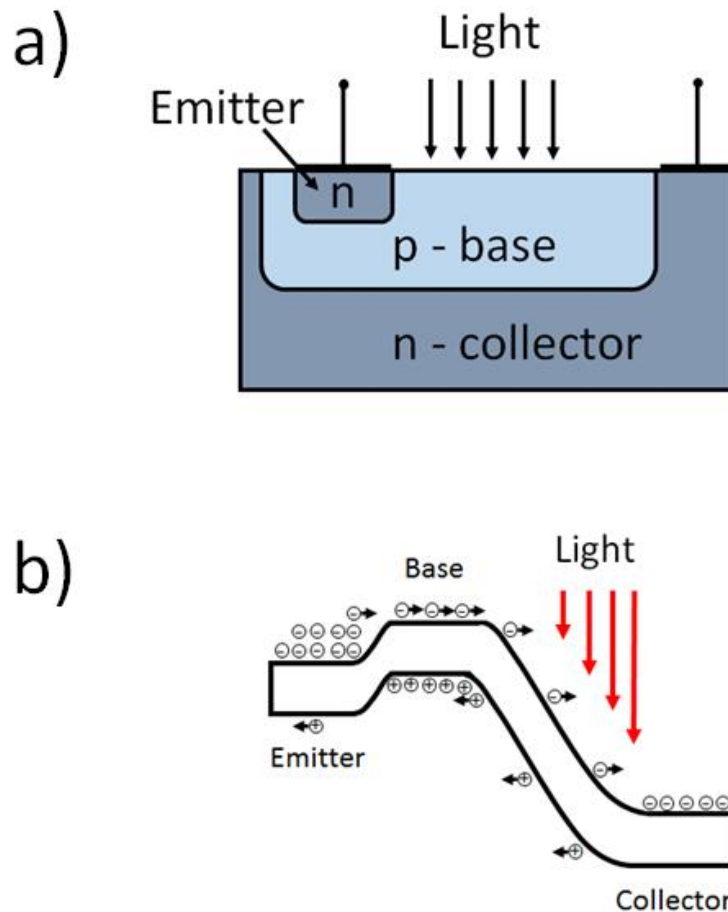

Figure 6: (a) Schematic drawing of an n-p-n BJT phototransistor, normally the base width is made very small for higher current gain. (b) Band diagram showing the operation of the of phototransistor and carrier movement under optical excitation.

When the common base current gain is close to unity the current gain becomes very large. This leads to very high amplification of a small photocurrent making phototransistors very sensitive to light. The speed of phototransistors is limited by large base-collector junction capacitance while the photocurrent is dependent on large base-collector junction. There is a trade-off between speed and photocurrent when designing BJT phototransistors.

1.2 Optical Modulators

In this section, we will review the operation mechanism of different silicon based optical modulators. The majority of optical modulators rely on the applied electric field to alter the refractive index of the semiconductor material [36]. Because the refractive index of most semiconductors are made up of the real and imaginary parts, an applied electric field can change the real part of the refractive index or the imaginary part or both depending on properties of the semiconductor [36], see discussions below. When the real part of the refractive index is changed due to an applied electric field, it is known as electro-refraction. If the imaginary part is changed it is referred to as electro-absorption [36]. Both electro-refraction and electro-absorption effects can be observed in the same device.

1.2.1 Electro-refraction Modulators

Electro-refraction modulators rely on phase shift or change in the polarization of optical beams passing through an applied electric field. The consequent constructive or destructive interference of the phase shifted or polarization changed optical beams produce the modulated output. These types of modulators are described as "Electro-Optic" modulators. The difference in phase or polarization is as a direct result of electric field induced refractive index change. To understand how the refractive index of the material is changed by the applied electric field, we have to recall the electric field relationship to the displacement vector [15], [37], [38], which is given as:

$$D = \varepsilon \cdot E \tag{20}$$

Where

D is the displacement vector, ε is the permittivity tensor and E is the applied electric field (all vector quantities).

The applied electric field changes the permittivity tensor and the permittivity is the square of the refractive index. Further descriptions of electro-optic modulators are based on the physical structure of the devices.

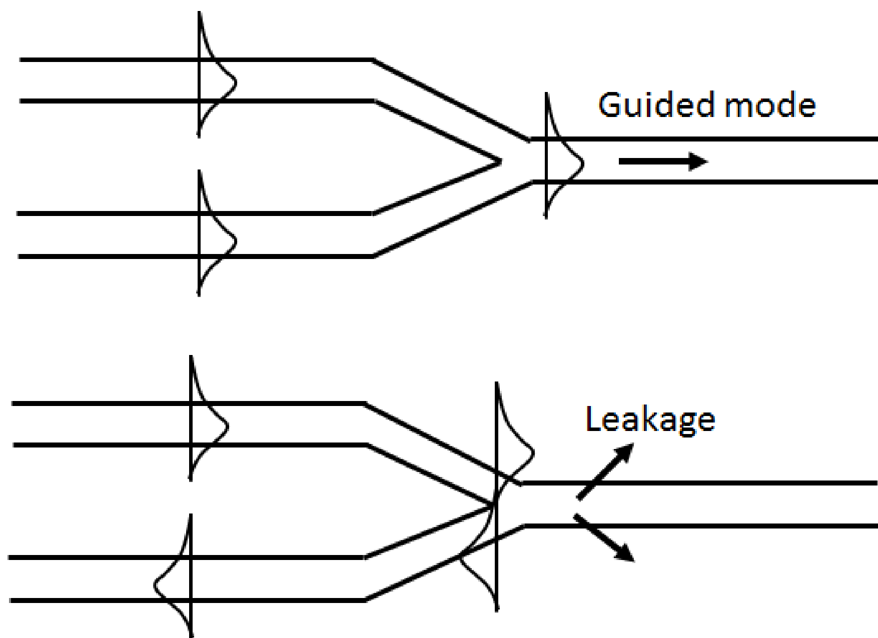

Figure 7: A Mach-Zehnder interferometric modulator showing enhancement of fundamental mode optical signal from a Y-junction waveguide through constructive interference and an attenuation of the same signal through destructive interference [15].

An example of the electro-optic modulator is the Mach-Zehnder interferometer illustrated in Figure 7. An applied electric field from voltage bias alters the refractive index of one of the waveguides thereby causing a 90-degree phase shift relative to the other waveguide. When the optical signals are combined, the phase shift results in a destructive interference of the optical signal. On the alternative, if the signal on the two waveguides are of the same phase, they combine

constructively and enhance the optical signal. To implement this type of modulator, information is encoded into electrical signal as voltage levels. The optical channels are biased to produce phase shift corresponding to the electrical voltage level, thereby encoding the electrical signal into optical signal (light modulation). The operation of the electro-optic modulator is governed by the equation:

$$P_{out} = \frac{1}{4}|e^{i\beta_a l} + e^{i\beta_b l}|^2 = \cos^2(\frac{\Delta\beta l}{2}) \tag{21}$$

Where

P_{out} is the optical power output from the Y-junction and $\Delta\beta l$ is the detuning factor.

1.2.2 Electro-absorption modulators

Electro-absorption modulators are based on the change in the imaginary part of the refractive index of a material due an applied electric field. The absorption mechanism can be due to free carriers or as a result of assisted direct transitions of carriers near the band edges [15][39][40]. The latter case can further be classified into two categories the Franz-Keldysh effect and quantum-confined stark effect (QCSE).

Franz-Keldysh effect is normally observed in bulk direct bandgap semiconductors. The presence of an electric field across a semiconductor material causes band bending in the direction of the field. As a result of this band bending, the wave-function of the conduction band electron and that of valence band hole can penetrate the bandgap, effectively lowering the bandgap of the material [15]. This implies that photons with energy lower than the bandgap of the semiconductor will now be absorbed. By creating two different absorption states in the semiconductor through externally applied electric field, we can effectively modulate an optical signal passing through

such material. The photon energy has to be slightly lower than the bandgap but higher than the absorption tails resulting from Franz-Keldysh effect.

The second effect is the quantum-confined Stark effect (QCSE). This effect is similar to the Franz-Keldysh effect but generally stronger and typically employed in quantum well 2D structures. The absorption is stronger for the QCSE because of the enhanced exciton binding energy in 2D structures due to the confinement of electrons and holes within the wells [15]. Modulators based on QCSE are generally more challenging to achieve due to the additional task of epitaxial material growth of quantum well structures. The Franz-Keldysh effect and QSCE are extensively covered in most photonics texts. For more in depth understanding of these effects, the reader can refer to ref[15].

1.2.3 Modulators based on plasma dispersion effect

At communication wavelengths of 1.3um and 1.55um, silicon is transparent and the electric field effects responsible for both electro-refraction and electro-absorption are extremely weak [41]. Therefore, it is very difficult to achieve good modulation in silicon at these wavelengths. One method that has been used to build efficient silicon modulators is to explore the physics of plasma dispersion effect. This involves the injection of free carriers into a silicon waveguide to change the real and imaginary parts of the refractive index within the local material area [42]. The changes in refractive index as well as absorption resulting from injection and extraction of free carriers were quantified for 1.33um and 1.55 in Ref [43] and started below:

At 1.3um:

$$\Delta n = \Delta n_e + \Delta n_h = -[6.2 \times 10^{-22} \times \Delta n_e + 6 \times 10^{-18} \times (\Delta n_h)^{0.8}] \qquad (22)$$

$$\Delta \alpha = \Delta \alpha_e + \Delta \alpha_h = 6 \times 10^{-18} \times \Delta n_e + 4 \times 10^{-18} \times \Delta n_h \qquad (23)$$

At 1.55um:

$$\Delta n = \Delta n_e + \Delta n_h = -[8.8 \times 10^{-22} \times \Delta n_e + 8.5 \times 10^{-18} \times (\Delta n_h)^{0.8}] \quad (24)$$

$$\Delta \alpha = \Delta \alpha_e + \Delta \alpha_h = 8.5 \times 10^{-18} \times \Delta n_e + 6 \times 10^{-18} \times \Delta n_h \quad (25)$$

Where

Δn_e and Δn_h are changes in refractive index and $\Delta \alpha_e$ and $\Delta \alpha_h$ are changes in absorption due to free electron-hole concentrations.

Next, we will examine three silicon modulating device structures that operate based on plasma dispersion effect. The first device relies on a capacitive structure to accumulate charges which leads to a change in refractive index of the material and subsequent phase shift of the optical beam passing through the material. A thin insulating SiO_2 layer at the middle the waveguide creates a capacitive plate where charges accumulate when electrically biased. The accumulated charges are responsible for the dispersive effect that alter the refractive index of the material and phase shift of the optical beam. An advantage of this modulator is that it can tolerate changes in temperature [41].

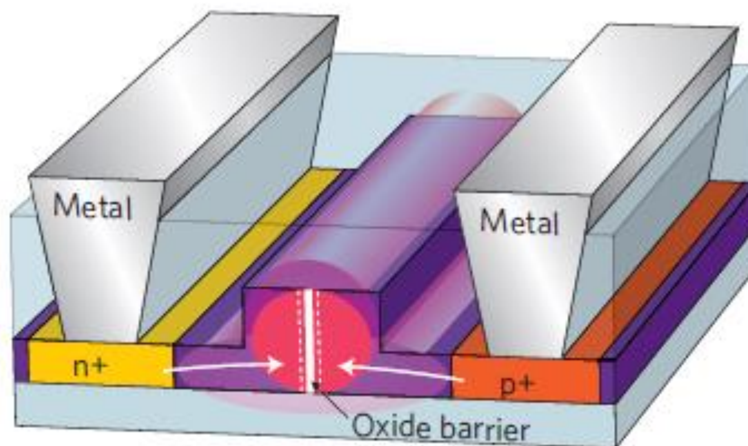

Figure 8: Modulator based on carrier accumulation at the capacitive plate which changes the refractive index of the material and induces an optical phase shift on the optical beam passing through the waveguide. Reprinted by permission from Macmillan Publishers Ltd: Nature Photonics ref[41], copyright 2010

Here we examine a modulator based on carrier injection as an example. The modulator shown in Figure 9 is based on carrier injection into an intrinsic material that forms the waveguide. The modulator has a $p^{+}-i-n^{+}$ structure. When the device is forward biased, carriers are injected into the intrinsic region (the waveguide). The injected carriers are responsible for the dispersive plasma effect that changes the refractive index of the material, causing a phase shift of the optical beam passing through the waveguide. A major drawback of this type of modulator is that it relies on carrier recombination time and drift due to the weak electric field along the channel. If the carrier recombination time is slow as is the case with carriers in an intrinsic silicon, the frequency response of the modulator will be slow.

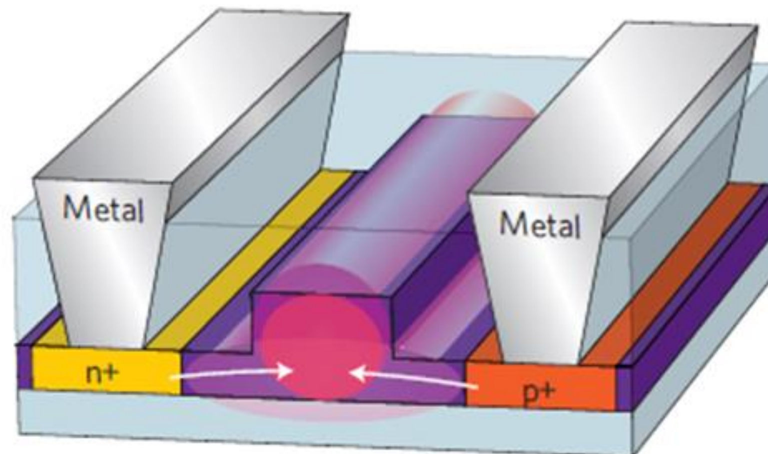

Figure 9: Modulator based on carrier injection into the intrinsic silicon waveguide when the device is forward biased. Reprinted by permission from Macmillan Publishers Ltd: Nature Photonics ref[41], copyright 2010

The last plasma dispersive effect device we will examine is the p-n junction modulator. These type of modulators operate based on carrier depletion rather than accumulation or injection. The operation mechanism is dependent on the expansion of the p-n junction depletion region when the device is reverse biased. Due to the very high field that exist at the depletion region, most of the free carriers are swept away by field. The deficiency of carriers reduces any plasma dispersive effect. By changing the biasing condition of the device from reverse bias to forward bias and vice versa, we can rapidly change the carrier concentration within the waveguide. This type of device can have very fast response because the carriers can be extracted at almost saturation velocity by applying a very high field. However, depending on the device area, junction capacitance can be very high and that could limit the frequency response of the device.

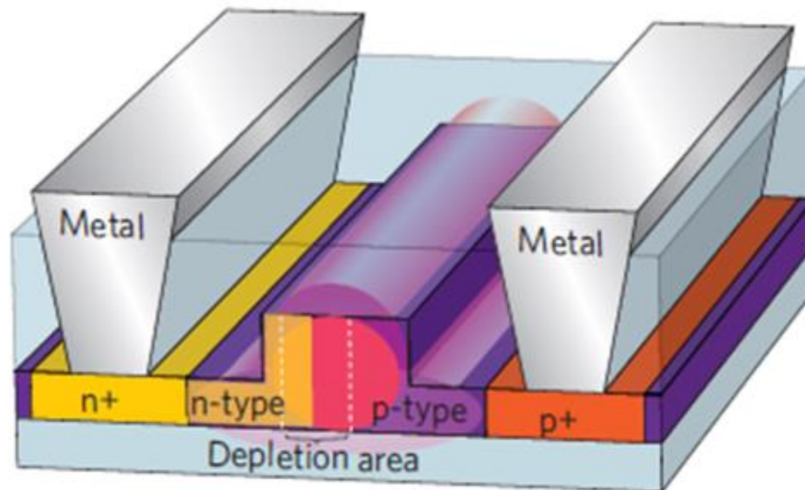

Figure 10: Modulator based on carrier depletion from the p-n junction at the middle of the silicon waveguide when the device is reverse biased. Reprinted by permission from Macmillan Publishers Ltd: Nature Photonics ref[41], copyright 2010

1.2.4 Memristor based modulators

Most of the modulators we have reviewed up to this point rely on the movement of carriers (electrons and holes) or band bending induced by an applied electrical field to change the refractive index or cause plasma dispersive effects. These devices are “volatile” and require the field to be continuously applied to create the desired effects. The memristive modulators work by the movement of ions instead of electrons, and as a result, can offer a memory effect and operate without a constantly supplied field. In this case, the field is only needed when the output signal needs to be changed, and the new output can then be maintained without applied field.

Memristors are nonvolatile memory structures that operate on the principle of electrical switching between high resistance state and low resistance state. The memristor structure typically consists of a top electrode, switching layer and a bottom electrode. For the sample device described in our study, the top electrode is silver (Ag) metal, the switching layer is amorphous silicon (a-Si) and the bottom electrode is heavily doped p-type poly-Silicon. At proper bias conditions, a conducting filament made up of Ag clusters can be formed in the a-Si layer, creating a low resistance between the top Ag and bottom p-Si electrodes. This state is considered the electrical “On” state. At reverse bias, the filament can be removed from the a-Si layer, recovering the device to the electrical “Off” state. These devices are also termed Conductive Bridge Resistive Random Access Memory (CB-RRAM). The Si layers have a dual purpose, they serve as a waveguide and an electrical path for memristive switching. Due to the closely matched refractive index of a-Si and poly-Si, they are optically considered to be one layer.

The device shown on Figure 11, based on this concept, is an optically readable CB-RRAM. The waveguides are a combination of the a-Si and poly-Si layers with a cross section of 280nm by 350nm. The sides of the waveguide are made up of thermally grown oxide layer fabricated using

the local oxidation of silicon (LOCOS) approach. The top electrode is a silver line perpendicular to the waveguide. The operation mechanism of this device is based on the enhancement and attenuation of surface Plasmon coupled light waves.

Light traveling through the waveguide is coupled to the silver (Ag) electrodes as surface plasmon. Ag clusters are then injected into the waveguide by simply forward biasing the CB-RRAM. These Ag clusters destructively interfere with the surface plasmon coupled waves and produce an attenuated signal. When these clusters are extracted back into the contact by reverse biasing the CB-RRAM, the surface plasmon coupling is restored and higher light transmission is restored within the channel. The two sequences needed to modulate the light is the "On" with no filament formed in the waveguide and an "Off" state with filament in the waveguide.

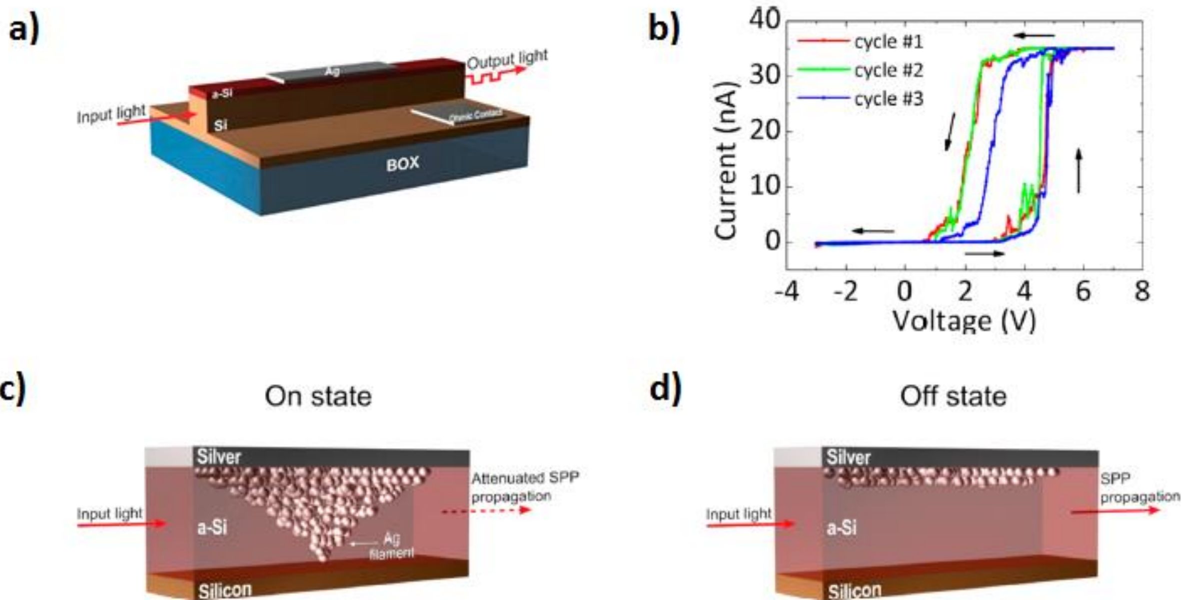

Figure 11: a) Schematic drawing showing CB-RRAM device with optical readout. b) Multiple cycling of a CB-RRAM with optical readout. c) On state of CB-RRAM with optical readout showing attenuation of Surface Plasmon Polaritons (SPP) waves. d) Off state with no optical attenuation. Reprinted with permission from ref[44]. Copyright 2013 American Chemical Society.

Chapter 2

Germanium Nanowire Growth

2.1 Why Germanium?

Germanium is an important semiconductor material due to its electrical and optical properties. In the early stage of the semiconductor industry, it was explored as a candidate material for making transistors. This is because Ge offers higher electron and hole mobility when compared with other materials like Silicon. However, due to the poor quality of Ge oxide (and the higher cost of Ge wafers), Si became the preferred semiconductor material for MOSFETs. Si forms a very good oxide which is needed to form the gate of MOSFETs. Nevertheless, Ge was re-introduced into the semiconductor foundries to improve carrier transport properties by utilizing strain engineering in SiGe source/drain contacts. As a result, Ge is a CMOS compatible material, which makes integration of Ge devices with existing Si devices possible.

In optoelectronics, Ge plays very important roles in applications such as detectors and modulators especially at the optical communication wavelength of 1.55um. Ge has a direct bandgap at 0.8eV and an indirect bandgap at 0.69eV. As a result of this unique band structure, Ge has strong optical absorption, comparable to III-V semiconductors. Ge is being researched as a possible material for mid-infrared detectors due to the separation between the degenerate Heavy Hole (HH)/ Light Hole (LH) band and the split-off band [45]–[48]. The bandgap between the degenerate HH/LH and the split-off band is 0.29eV. This small sub bandgap theoretically extends the detection range of Ge to more than 4um.

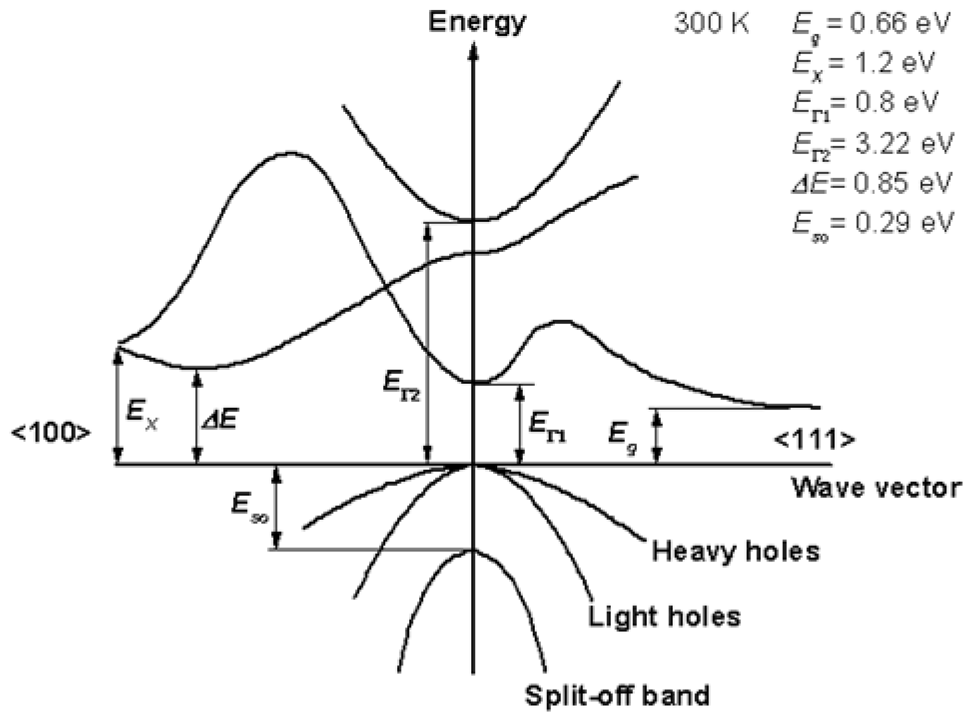

Figure 12: Band structure of Germanium showing the direct and indirect bandgaps and the Split-off band [49].

High quality Ge substrates are expensive to produce. Therefore, it will be more beneficial to integrate Ge devices with existing Si devices. Combining the good optical properties of Ge with the good electrical properties of Si will lead to new novel devices such as nanoscale detectors and modulators. Unfortunately, integration of Ge on Si is not a straight forward process due to the large lattice (4%) mismatch between Ge and Si. The lattice mismatch limits the epitaxial growth of Ge on Si to about 2nm. One method of overcoming this limitation is by growing Ge as 1D structures (nanowires) on Si. Strain relaxation in nanowires allows one to grow epitaxial Ge nanowires on Si and directly build devices on such structures.

2.2 Ge Nanowire Growth Mechanism

There are two main methods of growing semiconductor nanowires in vapor phase (vs. solution phase-based growth). These are the Vapor-Liquid-solid (VLS) and Vapor-Solid-Solid (VSS) methods. The major differences with these methods are the state of the metal nanocluster. Both methods have their unique advantages. We will only cover the VLS method because the devices that will be discussed in later sections utilize nanowires grown by this method.

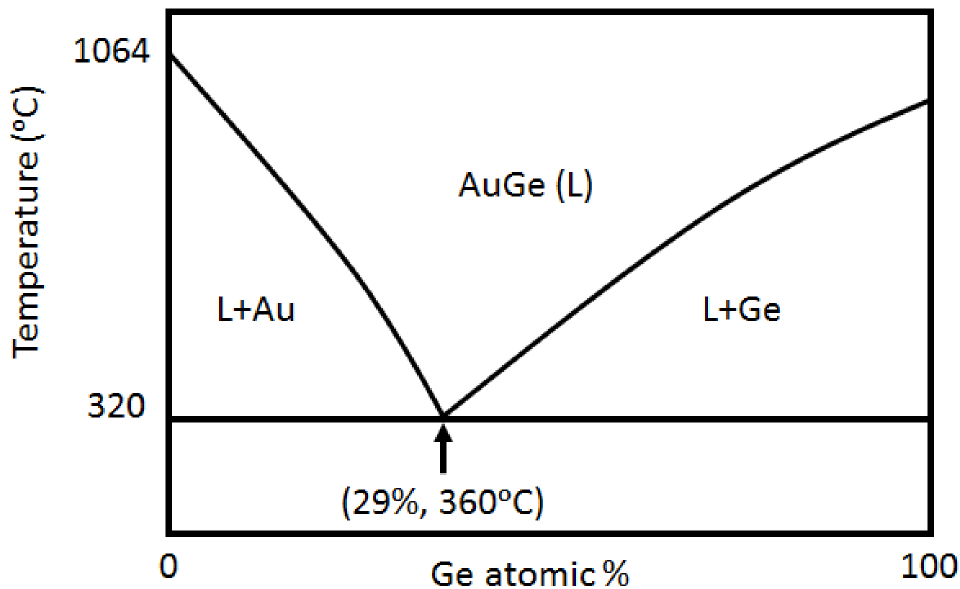

Figure 13: An illustration of the Vapor-Liquid-Solid (VLS) process for Ge nanowire growth using gold nanoparticles as catalyst. The eutectic point for this process occurs at 28% Ge content and 361°C [50].

The VLS process involves the use a nanoparticle, typically gold (Au), as a catalyst [29], [51]. Catalysts by definition promote a chemical reaction but are not consumed during the course of the reaction. The growth process starts with the dispersal of Au nanoparticles onto a substrate. The reactant species, in this case germane gas (GeH_4), are in the vapor phase. At an appropriate

temperature, the Au nanoparticles facilitate the decomposition of GeH_4 releasing Ge. The Ge adatoms diffuse into the Au metal to form a semiconductor/metal alloy (AuGe). At certain minimum temperature generally referred to as the eutectic temperature, the AuGe alloy melts and further catalyzes the decomposition of GeH4 gas and diffusion of Ge into the alloy.

The process described in the previous paragraph will continue until the alloy gets to a saturation point where the maximum Ge content that could be incorporated into the alloy has been reached. At this point Ge precipitates out of the alloy as crystalline Ge and attaches to the underlying substrate. The precipitation and attachment of crystalline Ge to the substrate is normally referred to as the nucleation stage. Beyond the nucleation stage, the process proceeds with nanowire growth usually along the radial direction. The eutectic temperature is only a minimum temperature required to melt the AuGe alloy. Beyond the nucleation stage, nanowire growth can proceed at a temperature lower than the nucleation temperature (with the system being in a supercooled stage). The growth temperature influences the nanowire growth rate, crystalline quality and shape.

2.3 Integration of free standing Ge nanowires on silicon substrate

For most Ge nanowire studies, the wires are grown on a substrate and subsequently transferred to a new substrate for device fabrication. While the method of growth and transfer is suitable for studying the properties of nanowires, making devices on transferred nanowires in a large scale will be very inefficient. Therefore, vertical integration of Ge nanowires on silicon substrate by growing the wires directly on the device substrate is very important for large scale implementation of Ge devices. As an example, one can potentially build photodetectors with very wide spectral response by utilizing the Si substrate and Ge nanowire structure. Such devices will have photo response from 0.3um to 2um, considering that Ge has a small bandgap of 0.69eV.

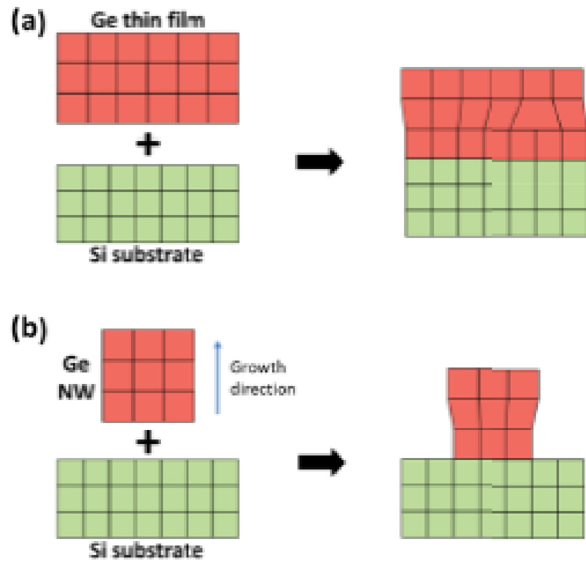

Figure 14: a) Growth of Ge on silicon substrate beyond the critical thickness which results in dislocation defects. (b) Due to strain relaxation in 1D structures allows for defect free growth of lattice mismatched materials like Ge nanowires grown on Silicon. Reprinted from ref [50].

Furthermore, epitaxial grown Ge nanowires on silicon substrate have shown very good heterojunction properties with very abrupt junctions [52]. Sharp heterojunctions are important for transistor applications such as Tunneling Field Transistors (TFTs) due to better gate control. Radial strain relaxation which leads to low defect density is another important reason for exploring vertically integrated Ge nanowires on Si substrate [9]. The proceeding sections will describe the unit steps involved in vertical epitaxial Si nanowire growth.

2.4 Epitaxial growth of Ge nanowires on (111) silicon

The nanowires used in our devices were grown on (111) silicon substrate. The reason for using (111) substrate is because Ge nanowires at 20nm diameter preferentially grow along the <111> direction [29], [51]. It has been documented in literature that nanowire growth occurs at near equilibrium conditions and as such the growth process is largely a thermodynamically driven

process [53]. Therefore, the growth direction occurs along the substrate crystal orientation where the required energy for the process to occur is minimized [53].

Our growth process employs the vapor-liquid-solid (VLS) method [54][50]. We used 20nm Gold (Au) nanoparticles suspended in colloidal solution as our catalyst material. The process was carried out at a chamber pressure of 45 Torr and gas flow of 1% germane gas (GeH_4) in H_2. The nucleation step occurred at 360°C for 1 minute and the nanowire growth/elongation was achieved at a lower temperature of 320°C. The reason for reducing the temperature during growth was to minimize the radial deposition of Ge during growth which leads to tapering of the nanowires.

2.4.1 Au nanoparticles adhesion to substrate to enable high growth yield

The nanowire density directly depends on the number of Au nanoparticles that adhere to the substrate before nanowire growth. The ability to achieve good epitaxial growth depends on the interface quality between the nanowires and the substrate. Any native silicon oxide on the substrate surface can affect the growth quality of the nanowires, particularly the Ge/Si epitaxial interface. Even though nanowires have been shown to grow on oxide surfaces [50], we need high quality Si/Ge interface for good device performance. To prevent any interface quality issue, the samples were treated with 0.1 M hydrogen fluoride (HF) solution. This removes any native oxide on the sample and creates a hydrogen terminated (H-terminated) substrate surface [50].

Due to citrate-stabilization of the Au nanoparticles and the H-terminated substrate surface, both the substrate and Au nanoparticles are negatively charged and will repel each other. The repulsion effect makes nanoparticle adhesion to the substrate difficult. To neutralize the citrate ion and reduce the nanoparticle/substrate repulsion as well as maintain the H-termination of the surface, we added HF to our Au colloid to a concentration of 0.1 M [54][50], [52]. Though it is

stated in Ref. [50] that increasing the acidity of the Au colloidal solution might cause clustering of the nanowires, we did not observe such effect during our experiments in the short time between the addition of HF and the deposition of the nanoparticles.

2.4.2 Effect of chamber pressure on nanowire growth

After sample cleaning and dispersal of Au nanoparticles as catalyst, the sample is transferred to the chamber for wire growth. The first step in the growth process is to stabilize the chamber pressure. For our process, the target pressure is 45 Torr. By flowing 200sccm of GeH_4 gas diluted in hydrogen, the target pressure was maintained by controlling the opening/closing of the gate valve connected to the pump. Pressure stabilization is necessary to prevent nanowire kinks and to maintain constant growth rate and to achieve high quality nanowires. We observed that the higher the pressure, the faster the growth rate of Ge nanowires. For instance, the growth rate changed from 50nm per minute at a pressure of 45 Torr to 215nm per minute at a pressure of 100 Torr.

2.4.3 Effect of temperature on nanowire growth

Immediately following the chamber pressure stabilization step is a rapid temperature ramp up of the substrate to the nucleation temperature. It has been observed previously in our research group that slow temperature ramp up can lead to non-ideal nanowire nucleation [50]. To achieve a rapid sample heat up, we used a local substrate heater instead of the furnace wall heaters. The local substrate heater enabled us to achieve a ramp rate of about 6°C/second. Vertical nanowire yield was about 60%. It is necessary to mention that very high temperature (> 340°C) causes significant tapering of the nanowires. To minimize tapering, high temperature steps are made very short. Also, rapid temperature ramp down below 300°C leads to significant kinking of the nanowires [50].

2.4.4 Effect of nanowire diameter on growth

The nanowire diameter is controlled by the size of the Au catalyst. The diameter of the nanowire affects the preferred growth direction. It has been observed in literature that Ge nanowires with diameter less than 15nm prefer to grow in the <110> and <112> directions [55][56]. We used 20nm diameter Au nanoparticles because 20nm wires prefer to grow in <111> direction. This gives a better vertical yield on (111) silicon substrate. Nanowire diameter could affect both the electrical and optical behavior of devices. For Ge nanowires less than 10nm, due to quantum confinement in the 1D structure, the bandgap of Ge increases. The increase in bandgap will increase the minimum photon energy that photodetectors based on such nanowires can detect. This is effectively a blue shift in wavelength.

2.4.5 Nanowire nucleation and growth

The nanowire nucleation and growth steps were done at two different temperatures. The nucleation was done at 360°C for 1 minute followed by a temperature ramp down. The nanowire growth/elongation step was done at 320ºC. The reduced growth temperature was to prevent nanowire tapering due to the radial deposition of Ge at elevated temperatures. Significant nanowire elongation occurs during the nucleation. The measured growth rate during nucleation is 200nm/min. This rapid elongation is expected during the nucleation step since the process is thermally enhanced. Nanowire elongation during the growth step is much slower with an average growth rate of 50nm/min.

2.5 Summary

In this chapter, we discussed the transport properties of Ge. The electron and hole mobility in Ge is higher than Si which makes Ge devices faster and smaller. We discussed the presence of

direct and indirect bandgap in Ge at the Near Infrared Region (NIR) which accounts for its strong optical absorption properties comparable to most III-V semiconductors. The possibility of sub bandgap optical absorption between the split-off band and the degenerate HH/LH band was explained.

Next, we discussed the lack of high quality inexpensive Ge substrate as a major setback in the fabrication of good Ge devices. The growth of 2D material on top of high quality substrates such as Si is highly limited due to the large lattice mismatch between Ge and Si. The use of Ge nanowires which are crystalline and almost defect free was presented as a high quality alternative to the Ge substrate and 2D grown material.

Furthermore, we explained the nanowire growth techniques such as the VLS method. The importance of pressure and temperature control during growth was emphasized. We also discussed the techniques for improving Au nanoparticle adhesion to Si substrate before nanowire growth to improve the growth yield. Lastly the integration of free standing nanowires on Si substrate without dislocations was attributed to strain relaxation in 1D structures.

Chapter 3

Ge nanowire photodetector on silicon substrate

3.1 Introduction

In this chapter, we will discuss the device fabrication steps. The method of isolating nanowires and controlling nanowire density by growing nanowires in trenches will be explained. The importance of good passivation layer between the nanowires and the underlying substrate will be elaborated on. We will explain the role of spin-on-glass (SOG) in selective etching of aluminum oxide from Ge nanowire sidewall. Next, we will discuss the optical measurement setup and the use of backside optical pumping for nanowire excitation.

For the majority of this chapter we will be discussing the different devices fabricated from Ge nanowire. The single nanowire device grown on n-type Si substrate without Si shell will be analyzed to determine the current gain, responsivity and quantum efficiency. The results of the single nanowire will be compared to the nanowire array device to determine if the devices are scalable based on the number of nanowires. The core/shell nanowire array device grown on n-type Si with Ni Ohmic contact will be discussed. We will also cover the core/shell nanowire array device grown on p+ Si substrate with Au contact. Finally, the core/shell device grown on n-type substrate will be analyzed for solar cell performance.

3.2 Substrate Preparation

The growth process started with lightly doped n-type Silicon substrate of (111) orientation (usually 4 inches in diameter). The substrate was cleaned to remove organics and the native oxide

was striped using diluted hydrofluoric acid (HF). A thick oxide was thermally grown and patterned to create openings for heavy doping of selected areas to form ohmic contact with the substrate. The patterned openings were wet etched in diluted HF to expose the substrate and subsequently doped with Phosphorous in a high temperature furnace. The wafer was diced into 16mm by 20mm rectangular pieces for device fabrication. 25nm of Al_2O_3 was deposited using Atomic Layer Deposition (ALD) tool to protect the substrate surface. Next, a 10% diluted 700B Spin-on-glass (SOG) was spun at 4000rpm and cured at 300℃ for 45 minutes to create a 30nm layer of SOG on the substrate.

3.3 Trench Patterning and VLS Growth

The prepared substrate was patterned by photolithography to create trenches of desired diameter (depending on the wire density required) from which the nanowires were grown (See Figure 15). Using the photoresist as a mask, the exposed trench areas were etched in 1Mole Hydrofluoric acid for two minutes. 20nm Gold colloidal solution was dropped on the substrate and rinsed off after 5seconds in de-ionized water. The photoresist mask was removed using Acetone and the substrate was rinsed in IPA. The sample was transferred to the LPCVD chamber for nanowire growth. Using GeH_4 gas diluted in H_2 gas (10% GeH_4), the VLS process was carried out at a nucleation temperature of 360℃ for 1 minute and a growth temperature of 300℃.

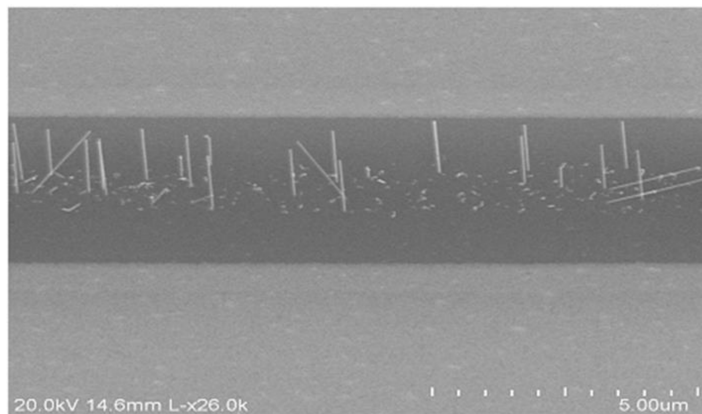

Figure 15: Scanning electron micrograph of Ge nanowires grown in a pattern trench. Aluminum oxide was patterned to define the active area and nanowires were grown using the VLS method.

3.4 Post Growth

After growth, the nanowires were passivated by a conformal deposition of 25nm Al_2O_3 using the ALD system. Besides providing mechanical support for the nanowires for subsequent processes, good quality Al_2O_3 layer prevents short circuits between the top and bottom contacts. The ALD step was followed by spinning and curing of 50% SOG to create a spacer layer. The SOG was cured at 300ºC for 45 minutes at a temperature ramp rate of 300ºC /hour. The slow ramp rate was to prevent the SOG layer from cracking. In order to improve SOG adhesion, HMDS solution was spun before the 50% SOG.

To create electrical contact to the nanowire (top-contact), the conformal Al_2O_3 layer around the nanowire was selectively etched to expose the top of the nanowires. The etching was done using phosphoric acid heated to 36ºC. Phosphoric acid does not etch the SOG, it only etches aluminum oxide. The SOG layer servers two purposes, first is to protect the underlying layer of aluminum oxide from being etched, preventing a leakage path to the substrate. The second purpose was to serve as a planarization layer which allowed the standing nanowire to be exposed for aluminum oxide etching. Nickel was deposited at a 45-degree angle to make contact with the standing nanowire through a lithographic and lift-off process. A final lithographic process was carried out to define the bottom contact. The SOG layer and Al_2O_3 layers were wet etched using diluted hydrofluoric acid and Ni was evaporated followed by lift-off.

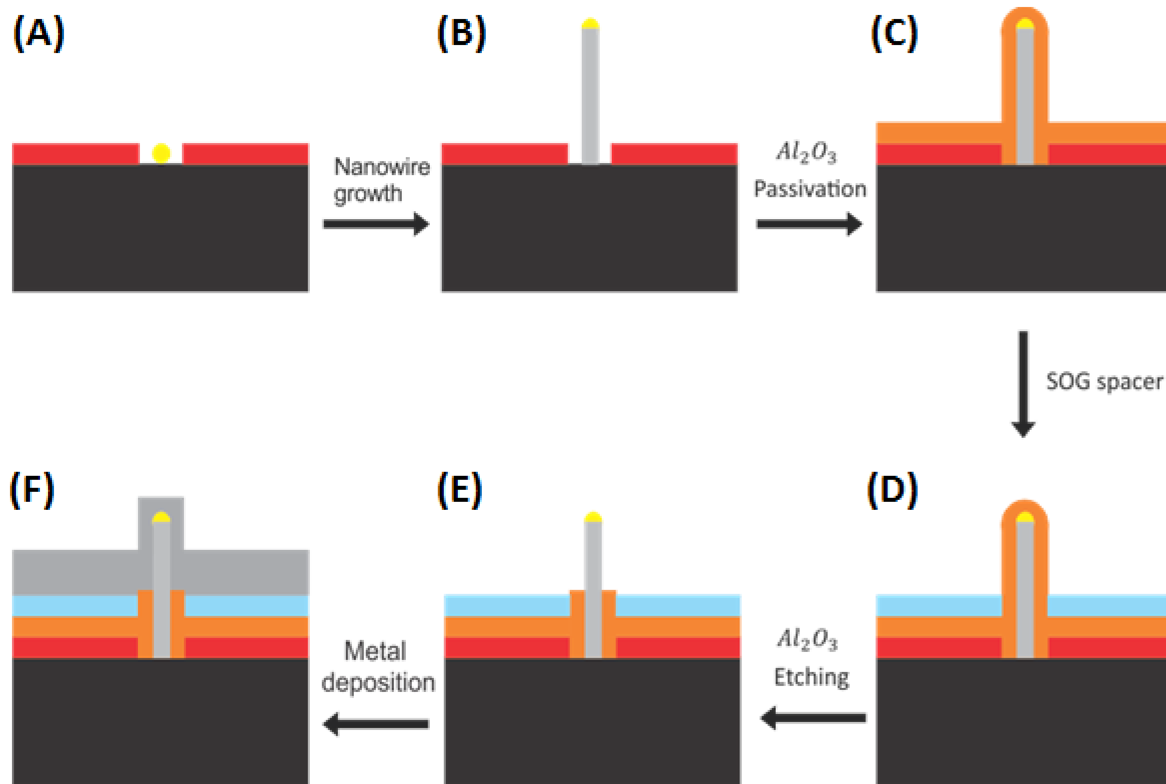

Figure 16: Schematic drawing showing the nanowire photodetector fabrication process from initial Au colloid deposition (A) to the last step of nickel deposition (F)

For devices based on single nanowires, we isolated each nanowire manually. This was done by taking a detailed scanning electron microscope (SEM) image around a predefined alignment marks close to the nanowires trenches. Using a custom made image processing software, the coordinates of the nanowires within the trenches were mapped with respect to the alignment marks. From this map, a GDS file was created that drew a line directly on the selected nanowires. The coordinates were verified using the Raith electron beam lithography (E-beam) system. This was followed by E-beam lithography and lift-off process.

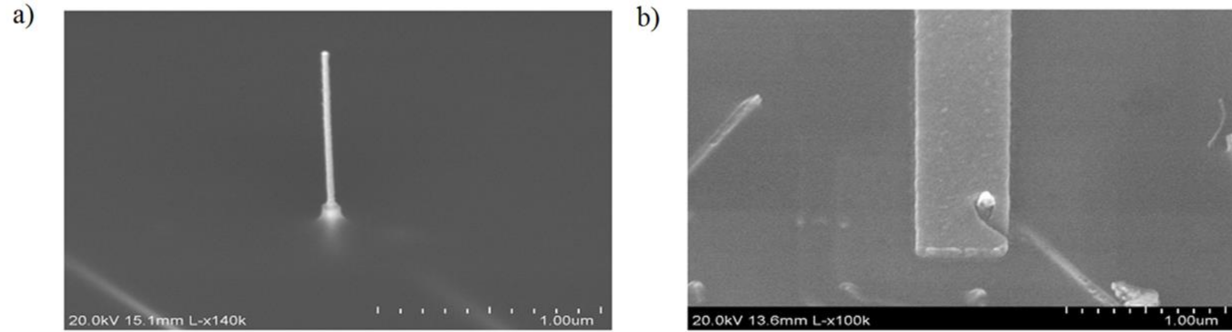

Figure 17: SEM images for the various fabrication stages. (a) Single nanowire after selective SOG and Al_2O_3 etching (b) Side view of a single nanowire device after Nickel deposition and lift-off process.

3.5 Optical Measurement Setup

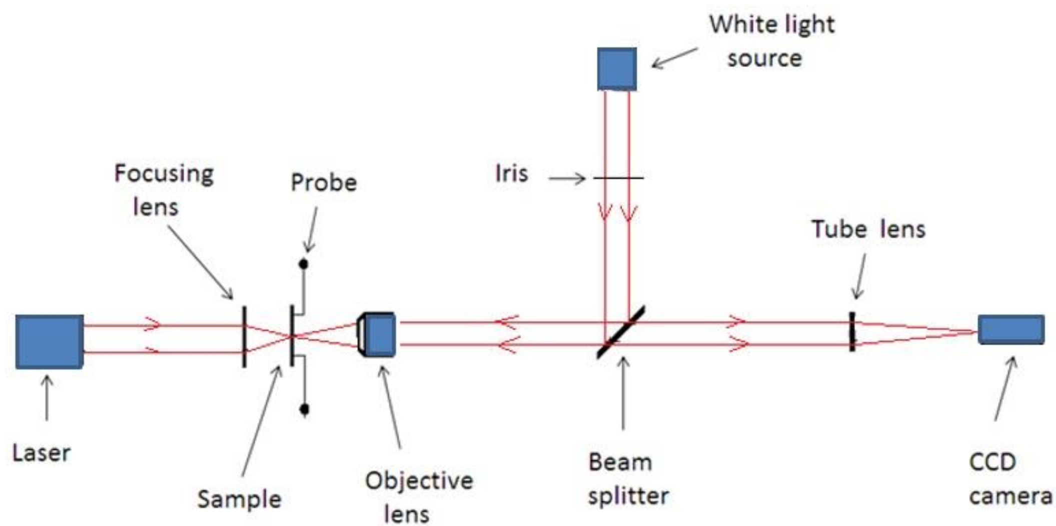

Figure 18: Optical setup for photocurrent measurement at 1.55um wavelength. The alignment for the setup was completed using the confocal microscopy.

Using a white light source, 20X objective lens and a CCD camera, confocal microscopic setup was used to align the photodetector sample for precise optical excitation of the active device region, in this case, a photodetector based on a single vertical Ge nanowire. The white light source

(LED) was used to illuminate the sample by splitting the beam using a 50:50 beam splitter. The reflected light was focused down on the sample using a 20X objective. The sample image was transmitted back through the objective lens and the beam splitter and was focused to a CCD camera using a tube lens. Next the laser beam was focused at the location of the sample using the same optical setup. The nanowire excitation was done through backside optical pumping using a 1.55um variable power (1mW to 800mW) laser since the Si substrate is transparent at 1.55um. The laser was focused down from 5mm beam radius to a 600um beam radius. This translates to an optical intensity of 282W/cm^2 at the maximum laser power.

3.6 Ge core nanowires on n-type Si substrate

3.6.1 Single nanowire device

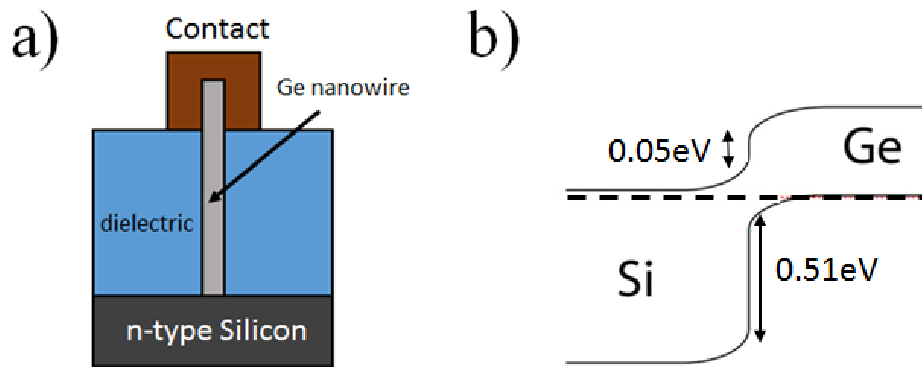

Figure 19: (a) Device schematic for single vertical Ge core only nanowire photodetector. (b) Band diagram for Si/Ge p-n heterojunction at no applied bias

The devices used in this study consist of a single Ge nanowire epitaxially grown on an n-type Si substrate, as shown in Fig. 19. From the electrical measurement of single nanowire devices, the I-V response shows that the device behaves like a p-n heterojunction. The dark current is very

low (< 1nA, Fig. 20). The ideality factor of 1.9 shows that our device quality including the Ge/Si interface is good. Even though no dopants were introduced into the Ge nanowire during growth, the Ge nanowire was inherently doped due to the effect of surface defect states and fermi level pining. The surface doping will be explained in the proceeding section. The doping concentration of the nanowires is estimated to be about $10^{18}\mathrm{cm}^{-3}$ [50].

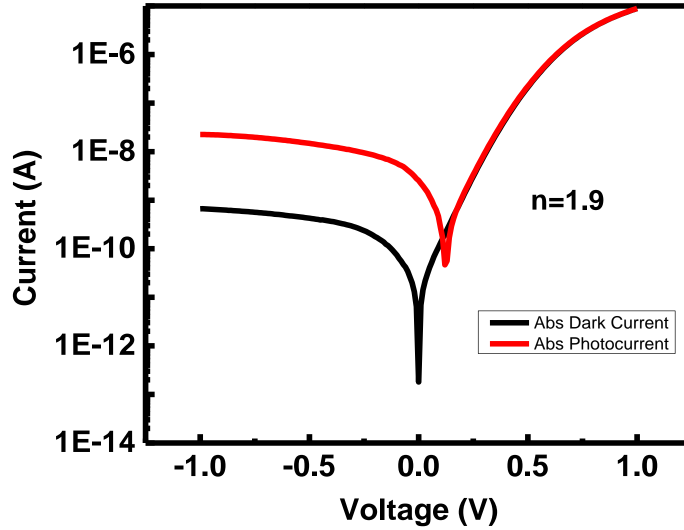

Figure 20: I-V plot of single nanowire photodetector excited at 1.55um with an optical power of 800Mw.

Using the doping concentration of $10^{18}\mathrm{cm}^{-3}$ and assuming uniform doping due to the nanowire dimension, we calculated the length of the depletion width at the Ge side of the junction from the equation:

$$W_{Ge}(V) = \left[\frac{2\epsilon_{Si}\epsilon_{Ge}(V_{bi}-V)}{e}\left[\frac{N_{Si}}{N_{Ge}(N_{Ge}\epsilon_{Ge}+N_{Si}\epsilon_{Si})}\right]\right]^{1/2} \tag{26}$$

$$V_{bi} = \frac{1}{e}(\Delta E_c + E_{Ge}) - \frac{k_B T}{e}\ln\left[\frac{N_{c-Si}\,N_{V-Ge}}{n_{Si}p_{Ge}}\right] \tag{27}$$

Where

W_{Ge} is the depletion width at the Ge side, ϵ_{Si} and ϵ_{Ge} are material permittivity, N_{Si}, N_{Ge}, n_{Si}, p_{Ge} are doping densities for Si and Ge, N_{c-Si} and N_{V-Ge} are conduction and valence band effective densities.

The depletion width on the Ge side is 4.4nm. This implies that most of the junction depletion happens at the Si side. Photocurrent due to absorbed carries at the junction will be very negligible since Si is transparent at 1.55um and the volume of Ge material within the junction is very small. However, carriers generated within one diffusion length away from the junction can diffuse to the junction and contribute to photocurrent. We thus consider the active region of our device to be the Ge side of the p-n heterojunction up to one diffusion length. The minority diffusion length has been experimentally measured in ref[57] to be about 200nm. Taking into account the active region of our device, it is reasonable to consider carrier transport as limited by diffusion instead of drift because the field will be extremely weak outside of the junction area.

The p-n heterojunction plays a major role in suppressing the leakage current and providing the field needed to sweep minority carriers (electrons in this case) across the junction. The effect of the p-n junction in suppressing leakage current will be shown by comparing the p-n heterojunction detectors with the p+/p Si/Ge nanowire detectors in later section of this report. Our device can be described as a photodetector based on a p-n heterojunction structure, where one side of the junction (Si side) does not play any major role in the optical properties of the device at 1.55um wavelength. On the active side (Ge side), the depletion region is very small and there is not enough material volume to contribute substantially to photon absorption. Most of the observed optical properties comes from one diffusion length away from the junction.

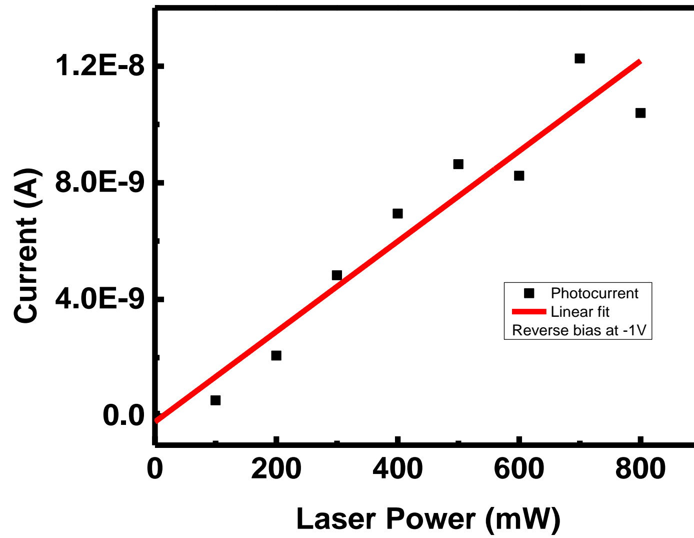

Figure 21: Plot of photocurrent versus optical power varied from 0W to 0.8W. The photocurrent increased linearly without any observable saturation.

Fig. 20 shows that photocurrent for this single-nanowire based device can be 10-20nA, which is high when compared to other devices[58]. Similar level of photocurrent was consistently observed in our devices. To verify that the photocurrent is due to optical absorption and not from other external secondary effects, the laser was directly modulated at low frequency and the electrical response of the photodetectors where measured. The devices responded beyond 50 KHz. However, the square wave function was lost at high frequencies due the RC delay associated from the parasitic capacitance from the external circuitry. If these results were as a result of thermal effects, the response of the wires to the modulated light would have been much slower due to the low thermal conductivity of nanowires [59]–[62].

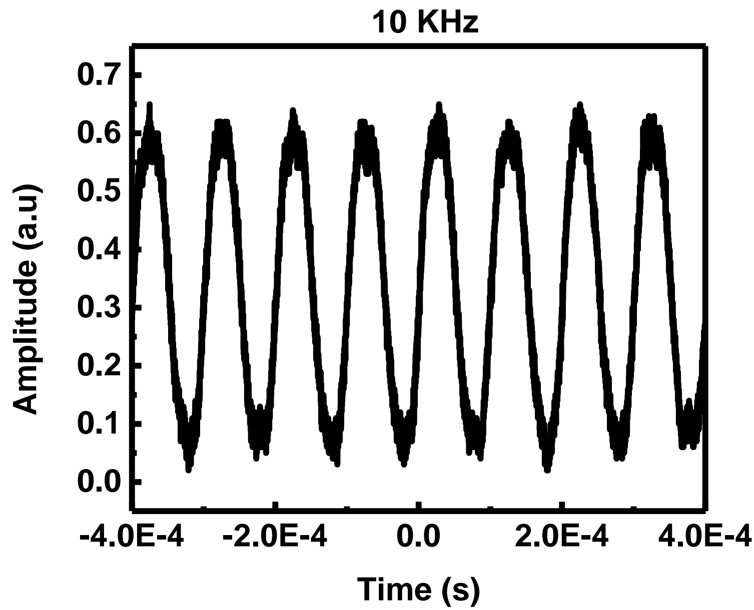

Figure 22: Pulsed response of photodiode excited with a modulated optical source at 10 KHz and 0.8W optical power.

Using equations from section 1.1.1 we estimated the maximum amount of photocurrent that could be generated from the nanowire structure. By comparing the theoretically calculated current to the actual current (measured current) of the device, we can estimate the current gain. The value of the gain gave us a good insight about the performance of the nanowire photodetectors. For the calculations, we have assumed constant optical intensity along the radial direction of the nanowire. This is a reasonable assumption considering that less than 1% of incident light will be absorbed within the nanowire material.

An important figure of merit for photodetector is the quantum efficiency. The quantum efficiency tells us how many electron-hole pairs are generated for each photon absorbed. Ideally we would like to have quantum efficiency greater than 1, which implies an internal gain mechanism within the photodetector. Parameters such as the actual amount of light absorbed within a material (determined by the absorption coefficient) and reflectivity of the material surface

limit the quantum efficiency of photodetectors. Quantum efficiency is given by the following equation:

$$\eta = \eta_i (1 - R)(1 - e^{-\alpha d}) \quad (28)$$

Where

η_i is the intrinsic quantum efficiency, R is the reflectivity, α is the absorption coefficient of the absorbing material and d is the distance travelled by the light beam within the absorbing medium.

We can solve the above equation if we have only one unknown variable in the equation. Here however two unknown variables, η_i and R, are present. From our measurement data, Figure 23, we can determine the injected primary photocurrent I_{ph} based on the equation:

$$I = I_o \left(e^{\frac{qV}{k_b T}} - 1 \right) - I_{ph} \quad (29)$$

Where

I_o is the dark current value.

At -1V bias, the current equation reduces to $I = -I_o - I_{ph}$ and we can calculate I_{ph} from the I-V plot of photocurrent and dark current.

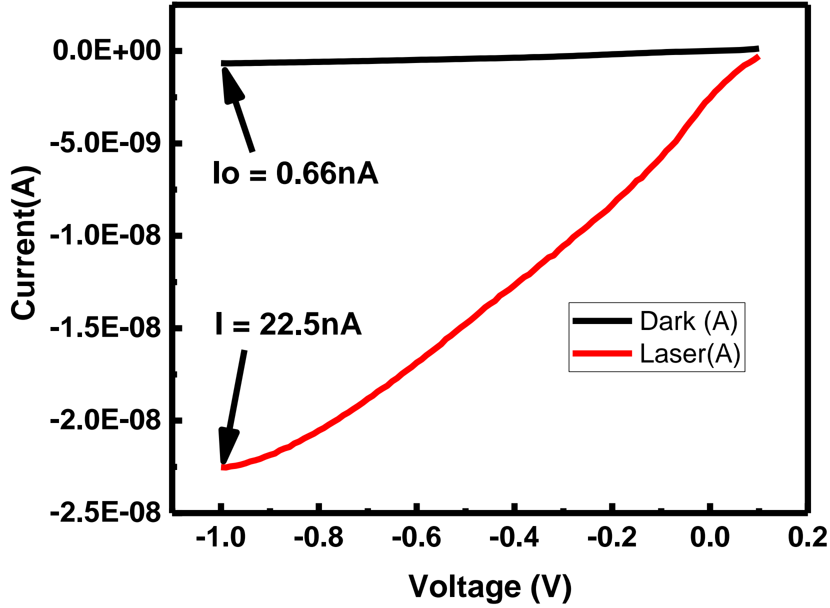

Figure 23: I-V plot of single Ge nanowire photodetector with a marked region showing I_o and I at -1V bias.

The equation for I_{ph} can be written as:

$$I_{ph} = eAG_o(L_p + L_n) \approx eAG_oL_p \tag{30}$$

Where

G_o is the optical generation rate, A is the nanowire radial area and L_p is the diffusion length at the Ge side of the heterojunction.

In the photocurrent equation, we have neglected L_n and W_n because Si is transparent at 1.55um wavelength and we assumed all the absorption is from the Ge nanowire. This hypothesis was experimentally verified by our control studies that the photocurrent generated from absorption in Si is indeed negligible.

From the photocurrent equation, we can calculate G_o as:

$$G_o = \frac{I_{ph}}{eAL_p} = 2.23 \times 10^{27} cm^{-3} s^{-1} \quad (31)$$

G_o is related to the external quantum efficiency and volume of the nanowire by the equation:

$$G_o = \eta(P_{opt}/\hbar\omega)/Vol \quad (32)$$

From the above equation, we can calculate external quantum efficiency as:

$$\eta = \frac{G_o \times Vol}{P_{opt}/\hbar\omega} = \frac{2.23\times10^{27} cm^{-3} s^{-1} \times 6.28\times10^{-17} cm^3}{8.85\times10^{-10} W/(0.8\times1.6\times10^{-19} J)} = 20.26 \quad (33)$$

If we assume a worst case situation where the reflectivity is zero, we can calculate the internal quantum efficiency as:

$$\eta_i = \frac{\eta}{1-e^{-\alpha d}} = \frac{20.26}{1-e^{(-460/cm\times200\times10^{-7} cm)}} = 2212 \quad (34)$$

The physical meaning of the internal quantum efficiency result is that for each incident photon absorbed, 2212 electron-hole pairs are generated. This can happen only if there is an internal gain mechanism. Next we calculate the responsivity of our detector using the equation:

$$R_\lambda = \frac{i_p}{P_\lambda} = \eta \frac{q}{\hbar\omega} = 25.3 \text{A/W} \quad (35)$$

The current amplification can be calculated with certain careful assumptions. Normally we consider current amplification as the measured current divided by the theoretical current. However, what values should be used for theoretical calculation is subject to varying interpretations. For our theoretical maximum current calculation, we assume that internal quantum efficiency is unity. Secondly, we calculate the generation rate based on the absorbed optical power only, which is determined by the incident optical intensity multiplied by $(1 - e^{-\alpha d})$.

After making these assumptions, the absorbed optical power was calculated to be 8×10^{-12}W. Using these values, the generation rate is calculated to be $10^{24} cm^{-3} s^{-1}$. The calculated photocurrent using the theoretical generation rate is 10pA, and led to a current amplification factor of

$$\text{Current amplification factor} = \frac{\text{Measured current}}{\text{Theoretical current}} = \frac{20\text{nA}}{0.01\text{nA}} = 2 \times 10^3 \tag{36}$$

Next, we calculated the photoconductive gain of the device using the measured photocurrent and the absorbed power as:

$$Photoconductive\ gain\ (G) = \frac{I_{pc}/e}{P_{abs}/\hbar\omega} = 1974.1 \tag{37}$$

P_{abs} is the power absorbed taking into account the absorption coefficient of the photoconductor material. The estimated gain value is higher than previous estimates for 60nm Ge nanowires which is about 20 [63]. However, not many optical studies have been done on low dimension Ge nanowires within the 20nm diameter range. The mechanism of the current amplification and the high photoconductive gain will be discussed later in Section 3.6.4.

3.6.2 Array Ge nanowire device results

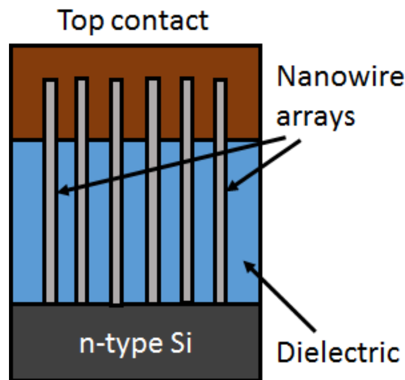

Figure 24: Schematic drawing of nanowire array photodetector. Some of the wires in actual device may be angled instead of vertical.

We further investigated the photo response of devices based on nanowire arrays to see if the measured photocurrent scales with the number of Ge nanowires. For the array devices, photolithography based on a stepper equipment was used for device fabrication. The top finger (electrode) size was 10um wide by 2um long and the contact thickness was 70nm of Nickel. From photocurrent measurements (e.g. Fig. 25), the photocurrent indeed scales according to the number of nanowires in the array. From SEM images, each array was estimated to contain 10 to 15 nanowires. The photocurrent for array devices was higher than the photocurrent for single nanowire device by a factor of ~10x. This implies a linear increase in the photocurrent as the number of nanowires increases.

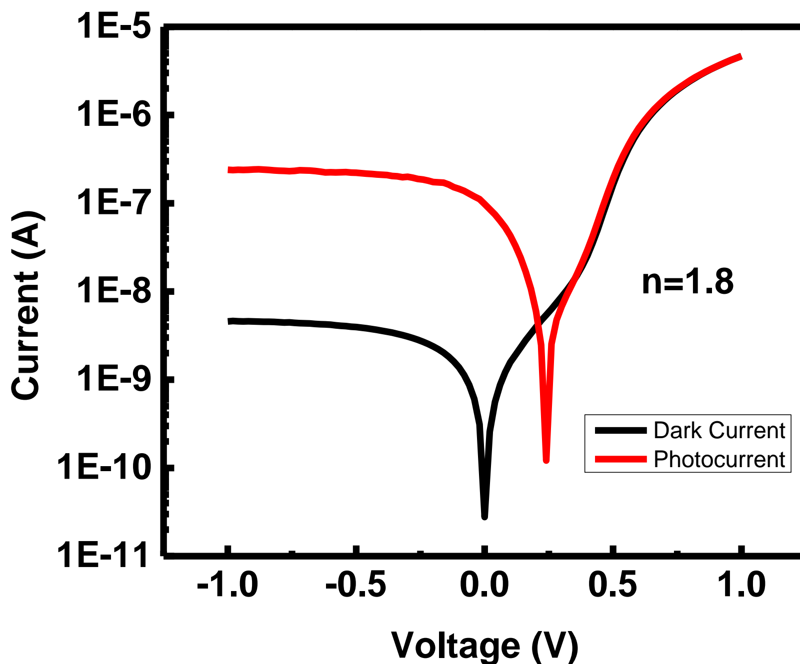

Figure 25: a) I-V plot of arrays of nanowire photodetector excited at 1.55um with an optical power of 800mW.

The current increase from the nanowire array is as a result of increased optical absorption due to a higher volume of the Ge material as the number of nanowires increases. Reduced resistance due to the parallel connected nanowire array could contribute to the increase in current. However, considering the known operation mechanism of nanowires which we will discuss in the next section, it is more likely that the increased current is due to higher absorption only.

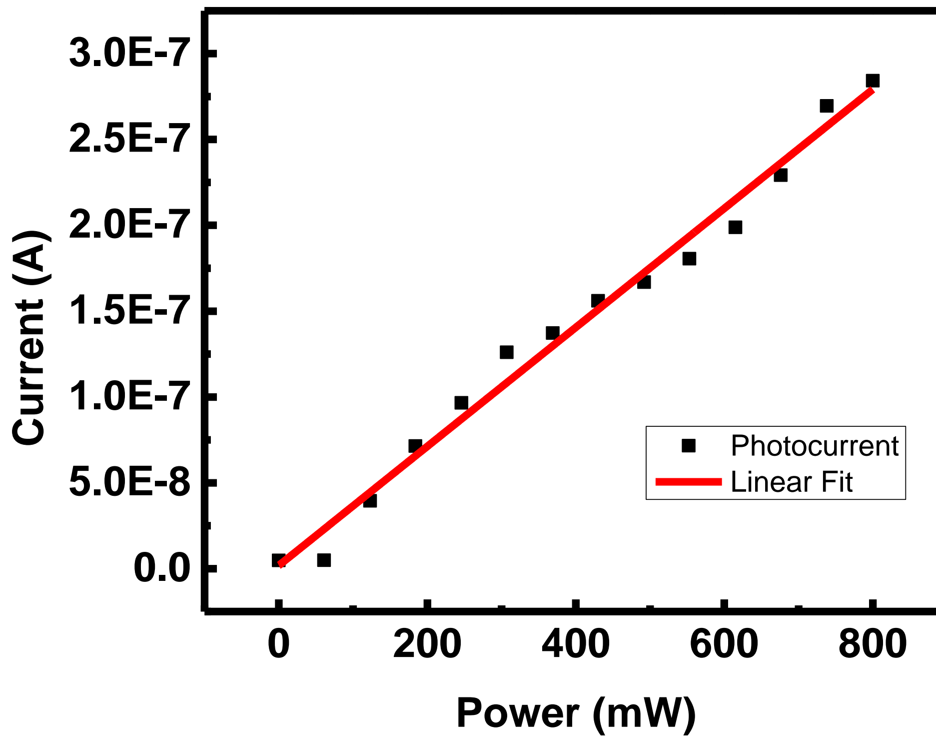

Figure 26: Plot of photocurrent versus optical power varied from 0W to 0.8W

The photocurrent increased linearly as the optical pump power is increased without any sign of clear saturation within the optical power range, as shown in Fig. 26. However, there was

only a 50% reduction in rise and fall time when the array device is compared to the single nanowire device, likely due to RC delay in the external circuit.

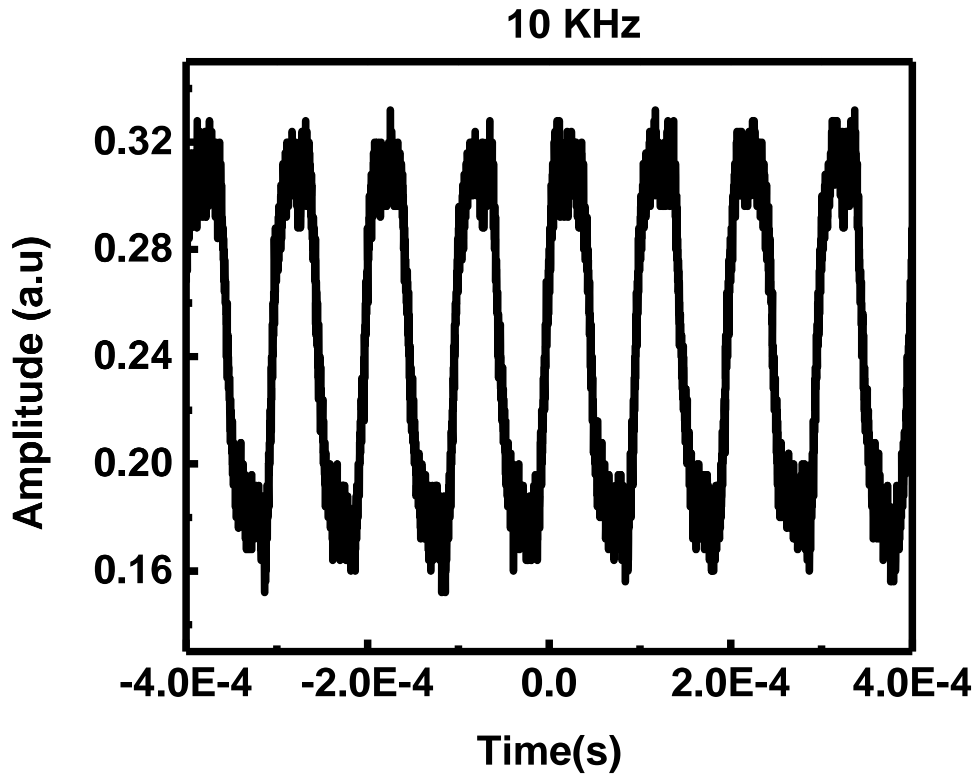

Figure 27: Pulsed response of photodiode excited with a modulated optical source at 10 KHz and 0.8W optical power.

3.6.3 Optical field enhancement around standing nanowires

To investigate the high current gain observed in our devices, we used the Comsol optical software to simulate the electric field distribution around a standing Ge nanowire on Si substrate. The initial simulation was done for a bare Ge standing nanowire. The subsequent simulation was done for the full device structure including the dielectric layers and Ni metal contacts. For the bare Ge nanowire, the simulation showed that the standing nanowire has waveguide properties. There was strong light guidance along the nanowire and the electric field plot showed an enhancement

of more than 2x. The electric field input magnitude was 1V/m but the field along the wire was greater than 2V/m. However, we did not observe any optical modes within the nanowire itself. Most of the light is guided at the sides of the nanowire with some light penetration into the nanowire core. The highest field enhancement was at the Si/Ge heterojunction.

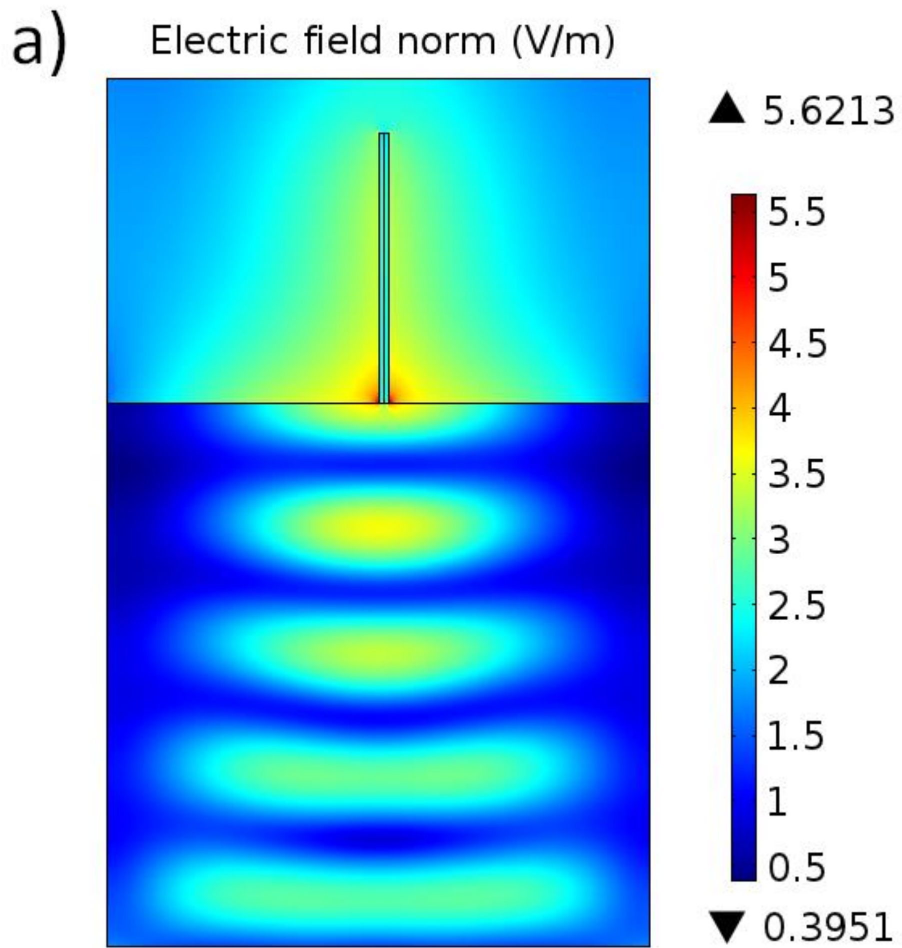

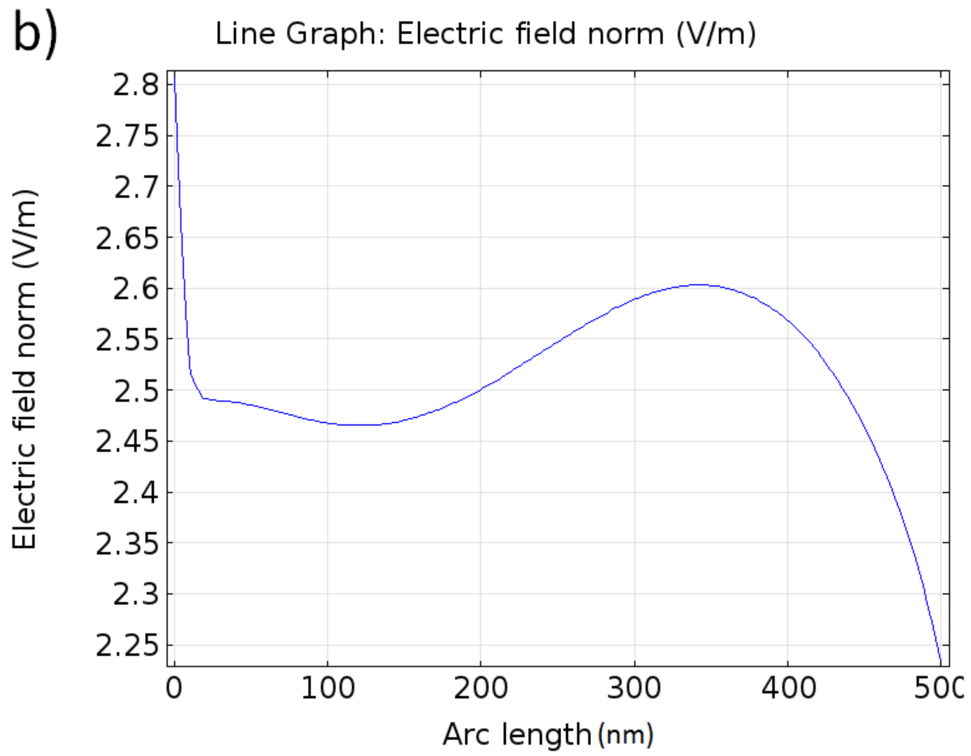

Figure 28: (a) 2D plot of electric field along a bare Ge nanowire length (nanowire standing in Si substrate surrounded by air). The input excitation is a plane wave with initial amplitude of 1V/m and excited from the bottom side of the Si substrate. (b) ID plot of electric field along the nanowire length.

a)

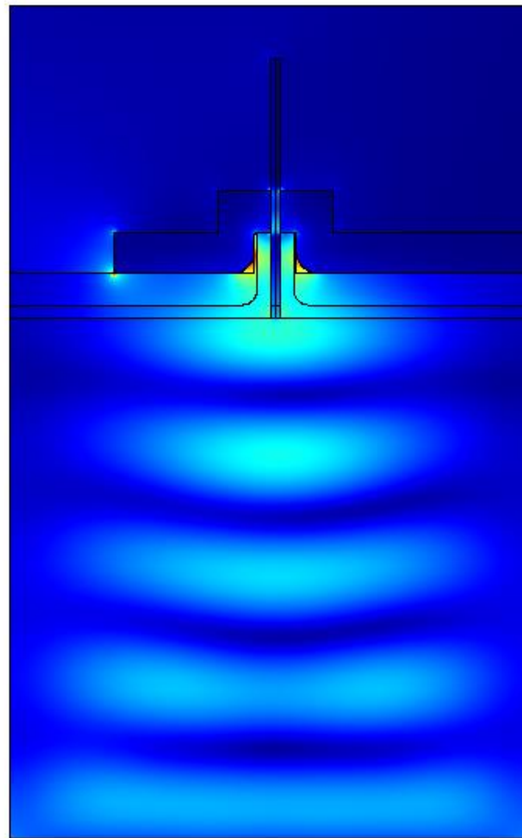

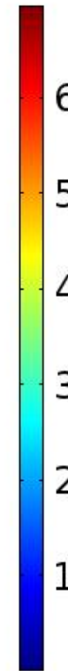

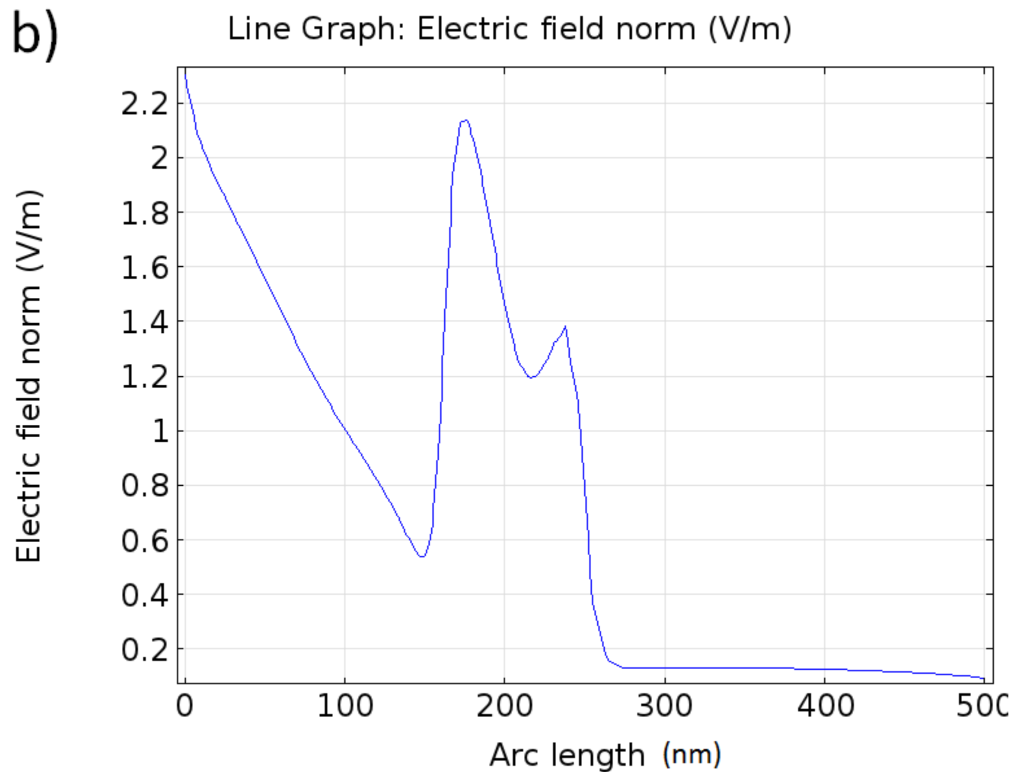

Figure 29: (a) 2D plot of electric field along a bare Ge nanowire length (nanowire standing in Si substrate surrounded by air). The input excitation is a plane wave with initial amplitude of 1V/m and excited from the bottom side of the Si substrate. (b) ID plot of electric field along the nanowire length.

The simulation of the full device structure showed completely different field profile from the bare Ge nanowire. The field profile showed some sharp peaks along the nanowire. This could be a result of local resonances formed due to reflections from the Ni metal as well as cladding effect of the aluminum oxide and silicon dioxide layers. However, we observed an overall field enhancement up to the 200nm length of the nanowires. Beyond the 200nm region, most of the light was absorbed in the contacts. This is consistent with the design of our detectors, where we expected no contribution to photocurrent beyond the diffusion length region. In any case, in both simulations the gain in the electric field enhancement is about 2 which is much lower than the experimentally

observed gain of ~ 2000. From the simulation, we ruled out the possibility of the observed photocurrent being mainly from the strong optical field enhancement around the nanowires.

3.6.4 Photocurrent enhancement as a result electron trapping

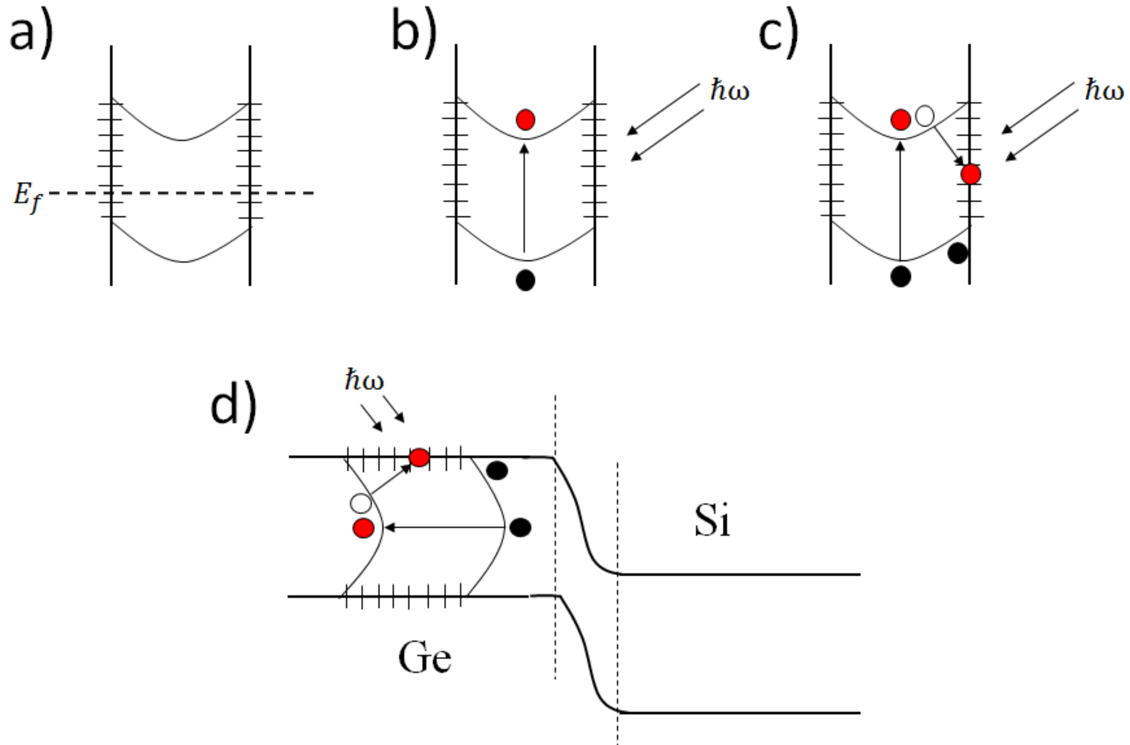

Figure 30: (a) Illustration of the band diagram of a core only Ge nanowire clearly showing the p-type behavior due to Fermi level pining close to valance band at the surface. (b) Illustration of light absorption creating electron-hole pairs (c) Schematic showing electron trapping at the surface states and holes being pulled close to the surface due to the effect of field. (d) Complete band diagram showing he p-n heterojunction.

The large current amplification gain effect was explained by a mechanism considering surface trapping of photo-generated carriers, schematically shown in Fig. 30, due to the large surface to volume ratio and the proximity of the surface to any region in the nanowire for such small diameter nanowires.

As explained in Sec.1.1, similar to ZnO nanowire photodetectors, in the Ge nanowire photodetector after creating an electron-hole pair by an incident photon, the electron may be trapped at the nanowire surface and stay there for a long time before it is finally recombined with a hole. This is different from a conventional photoconductor where the generated minority carriers (*e.g*. electrons in this case) quickly diffuses to the electrode. To maintain charge neutrality, hole carriers are injected into the nanowire. Due to the long lifetime of un-trapped carriers (e.g. estimated to be 33 seconds for the ZnO nanowire [33]) as compared to their transit time, this means that equivalently electron-hole pairs are created during the lifetime of the trapped carriers, leading to large current amplification factor shown in Eq. 36. From a different angle, the effect of trapped electrons is equivalent to gating the p-type nanowire. The higher the number of surface states, the stronger the gating effect is.

For our devices, the p-n junction between the Ge nanowire and the Si substrate adds an extra advantage of very low dark current, compared with the ZnO nanowire photodetector case, where a simple photoconductor structure was used leading to high dark currents. Under illumination, the photoconductive gain introduced by the trapped electrons leads to high photocurrent measured in our devices, which is more than 3 orders of magnitude higher than the estimated photocurrent. It is important to note that our theoretical calculation was made assuming a 100% quantum efficiency which was a worst case situation.

3.6.5 High dark current

A major figure of merit for photodetectors is the dark/leakage current. Ideally, we would like to have devices with negligible dark current. This is important in order to improve the signal to noise to ratio. Usually, it is desirable to have a photocurrent level that is at least ten times higher than the dark current. Si devices are known to exhibit smaller dark current compared to Ge devices.

This can be attributed to the larger bandgap in Si, and the difficulty of producing very high quality Ge substrates. For Ge nanowire devices, we expect reduced leakage current compared to bulk Ge devices because of the high quality of the nanowires.

Unfortunately, in our Ge nanowire devices, the measured leakage current of 2e-9A is still several orders of magnitude higher than the expected range of 1e-14A to 1e-13A. To understand the reason for this high leakage current, we used device simulator to simulate our device while applying different physics parameters to see if we can reproduce similar results to what we observed experimentally. From the simulation, we were able to produce band diagrams for different bias conditions. Fig. 31b shows the band-diagram at relevant -1V bias condition.

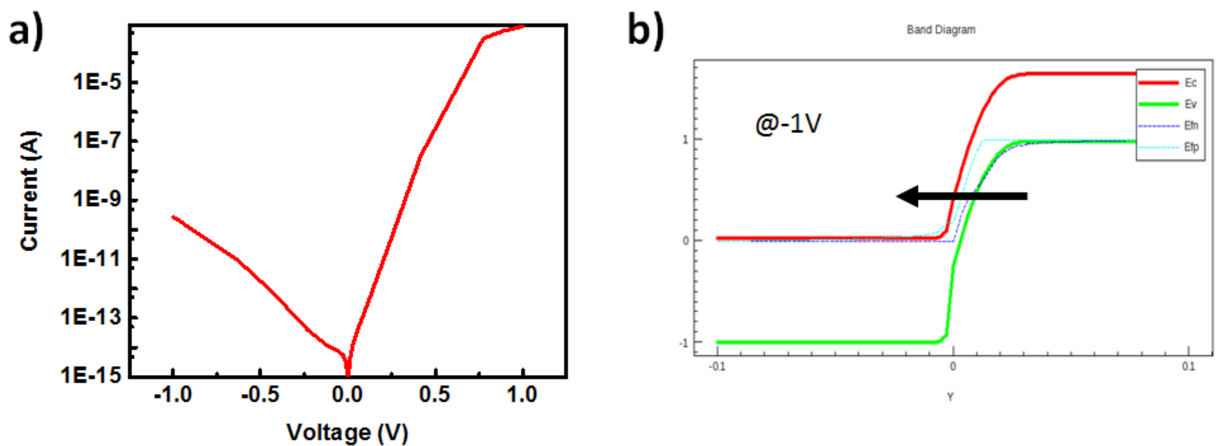

Figure 31: (a) I-V plot from the device simulation for Ge core only structure. (b) Band diagram showing the narrow region from which tunneling could occur.

In the device simulation, we tried to reproduce the leakage current using different mechanisms such as interface defects at the heterojunction and tunneling. The dark current increased significantly to almost the same level observed in the actual device when tunneling effect was included. However, comparing the I-V plot of the simulation to actual device I-V

characteristics, it can be observed that tunneling effect started at a much lower reverse bias voltage than the simulation shows. Understanding the cause of performance limiting effects such as leakage will give us better insight on how to mitigate them in future devices.

3.6.6 Nanowire size dependent gain

At small nanowire diameter, the photoconductive gain of Ge nanowires has been shown to be very high. Previous studies on similar nanowires have shown that photoconductive gain increases with a decrease in nanowire diameter [63]. In ref[63], the photoconductive gain saturated at lower power for the smaller nanowires (50nm and 60nm). This could the due to the filling of available trap sites which caused excess electron-hole pairs to recombine.

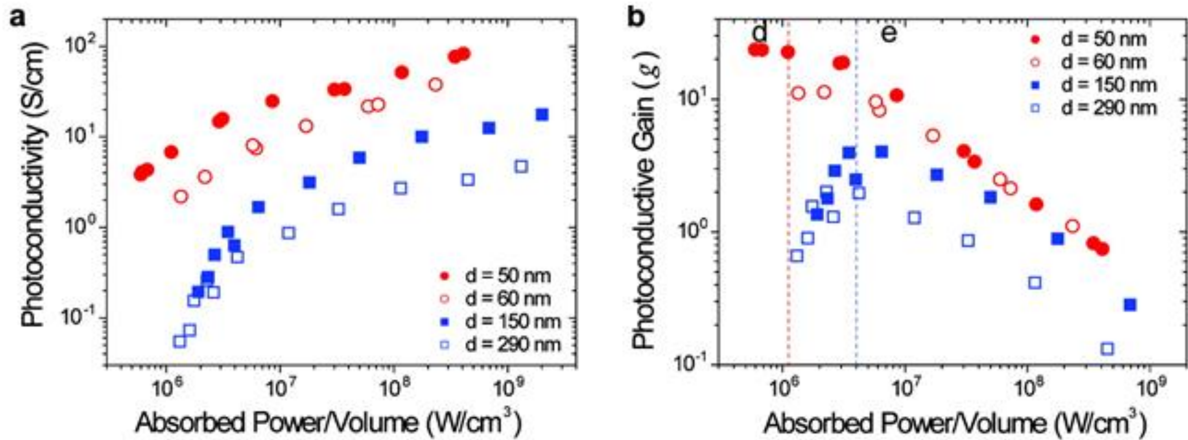

Figure 32: Plot of photoconductivity versus absorbed power density for Ge wires with different diameter. (b) Plot of photoconductive gain versus absorbed power density. Reprinted with permission from ref[63]. Copyright 2010 American Chemical Society.

For our single nanowire devices, the photoconductive gain was more than 1000, which is about two orders of magnitude higher than the value shown in Figure 32. This high gain should be expected because our nanowires are smaller than the wires used in the prior experiment. The effect of surface states will be stronger for smaller wire geometries due to stronger interaction between

the surface states and photo generated charge carriers. Photoconductive gain has been shown to be inversely proportional to nanowire diameter [63].

3.6 Ge/Si core/shell nanowire array device

Next, we examined the optical response of Ge nanowires with a silicon shell. The Si shell was added following the normal nanowire growth in the LPCVD furnace by flowing silane gas at a temperature of 470ºC for 2 minutes. The silane gas decomposes and Si is deposited at the sidewall of the nanowires to form a radial Si shell. The shell thickness is about 3 to 4nm and is intrinsic silicon. The addition of Si shell to Ge nanowires changes the electrical and optical characteristics of the nanowires. The radial Si shell forms a quantum well with the Ge core because of the lower bandgap of Ge compared to Si. The Si/Ge/Si hetero structure leads to the formation of a 1D hole gas[64] which changes the electrical transport behavior of the material in terms of mobility and electrical conductivity.

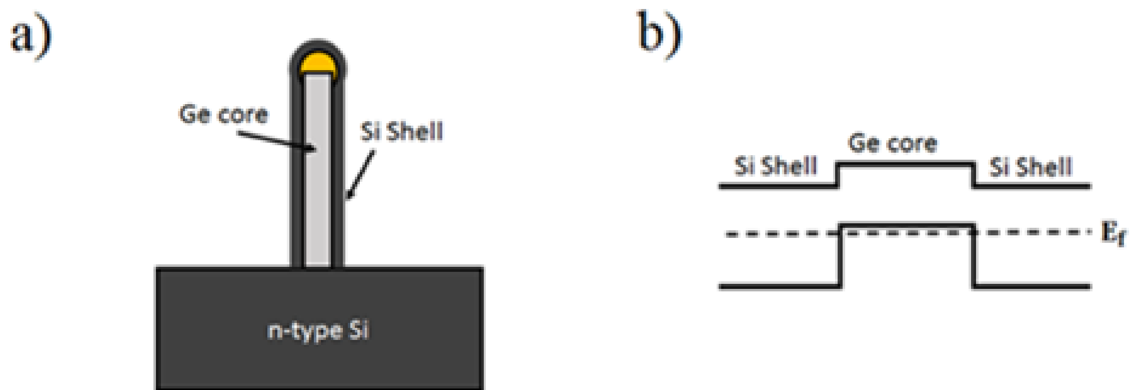

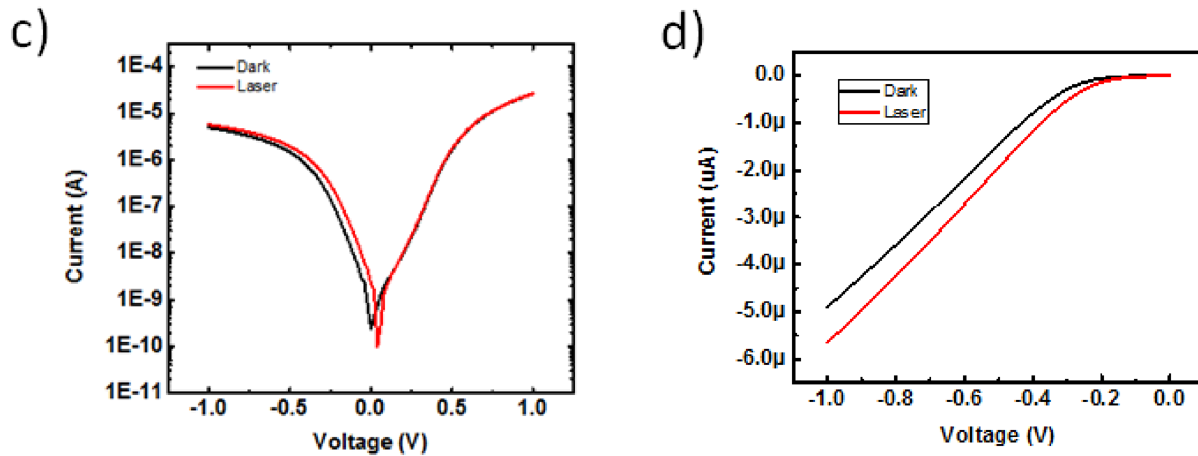

Figure 33: (a) Schematic drawing of core/shell Ge/Si nanowire grown on n-type Si substrate. (b) Band diagram for the core/shell hetero structure. (c) I-V plot of core/shell nanowire in dark and under laser illumination at 1.55um wavelength in log scale (d) I-V plot of core/shell nanowire in dark and under laser illumination at 1.55um wavelength in linear scale.

The core/shell nanowire array detectors were optically excited at 1.55um wavelength using the same setup shown in Figure 18. From the photocurrent measurement shown in Figure 33c, the photocurrent for the core/shell arrays was more than 50X higher than the measured current for Ge core only array devices at similar optical intensity. The higher photocurrent could be related to the increase in surface states as a result of the Si shell. With more electrons trapped at the surface states, more holes are maintained in the nanowire and collected at the contact contributing to an increased overall photocurrent. More quantitative study is needed to understand the full effect of shell thickness on the photo response.

Next, we perform quantitative analysis on the measured photocurrent for the Ge/Si core/shell nanowires, just like we did for the Ge core only nanowire. We begin with the measured photocurrent and obtain the carrier generation rate. Because the core/shell device is made from

arrays of nanowires (~20 nanowires in each array), we will multiple the area and volume of a single nanowire by a factor of 20 in our calculations. The optical intensity for the measurement was 381W/cm^2.

$$I_{ph} = eAG_o(L_p + L_n) \approx eAG_oL_p$$

$$I_{ph} = eAG_o(L_p + L_n) \approx eAG_oL_p = 0.76uA$$

$$G_o = \frac{I_{ph}}{eAL_p} = 3.78 \times 10^{27} cm^{-3}s^{-1}$$

$$\eta = \frac{G_o \times Vol}{P_{opt}/\hbar\omega} = \frac{3.78 \times 10^{27} cm^{-3}s^{-1} \times 20 \times 6.28 \times 10^{-17} cm^3}{2.39 \times 10^{-8} W/(0.8 \times 1.6 \times 10^{-19} J)} = 25.4$$

$$R_\lambda = \frac{i_p}{P_\lambda} = \eta \frac{q}{\hbar\omega} = 31\text{A/W}$$

$$\text{Amplification factor} = \frac{\text{Measured current}}{\text{Theoretical current}} = \frac{0.76\text{uA}}{0.2\text{nA}} = 3800$$

$$Photoconductive\ gain\ (G) = \frac{I_{pc}/e}{P_{abs}/\hbar\omega} = 2778$$

From the calculations, the nanowires with shell show much better photocurrent response, with the current amplification, responsivity and photoconductive gain all higher than the Ge core-only nanowires.

3.6.1 High dark current in core/shell nanowire detector

Another important observation is the increase in the dark current. From Figure 33c, the dark current increased by more than 3 orders of magnitude when compared to the Ge core only device. To understand why this is the case, we referred to previous research done on ref[64]. The addition of Si shell to Ge nanowires creates a quantum well structure as shown in Figure 33b and essentially P+ dopes the Ge nanowire. The increases in the nanowire p-type doping concentration was clearly observed from electrical characterizations of these core/shell nanowires in control

experiments. The higher doping increased the tunneling current which we observe as leakage current.

We performed device simulations to show that this indeed the case. We tried to simulate the effect of the Si shell on the leakage current following the process we did for the Ge core only device. From the simulation, we observed that the tunneling barrier between the Si/Ge heterojunction interface was much narrower than the Ge core only case (Fig. 34b). This implies that the tunneling current will increase significantly, as shown in Fig. 34a.

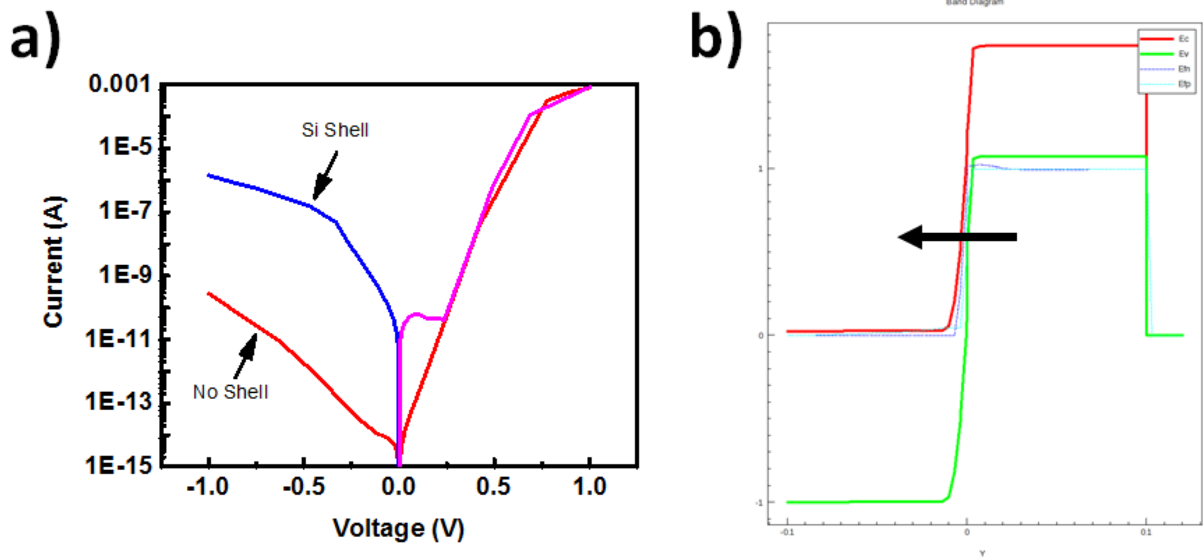

Figure 34: (a) I-V plot showing single Ge nanowire with no shell (red line) and Si shell (blue line). (b) Band diagram of the Ge core/shell nanowire device showing a very narrow barrier at reverse bias of 1V.

A possible method of mitigating the leakage current while maintaining the high photocurrent is by adding an intrinsic layer between the Si substrate and the core/shell nanowire. This can be done by growing the nanowires, then adding a passivation layer such as aluminum

oxide and performing a partial etch of the passivation to expose the upper region of the nanowire for shell deposition.

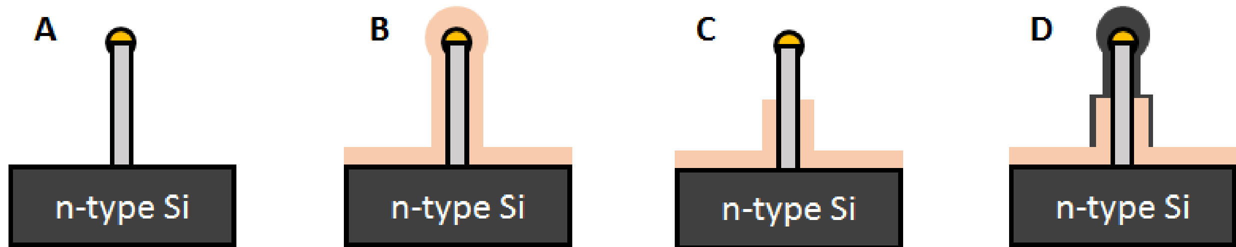

Figure 35: Schematic showing a possible method of creating a reduced doping region between the Si substrate and core/shell nanowire to reduce tunneling current. (a) Ge core only nanowire is grown. (b) Aluminum oxide is deposited. (c) Part of the aluminum oxide is etched away. (d) Si shell is deposited.

3.7 p+Ge/p+Si/Au nanowire array device

Next, we fabricated and measured the nanowire grown on p+ Si substrate. The device structure is based on the formation of Schottky barrier between the Ge nanowire and the Au top contact. The purpose of this device is to test the optical response of Ge nanowire at longer wavelengths. It can be recalled from the band structure of Ge that there is a bandgap of 0.29eV between the split-off band and the degenerate Heavy Hole (HH) and Light Hole (LH) band. In this experiment, our goal is to determine if there are intra band transitions of hole carriers between the Split-off of band and the HH.

The Au/Ge junction has a barrier height of about 0.3eV from experimental measurements. The low barrier allows electrons to gain enough energy to overcome the barrier and be injected from the metal into Ge nanowire at mid infrared wavelengths (MIR). The combination of low Schottky barrier height and the sub bandgap of Ge will lead to two non-competing processes that positively contribute to the photocurrent at MIR range. The performance of this device at mid

infrared region (MIR) such as 3um has not been tested successfully. As of the time of this writing, MIR testing remains an ongoing research effort in our laboratory.

As a preliminary test, this device was excited at 1.55um to compare its performance with the Ge core only and core/shell device. Using the same procedure as we did for Ge core only and core/shell devices, we estimated the quantum efficiency and gain of this device.

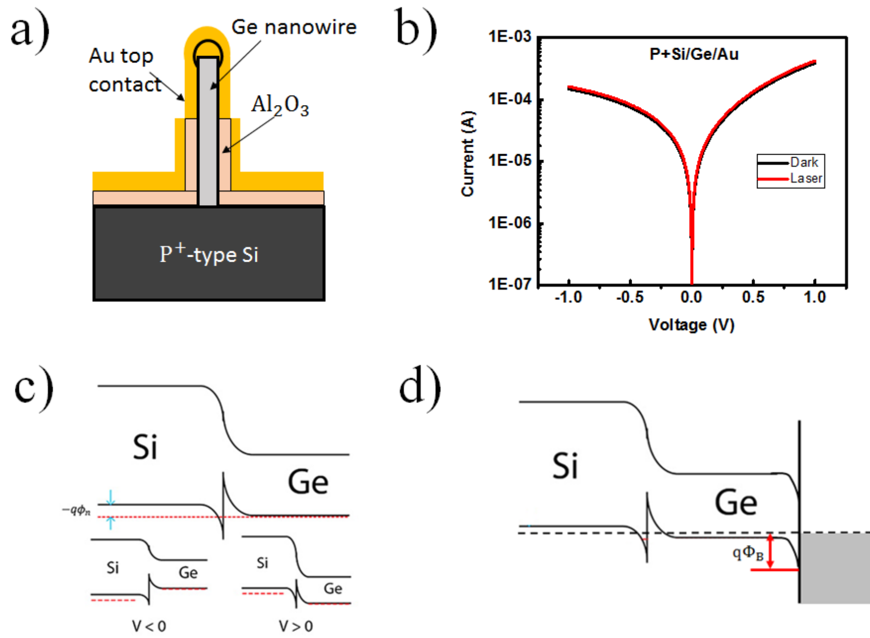

Figure 36: (a) Schematic drawing of p-Ge nanowire grown on p+ Si substrate. (b) I-V plot of p-Ge nanowire in dark and under laser illumination at 1.55um wavelength. (b) Band diagram for the p+/p Si/Ge heterojunction with no bias and under positive/negative bias. (d) Band diagram showing the Schottky junction formed between p-Ge and Au top contact. Figures (c) and (d) are Reprinted with permission from ref[52]. Copyright 2013 American Chemical Society.

$$I_{ph} = eAG_o(L_p + L_n) \approx eAG_oL_p = 12.9uA$$

$$G_o = \frac{I_{ph}}{eAL_p} = 6.42 \times 10^{28} cm^{-3}s^{-1}$$

$$\eta = \frac{G_o \times Vol}{P_{opt}/\hbar\omega} = \frac{6.42 \times 10^{28}cm^{-3}s^{-1} \times 20 \times 6.28 \times 10^{-17}cm^3}{2.39 \times 10^{-8}W/(0.8 \times 1.6 \times 10^{-19}J)} = 431.9$$

$$R_\lambda = \frac{i_p}{P_\lambda} = \eta \frac{q}{\hbar\omega} = 539A/W$$

$$\text{Amplification factor} = \frac{\text{Measured current}}{\text{Theoretical current}} = \frac{12.9uA}{0.2nA} = 64500$$

$$\text{Photoconductive gain (G)} = \frac{I_{pc}/e}{P_{abs}/\hbar\omega} = 47166$$

From our measurements at 1.55um, we observed a very high increase in photocurrent. The photocurrent was 3 orders of magnitude higher than the measured photocurrent from the p-n heterojunction array devices. The I-V plot shows a weakly rectifying diode which should be expected in this case due to the low barrier height. The noise level is extremely high and this reinforces our earlier suggestion that a good p-n junction is essential to maintain a very low dark current in these devices. The possible explanation for the very high photocurrent could be due to the device structure. For the heterojunction devices we examined earlier, most of the electric field drops at the heterojunction as is evident from their band diagram and little field is dropped in the Ge nanowire region where the majority of photo absorption occurs. In the absence of electric field, the photo generated carriers move by diffusion which greatly reduces the number of these carriers collected at the contacts as majority of the carriers will recombine before reaching the contacts.

For the p^+-Ge/p^+ Si/Au device, we can treat this device as purely a photoconductor. The reason is that the Schottky junction is weakly rectifying and almost Ohmic in nature as is observed in the I-V plot in Figure 36b. This means that there is an electric field gradient along the entire device. Under the force of this field, more carriers are driven to and collected at the contacts. At the same time, amplification due to the trapping of electrons which provides the internal

photoconductive gain is still present. The combination of efficient carrier collection and amplification of carriers, leads to the high photocurrent observed in this device.

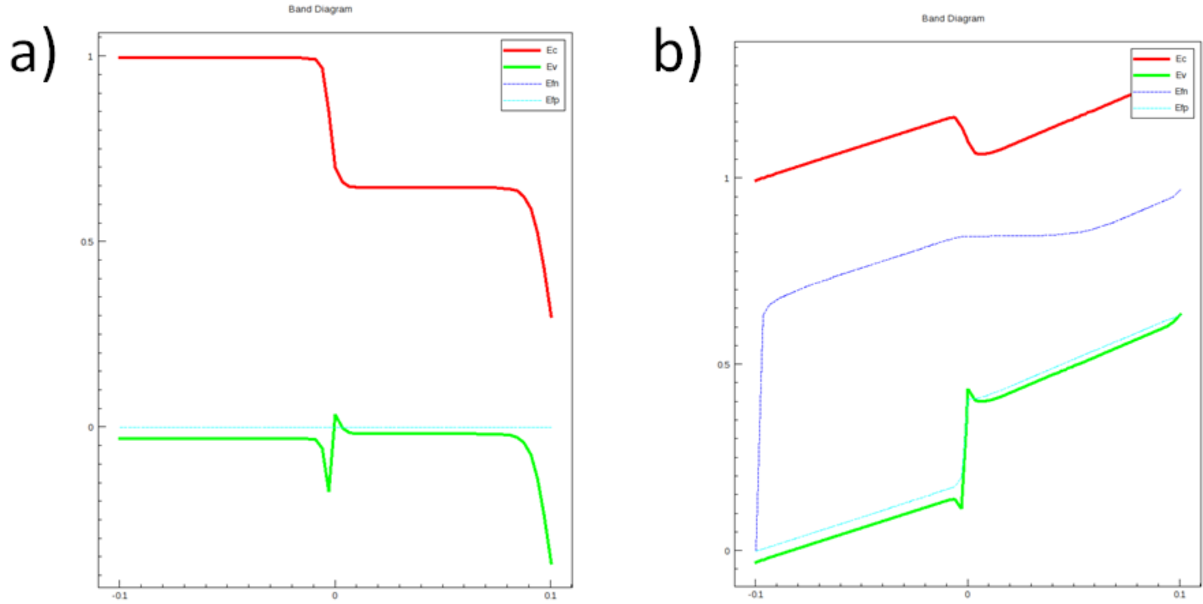

Figure 37: (a) Plot of the band diagram of p+Si/p+Ge/Au device at zero bias. (b) Repeat of the plot of p+Si/p+Ge/Au under -1V bias. Note the Ge/Au contact is biased to –1V while the Si side is grounded.

3.8 Hybrid Schottky Ge/Si heterojunction photodetector

Another structure that we investigated is a combination of a Schottky diode created from a simple low doped n-type Si and nickel (Ni) electrode with embedded free standing Ge core only (p-Ge) nanowires, as shown in Fig. 38a. The device structure for this case under discussion could be considered as two photodiodes connected in parallel. We expected the leakage current of the Schottky diode formed between the electrode and the Si substrate to be the limiting factor for the hybrid device performance. By keeping the device area small for the Schottky diode and using a clean Si interface, we were able to limit the dark current from the Schottky diode to less than 1nA. This means that the dark current of the p-n heterojunction photodetector (< 10nA) becomes the

limiting factor in our hybrid device performance. We estimated the dark current for the Schottky device using the equation:

$$I_s = AA^*T^2\exp(\frac{-q\phi_B}{k_BT}) \quad (38)$$

Where A is the device area, A^* is the effective Richardson constant and T is the temperature in Kelvin.

From equation 23, using effective Richardson constant of $110\ \text{A cm}^{-2}\text{K}^{-2}$, device area of 10um by 2um and temperature of 300K we calculated the maximum dark current to be 4pA. In reality, dependent on surface quality, the leakage current is more than one order of magnitude higher than the theoretical value as is the case with our device.

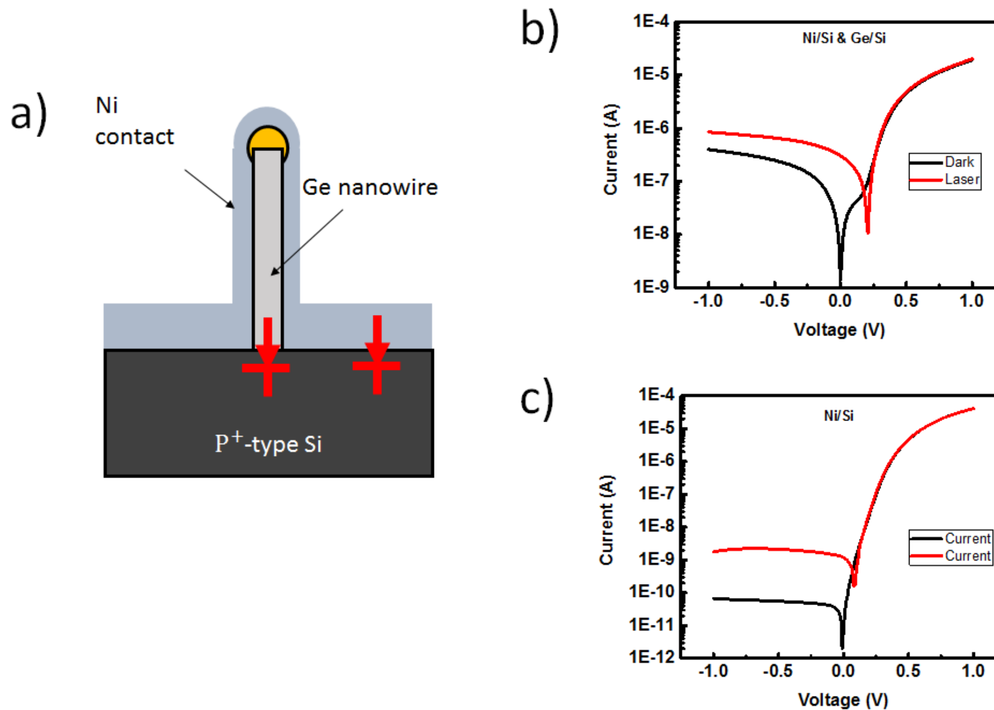

Figure 38: (a) The device schematic with an indication of the multiple junctions formed between the Ge nanowire and the Si substrate and between the Ni and Si substrate. (b) Shows the I-V plot of the hybrid Ge/Ni/Si device in dark and under 1.55um laser excitation. (c) Shows the I-V plot of the Ni/Si schottky device in dark and under 1.55um laser excitation.

The measurement of our reference Schottky diode sample based on the Ni electrode on the Si substrate without the nanowire showed a dark current of less than 100pA. Though this dark current level is higher than the estimated value by several orders of magnitude, it is still within the level that allows us to observe any reasonable photocurrent generated from either the Schottky structure or the p-n heterojunction structure. Note the photocurrent in the Si based Schottky diode is small (~ 1nA) compared to the Ge nanowire based photodetector discussed earlier, despite the much large volume of the Si substrate, and confirming our hypothesis that light absorption in the Si substrate is negligible at 1.55um.

With embedding of Ge nanowires together with the Schottky junction, the photocurrent increased by 3 orders of magnitude (1nA to 6uA). The dark current also increased by a similar ratio as the photocurrent. We attribute the increase in dark current to be as a result of a very short p-n heterojunction due to the close proximity of the Ge contact to the junction.

The main reason we investigated this structure is due to the ease of fabrication which makes it attractive for future integration with existing CMOS structures. Of recent, there has been strong interest in Schottky based detectors due to the extra flexibility of choosing the wavelength detection range of such devices by simply using a metal of appropriate work function with respect to the semiconductor. By adding Ge to the Schottky detector, we have shown that this structure significantly improves the photocurrent detection at 1.55um. The only disadvantage of the hybrid device is the device to device variation due to interface quality. This variation is an undesirable property of Schottky junctions.

3.9 Nanowire solar cell

Lastly, we tested the Si/Ge core/shell device for potential solar cell applications. We expected good solar cell performance due to the unique structure of the nanowires that allowed us to maximize the exposed area. Secondly, we expected a larger spectral response due to a small bandgap of Ge. Essentially, Si/Ge solar cell should be able to respond from the visible spectrum up to 2um wavelength which corresponds to the indirect bandgap of Ge. The combined effect of Ge core and Si shell which will both act as absorption layers in the solar cell device and the previously observed gain in small dimension nanowires was the main attraction to investigate this device.

To fabricate the solar cell structure, core/shell nanowires were grown in a 5um wide and 3.6mm long patterned trenches on a (111) Si substrate. The growth was followed by regular nanowire fabrication as described in section 3.4. Outside the trench area was covered with 120nm Ni layer to prevent additional substrate absorption. To make Ohmic contact around the nanowires, we deposited 15nm of Ni by sputtering. It is important to note that the light reaching the nanowires and the p-n heterojunction (Si/Ge junction) area is less than 5% of incident light because some of the light will be reflected and the thin Ni layer absorbs light very strongly. This does not imply that if all the light was transmitted, the device performance will scale accordingly since we expect the device performance to saturate at some point.

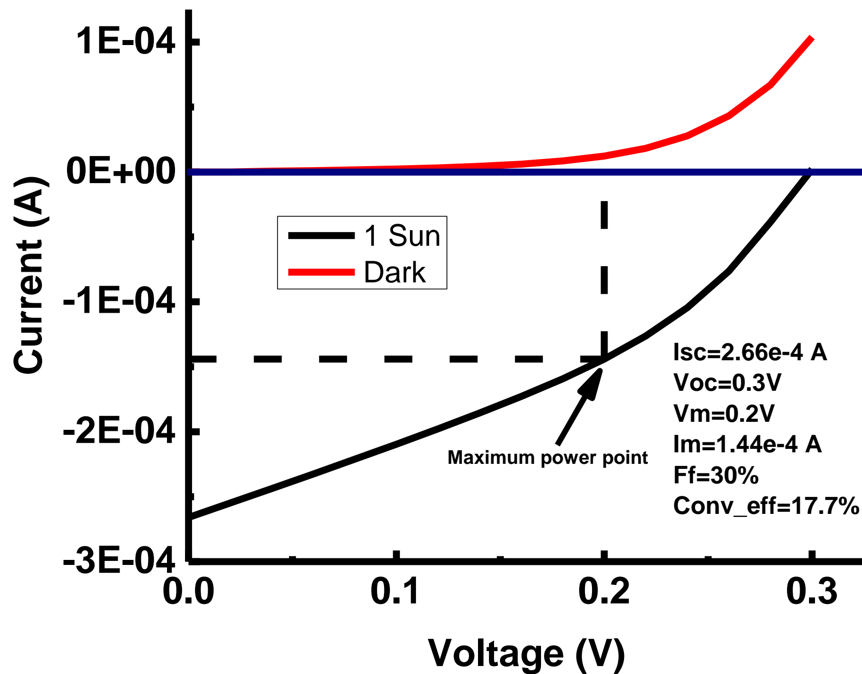

Figure 39: I-V plot of Si/Ge core/shell nanowire array solar cell. The device shows a short circuit current of 2.66e-4A, open circuit voltage of 0.3V and a fill factor of 30%.

After testing the nanowire-based solar cell and analyzing the collected data, we calculated the efficiency of the solar cell to be about 17.7%. The open circuit voltage was 0.3V and short circuit was 2.66e-4A. While this results are only moderate if compared with the solar cell performance of the crystalline Si, it is noteworthy that no optimizations were attempted on this initial study. For instance, we can improve the performance of the device by replacing the Ni electrode with a transparent electrode such as Indium Tin Oxide (ITO). Also, addition of an anti-reflective coating which is a standard practice for most solar cell devices could further improve the device performance. More detailed investigations of Ge nanowire solar cell was not performed because that was not the focus of our research.

3.10 Effect of Substrate Absorption

3.10.1 Substrate Shielding

To reduce substrate absorption, the optical measurements were conducted at a wavelength of 1.55um which is transparent to silicon. This enabled us to use backside laser excitation through the silicon substrate to pump the Germanium nanowires. Never the less, we still carried out detailed control experiments to check if substrate absorption contributed in any way to the photocurrent results that were earlier reported. It is expected that prime-grade silicon substrates used in our study should be transparent at 1.55um due to silicon bandgap at 1.12eV which corresponds to 1.1um minimum absorption wavelength. With the presence of defects, some of which are mid bandgap defects, most materials could potentially absorb photons with energy less than their bandgap. Such absorptions are very weak when compared to inter band absorptions. However, considering the very large volume ratio of the substrate and the nanowire, the effect of substrate adsorption needs to be unambiguously eliminated.

To determine the effect of any substrate absorption, the backside of the substrate was shielded with an optically thick gold layer. A 50um by 50um opening was created to enable laser excitation at the active device regions only. This was done by patterning the backside of the substrate. Alignment marks were placed at the top side of the substrate and photoresist was spun at the backside of the substrate. Using an Infrared (IR) camera available on the lithographic tool, we performed backside alignment to create the openings at the device active areas.

The devices showed no noticeable change in photocurrent after shielding, as shown in Fig. 40a, for unshielded control devices with illumination area of 282743um^2 and shielded devices with openings of 50um x 50um. However, due to the added processing steps in making the back shield,

the majority of the devices were degraded as a result of the experiment. This degradation can be observed from the increase in dark current after the shielding process. The damage to the nanowires could be minimized by decreasing the number of process steps needed to shield the sample.

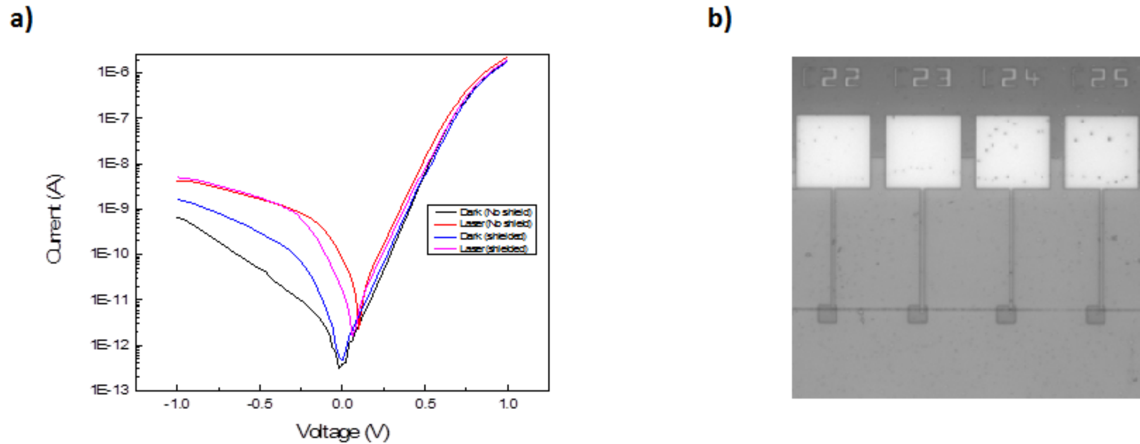

Figure 40: (a) I-V plot of arrays of nanowire photodetector excited at 1.55um with and without the optical back shield with a beam size of 300um diameter. (b) IR image of a back shielded device showing a 50um by 50um opening through which optical excitation of the active region of the device is carried out. The rest of the substrate is completely shielded and should not have any photon absorption.

3.10.2 Schottky diode structure

Another method we used to determine the effect of substrate absorption was to fabricate a Schottky diode structure with a Schottky barrier higher than 0.8eV. The reason for choosing high Schottky barrier is to prevent electrons from gaining enough energy to cross the barrier and contribute to photocurrent. To achieve this goal we choose platinum metal which has a Schottky barrier of 0.9eV with n-type silicon. We also used an n-type substrate with very low doping of 10^{14}cm^{-3}. The low doping allowed us to have very long diffusion lengths of almost 1mm in the silicon substrate. This meant any photo generated carriers within the substrate will have a higher chance of being collected at the contacts.

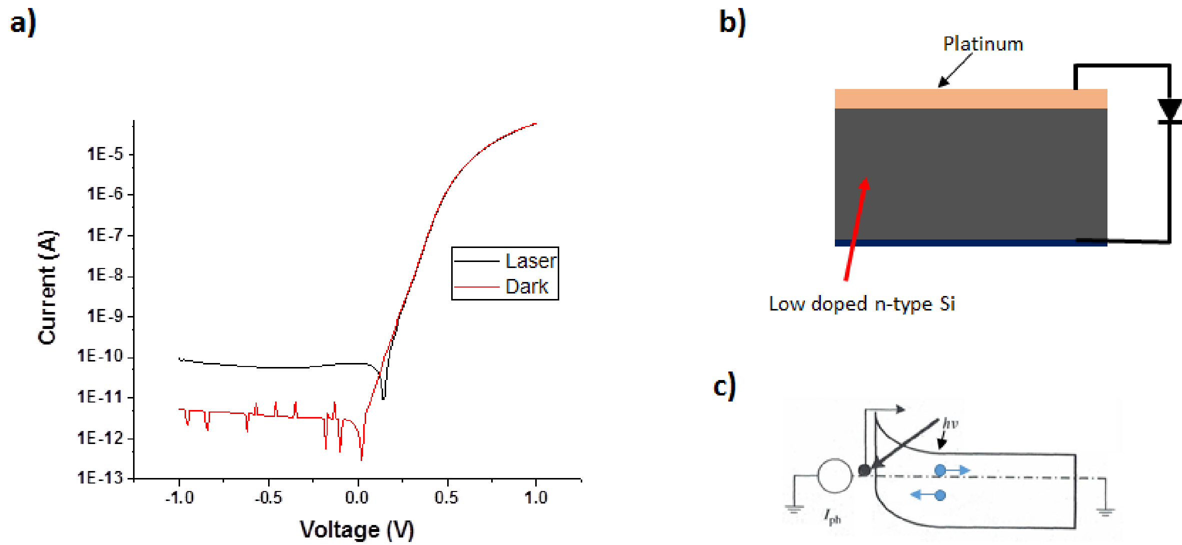

Figure 41: a) I-V plot of Si/Pt Schottky diode in dark and under photo excitation at 1.55um. b) A schematic showing Si/Pt Schottky diode structure. c) Schematic showing band bending due to the formation of Schottky junction and possible carrier absorption mechanisms.

Results obtained from such a Schottky diode are shown in Fig. 41. Considering the results from the Si/Pt Schottky device, the photocurrent generated by both the silicon substrate and possible defect sites within the Schottky barrier was still two orders of magnitude lower than what we observed in our Ge photodetector devices. This experiment helped us to draw a very useful conclusion that the photocurrent measured from the Si/Ge heterojunction device is due to absorption in the Ge nanowire even in single nanowire devices.

3.11 Photodetector device performance

Table 1: Performance comparison for photodetetectors based on various material systems

Material	Responsivity (A/W)	Bandwidth (GHz)	Dark Current (µA)	Photodetector Structure	Year	Reference
InGaAs	1.1@1550nm	-	10^{-6} @0 0.5V	p-i-n	2010	[65]
InGaAs	0.17@1550nm	9	2.5 @ -1V	p-i-n	2012	[66]
InGaAs	0.96 @ 1550nm	4	0.015 @ 5V	MSM	1992	[67]
InGaAs	>0.4 @ 1520-1630nm	-	0.27 @ 1V	MSM	2014	[68]
InGaAs	-	120	0.34 @ 5V	APD	2013	[69]
InGaAs	0.69 @ 1310nm	270	-	APD	2014	[70]
Ge	1.08 @ 1550nm	7.2	0.06 @ 0.1V	p-i-n	2007	[71]
Ge	0.56 @ 1550nm	-	1.08 @ 1V	p-i-n	2013	[72]
Ge	0.53 @ 1550nm	-	0.0115 @ 1V	MSM	2008	[73]
Ge	1.76 @ 1550nm	1.1	412 @ 5V	MSM	2013	[74]
Ge	5.88 @ 1310nm	340	10 @ 25V	APD	2009	[75]
Ge	0.75 @ 1550nm	30	0.184 @ 1V	APD	2013	[76]
Si	0.5-10 @ 1100-1700nm	35	<0.5 @ 60V	MBA	2009	[77]
Si	4.7 @ 1550nm	2	-	MBA	2013	[78]
Si	0.036 @ 1575nm	-	-	SSA	2008	[79]
Si	0.00025 @ 1550nm	-	0.0025 @ -15V	SSA	2009	[80]
Si	0.15 @ 1550nm	1.46	12E-6 @ 5V	IPE	2008	[81]
Si	0.00008 @ 1550nm	>170	0.1 @ 5V	IPE	2010	[82]
HgCdTe	-	7	1.325 @ 63.7V	APD	1997	[83]
HgCdTe	13.1 @ 1550nm	>100	0.066 @ 77.7V	APD	2002	[84]
Graphene	0.0005 @ 1550nm	>100	1.2 @ 4V	MSM	2009	[85]
Graphene	1E+7 @ 1450nm	1	-	Hybrid graphene-QD	2012	[86]
Graphene	0.4-1 @ <1000nm	500	<0.1 @ 5V	Vertical p-n junction	2014	[87]
CNT	0.9-1.8 @ 500-1800nm	-	-	Bolometer p-n diode	2011	[88]
CNT	0.02-0.64 @ 400-1500nm	0.031	-	CNT/C60 Heterojunction	2009	[89]
QD	2700 @ visible-1300nm	2E-8	0.7mA/cm^{-2} @ 100V	Photoconductor	2006	[90]
QD	0.2 @ visible-1600nm	1E-3	<0.1nA/cm^{-2}	Photodiode	2009	[91]
Plasmons	1.081 @ 1550nm	15.6	0.5 @ 1V	Plasmonic electrode	2010	[92]
Plasmons	0.0133 @ 1310nm	-	0.013 @ 0.1V	Plasmonic electrode	2011	[35]

Plasmons	0.049 @ 1550nm	270	<0.1 @ 1V	Plasmonic antenna	2012	[93]
Plasmons	0.1 @ 700nm	-	-	MIM	2011	[94]

Reprinted with permission from ref[58], Copyright 2015, Walter de Gruyter GmbH

Comparing the values in table 1 with our Ge core only single nanowire photodetector, our device outperformed all the Ge detectors listed on the table in terms of responsivity. The highest responsivity reported for Ge devices in the table is 4.7A/W which is about 5 times smaller than our reported responsivity of 25A/W. For the our P^{+}-Si/P^{+}-Ge/Au device, the responsivity of 539A/W is more than 100 times higher than the highest reported responsivity for Ge devices on the table. Higher responsivities was reported for Graphene at 10^{7} for 1450nm wavelength and for quantum dot (QD) at 2700 for visible-1300nm. Considering the dimensions of our nanowires and the ease of integration to already existing platforms, the nanowire photodetector we demonstrated in this research could play a major role for future applications.

3.11 Summary

In this chapter, we discussed the Ge nanowire photodetector fabrication on (111) Si substrate. The Ge core with no shell, the Ge/Si core/shell and the hybrid Schottky/Ge core devices were fabricated and tested. The photodetectors were fabricated in lithographically defined trenches on the Si substrate in order to control the nanowire density and location. By changing the trench width, we controlled the nanowire density within the trench (the wider the trench, the higher the nanowire density). We also discussed the optical measurement setup for the nanowire photodetector. Confocal microscopy was employed in the measurement setup to align the active area of the photodetector to the NIR laser beam and device was excited from the Si substrate side.

Following the successful fabrication of the three devices, each device was optically excited to determine the photocurrent response. The photocurrent data for the Ge core and core/shell devices were further characterized to determine the current gain, quantum efficiency and responsivity of each of the devices. The current gain, external quantum efficiency and responsivity for the Ge core device was 2000, 20.26 and 25.3A/W. For the Ge/Si core/shell photodetector, the current gain, external quantum efficiency and responsivity was 3800, 25.4 and 31A/W. The photodetectors showed very good response to low frequency (10 KHz) modulated laser excitation. The core/shell photodetector device was tested for solar cell performance and it showed an efficiency of 17%.

In order to understand the mechanism responsible for the very high current gain and high responsivity, we stimulated our nanowire structure to check for optical field enhancement around the standing nanowires. The simulation showed electric field enhancement by a factor of 2 around the nanowires. This field enhancement could not account for the high current gain observed in the photodetector device. Based on the high photoconductive gain observed in ZnO and Ge nanowires from previous studies [33][57], we attributed the high current gain in our photodetector devices to electron trapping at the surface states and subsequent long lifetime of holes within the nanowire structure.

We also observed higher reverse current in core/shell devices when compared to none shell devices. This higher reverse current was due to increased tunneling current as the tunneling barrier at the Si/Ge heterojunction decreased due to higher Ge nanowire doping as a result of the shell structure.

Chapter 4

Multi-level memristive optical modulator/encoder

4.1 Introduction

In section 1.2.4 we introduced the concept of using memristors to modulate an optical channel. Memristors are non-volatile memories that rely on the manipulation of ions to achieve different resistance states. In so-called CB-RAM memristors, the movement of metal ions within the active region of the device leads to changes in the resistance state of the device. Low resistance state corresponds to the formation of a metal filament while high resistive state corresponds to the retraction of the filament in the active layer. The major advantage of using memristors for optical applications is the ability to fabricate memristors at the nanoscale and the ability to control optical properties in a nonvolatile fashion.

In this research we have expanded on the work done in ref[44] by demonstrating a multilevel modulating/encoding device based on the asymmetric properties of multiple memristors embedded in a photonic crystal. By the word multi-level, this implies that we can have multiple electrical signals modulating the same optical channel and producing discreet optical signals for each of the possible electrical modulating states. Consider a situation where multiple electrical signals need to be encoded into an optical channel for long haul data transfer. Currently, system designers will rely on multiplexers/de-multiplexers to encode/decode multiple electrical signal channels. For high speed systems, it will be difficult to realize signal encoding/decoding using multiplexers because of their slow speed of operation [95]

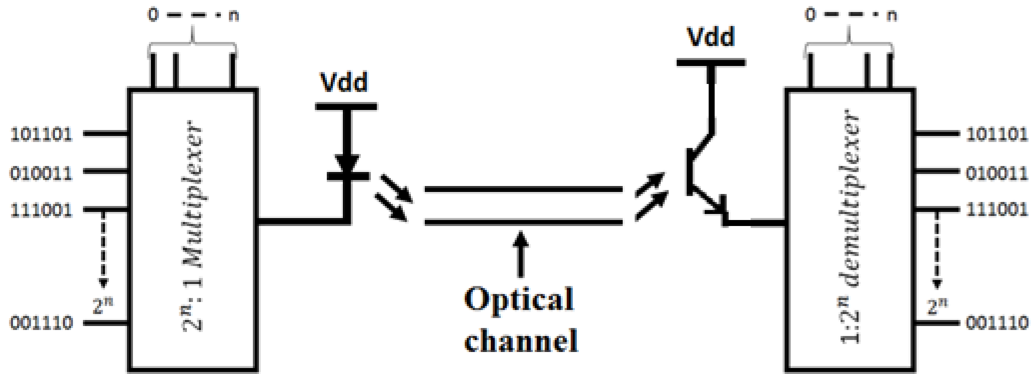

Figure 42: Schematic showing the encoding of multiple digital signal channels into optical signals. The encoder is used to directly drive the laser diode producing optically modulated signal.

Sometimes it is also possible to combine electrical signals with the use of a summing amplifier before encoding into an optical channel. In this case, multiple electrical signals are connected to the inverting/non-inverting input of the amplifier and the output will be the sum of the input signal amplitudes plus an amplifier gain that is dependent on the ratio of the resistors. This method could offer some flexibility in terms of speed compared to the signal multiplexing. However, it is difficult to uniquely distinguish the individual state of each signal after summing.

The optical modulating/encoding device we have demonstrated is able to encode multiple electrical signals into the same optical channel. For every possible combination of the electrical signals to be encoded into optical signal, there is only one optical level that corresponds to that combination. The device could be used to implement a digital signal summer, a multiplexer and an electrical to optical encoder all at an instant without the complex electrical circuitry needed to achieve any of the three name devices.

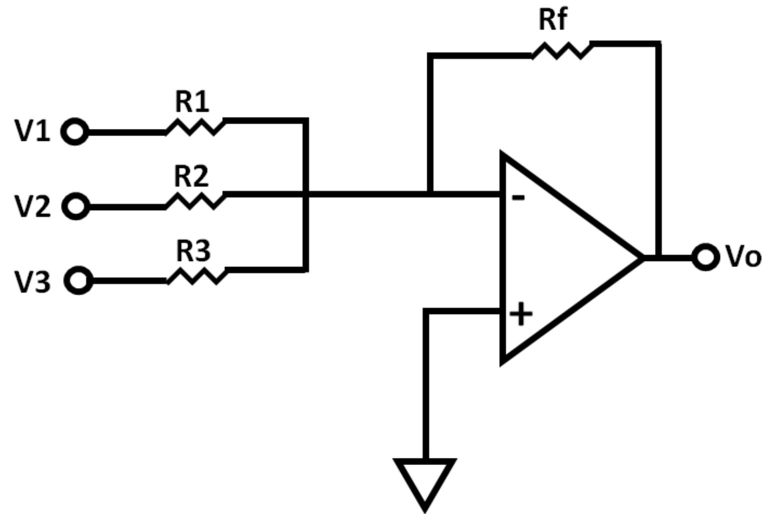

Figure 43: A circuit implementation of a signal summer using an inverting amplifier. The output of the amplifier is the sum of V1, V2 and V3 plus an amplifying factor determined by R_f/R.

Revisiting the earlier explanation of modulators from chapter one, to modulate light, a reversible change in the intensity or phase of the optical signal is needed [96]. In some modulators, a change in intensity is achieved by free carrier scattering or absorption of the incoming optical signal [42], [97]–[100]. Usually a p-n junction is created within the optical channel and electron/hole carriers are either injected or extracted from the junction. The surplus or deficiency of carriers cause a change in both the absorption coefficient and refractive index of the channel material [101]. Since Si is the semiconductor of choice for fabricating electrical devices, it is important to implement Si based modulation for integration with already existing platforms. The major drawback for the free carrier absorption mechanism in silicon is that it is very weak at the optical communication wavelength of 1.55um. This means that the absorbing channel has to be several hundreds of micron to a few millimeters long to cause a significant change to the amplitude or phase of the input beam.

The multilevel optical encoder/modulator we demonstrated consists of two memristors. The operation of the memristor is based on the formation of a silver based filament which represents the low resistance state and the annihilation of such filament which represents the high resistance state[101]–[103]. In our device, these filaments are formed on top of the optical channel. The injected silver ions, which eventually deionize to form silver clusters, serve as extinction centers for the incoming photons, schematically shown in Fig. 44. By further embedding the memristive device in a photonic crystal waveguide, we utilize the local resonances formed within the waveguide to create unique asymmetric extinction centers created by the formation/elimination of the filaments in the memristor devices.

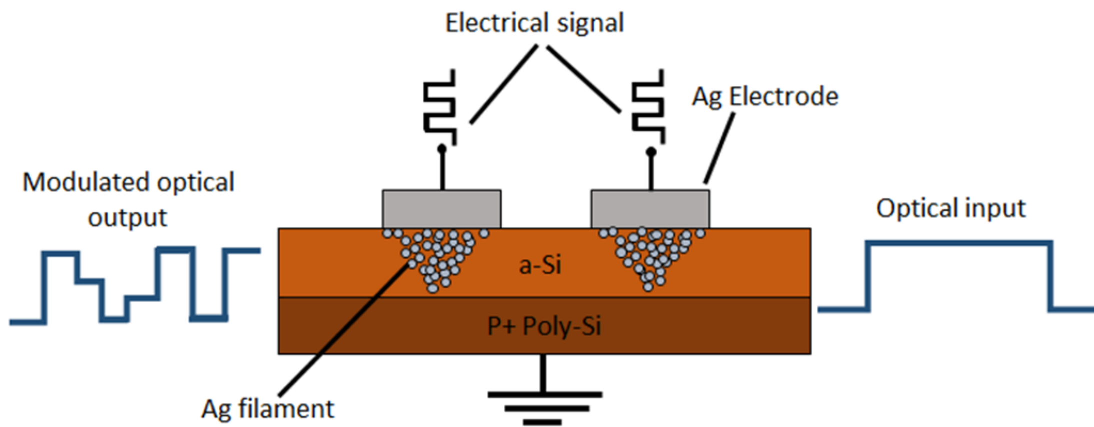

Figure 44: Schematic showing a modulating/encoding optical device that operates with multiple electrical input signals. For each combination of the input electrical signals, a discreet optical state is outputted.

What we refer to as asymmetric behavior is that different memristive states with the same number of filaments will have different optical output level if the filaments occur at different locations within the optical channel. This explains why the “01” state, with the first memristor off and the second memristor on, produces an optical output that is different from the “10” state. The asymmetry created within the system allows multiple filaments to interact with the incoming

photons and a discreet output signal generated for each state of all possible combinations. For our demonstration, we fabricated two memristors along the optical path and the state of these two devices are (00, 01, 10 and 11). Here, (00) state represents no filament formation, (01) state represents first filament formed and second filament unformed, (10) state represents second filament formed and first filament erased and (11) state represents both filaments formed. The addition of photonic crystal waveguide helps to decouple the signal for each state into unique optical signal level.

4.2 Modulator/encoder simulation

Before fabrication and testing of the multilevel modulating device, we ran 2D and 3D simulations to determine optimal design parameters such as length of the filament, thickness of the waveguide needed to support a fundamental optical mode and the input coupler. For the materials, we used a combination of heavily doped poly silicon (poly-Si) and intrinsic amorphous silicon (a-Si) to form our device layers. We used the refractive index of 0.14+11.4i from ref[104] for the silver filament and the electrode during the simulation. The heavily doped p-type (Boron doped) silicon was used as an Ohmic contact to the devices while the a-Si layer served as the active layer for memristor switching. Electrically, the a-Si layer and poly-Si layer are distinct due to the difference in doping concentration as well as the atomic orientation. Optically, by considering that the indices of a-Si (n=3.5) and poly-Si (n=3.44) are closely matched, these two layers can be treated as the same for optical considerations. Therefore both the a-Si and poly-Si layers are part of the waveguide layer. It is important to note that the heavily doped poly-Si will increase the optical absorption along the waveguide but to mitigate these loses we kept the length of the waveguide to a few millimeters.

4.2.1 Grating coupler design

The poly-Si layer was chosen to be 70nm and the a-Si layer to be 50nm to allow successful memristor operations. Due to the thickness of our structure (120nm), we could not efficiently couple light into the waveguide through butt coupling. The size mismatch between our waveguide and the input single mode fiber is also too large to achieve any reasonable light coupling between the former and the later. In order to improve the coupling efficiency, we opted to use a grating coupler.

The use of grating coupling for light input into the device served as a coupler and filter. As will be explained in detail in the proceeding sections of this chapter, our device makes use of photonic crystal (triangular lattice type) waveguide structure which guides only a particular type of linearly polarized light. The grating coupler acts as a filter by coupling only the TM polarized light into the waveguide. Using the grating as a filter eliminated the strict requirement of maintaining a particular polarization into the waveguide. By simply adjusting a polarization controller, we can monitor the output coupled light until a maximum is reached, which indicates that the light is almost perfectly polarized in the direction required by the grating coupler.

Next, we stimulated the grating coupling into the photonic crystal waveguide using the equation:

$$m\frac{\lambda}{a} = n_{eff} - n_{cladding}\,\mathrm{Sin}(\theta) \tag{39}$$

Where

λ is the wavelength of the coupled light source, a is the pitch of the grating coupler, m is the refractive order with integer values of 1 or greater, n_{eff} is the effective index of the waveguide and θ is the incident angle of the coupled light.

From equation 38, we were able to design a grating coupler with a pitch of 1um, duty cycle of 0.66, θ of 13.2º, thickness of 0.12um and a coupling efficiency of 25% using a commercial-grade simulator based on the finite-difference time-domain [105]. The optimization was done using a 2D coupler design. The maximum coupling efficiency dropped to 10% when simulated in 3D.

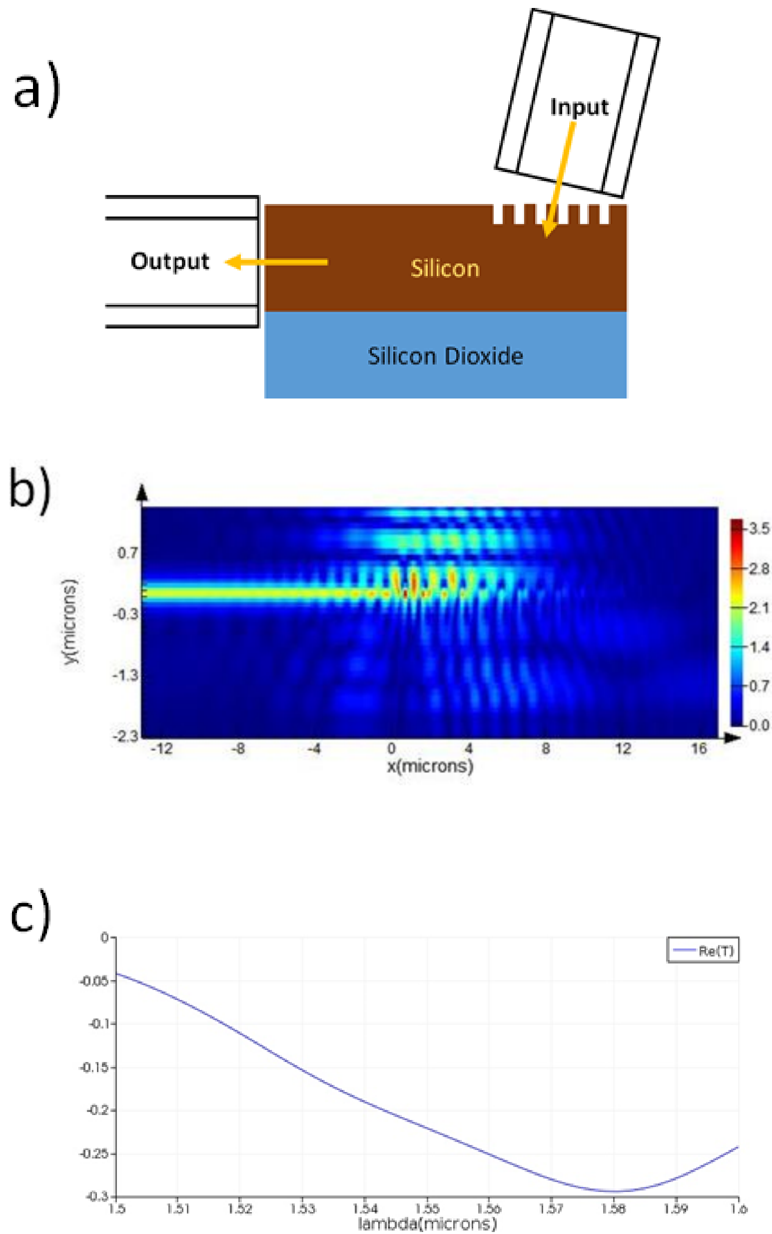

Figure 45: (a) Schematic of grating coupler. (b) 2D simulation of 2D grating coupler. (c) Output transmission versus wavelength of 2D grating coupler.

4.2.2 Photonic crystal simulation

Similarly, the photonic crystal was designed for a planar 3D triangular lattice. Choosing a lattice constant (a) of 0.5um, hole radius of 0.3a (0.15um) and a slab thickness of 0.6a (0.3um), we simulated one unit cell of the triangular lattice, applying Bloch boundary conditions assuming lattice periodicity from Bloch theory. The band structure of the photonic crystal was determined by plotting the angular frequency as a function of wave vector (k) for the frequencies of interest using the software from ref[105]. After careful optimization to minimize slab thickness while maintaining a bandgap at 1.55um wavelength, an optimal design for the photonic crystal was achieved. We were able to design a photonic crystal waveguide with a lattice constant of 0.5um, etched hole radius of 0.11um and thickness of 0.12um with a bandgap at 1.55um wavelength. We have skipped the detailed explanation of the physics of photonic crystals in this thesis because such information are well explained in different texts such as ref[15]. The reader may reference those texts for more in depth understanding of such physics. We are primarily concerned with the experimental and simulation results of the photonic crystals due to the nanoscale requirements of our design.

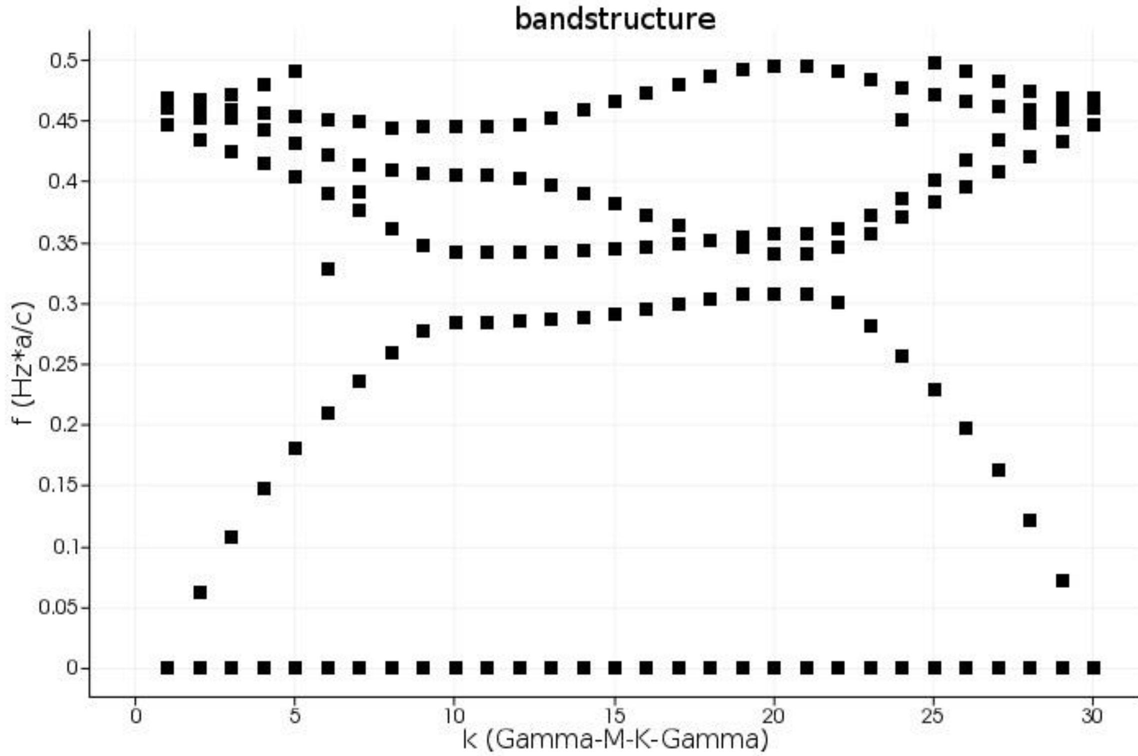

Figure 46: Band structure of a photonic crystal with a lattice constant of 0.5um, etched hole radius of 0.11um and a slab thickness of 0.12um.

The band structure simulation result showed that the photonic crystal has a very narrow bandgap at 1.55um. We observed that the band structure narrowed as the slab thickness was reduced. We had to adjust other parameters such as the etched hole radius in order to maintain a reasonable bandgap at the wavelength of interest. Next, we created the photonic crystal waveguide by creating a defeat line within the photonic crystal. This was done by removing a row of etched holes from the photonic crystal. Further simulation of the waveguide showed very good guidance of the linearly polarized light, as shown in Fig. 47b.

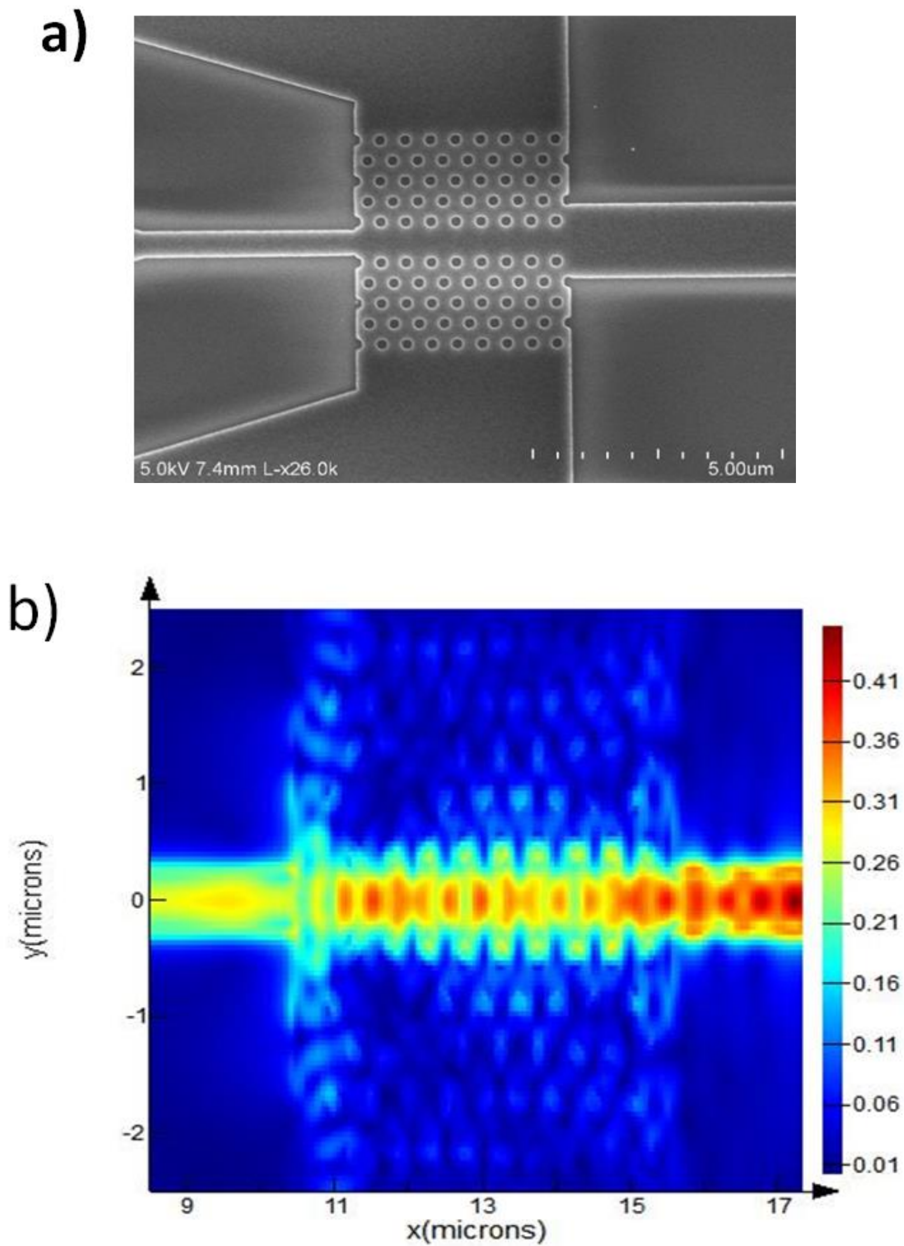

Figure 47: (a) SEM image of fabricated Si photonic crystal waveguide. The left side is the input of the waveguide (0.5um wide). (b) Simulation image of the same photonic crystal waveguide. The fundamental mode is clearly well confined to the waveguide path.

4.3 Modulator/encoder fabrication

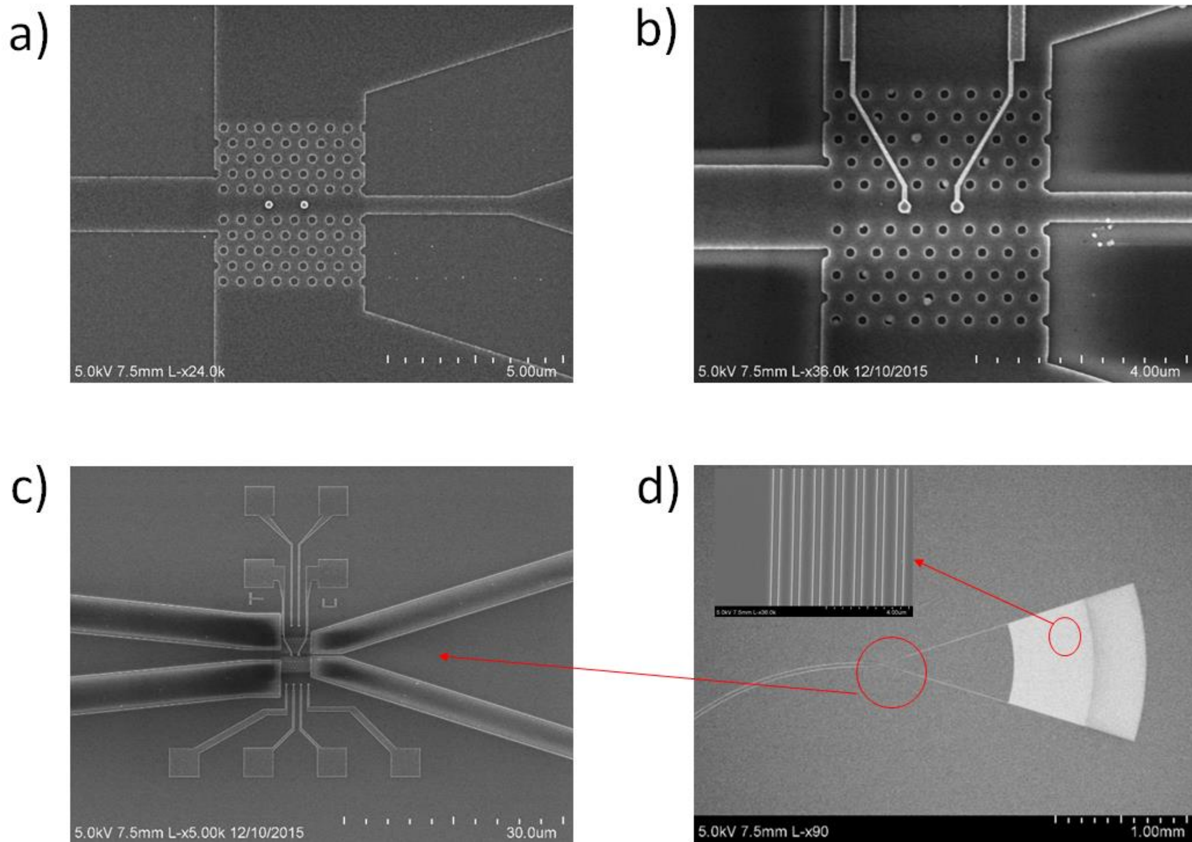

Figure 48: (a) SEM image after photonic crystal waveguide and memristor fabrication (waveguide input from right). (b) SEM image after the addition of external contacts. (c) Zoomed out image of the full fabricated device. (d) Zoomed out image showing the grating coupler and the output waveguide.

The device fabrication started with the deposition of 70nm thick heavily doped (p-type) poly silicon layer on top of a 2um thermally grown oxide layer on a silicon substrate. The deposition was carried out in a LPCVD chamber at 590ºC. The layer had a resistivity of 0.01Ω.cm. On top of the poly silicon layer, we deposited a 50nm intrinsic amorphous silicon (a-Si) layer (SiH_4:He = 5 sccm:45 sccm at 260 ºC, 1.75 Torr). Using electron beam lithography (JEOL), we defined the photonic crystal waveguide with hole sizes of 220nm diameter together with the grating coupler (grating period of 1um and 66% duty cycle) and the input/output waveguides. Next

we etched the defined pattern using reactive ion etching (RIE) and using the underlying 2um oxide as etch stop. Oxygen plasma treatment was used to remove left-over carbon deposits from the etch step. We defined the top electrode along the photonic crystal waveguide using E-beam lithography and deposited 50nm of silver capped with 30nm of Palladium followed by a lift-off process. A 10nm of aluminum oxide was deposited using atomic layer deposition (ALD) as an insulating layer for the external contacts. Three more lithography steps were carried out to expose the top and bottom electrodes. Finally, 90nm of palladium was deposited followed by lift-off process to make the external contacts.

The final structure included the addition of two silver electrodes at the lattice sites within the waveguide, separated by two lattice constants. The purpose of these electrodes is to inject the Ag ions into the waveguide to enable memristor operations by applying an electrical bias to the electrodes, and to move the Ag nanoparticles to either enhance or annihilate the modulating filament.

4.4 Modulator physics

Next, we examine the physics responsible for the optical modulation observed in our device. For simplicity, we assume that the injected Ag ions de-ionized to form completely spherical Ag clusters (nanoparticles). In our device, the Ag clusters serve as extinction centers for the incoming optical beam[106]. The extinction factor accounts for both scattering and absorption of the incident optical beam by the Ag clusters [106]. Without the contribution from the nanoparticle extinction centers, there is still a strong coupling between the Ag electrodes and the optical beam in the form of surface Plasmon Polaritons (SPPs) and this coupling accounts for the strong optical attenuation experienced before filament formation in the waveguide. The combination of steady state coupling to the electrodes and the electrically controlled extinction

from the nanoparticles is responsible for the observed device characteristics. Following the work done in refs[106], [107], we can examine the electromagnetic field (quasi-static near field) coupling in the form of SPPs on the surface of Ag spherical nanoparticles. The quasi-static approximation assumes in-phase oscillations for the entire surface of the spherical nanoparticles and is valid for particle sizes far smaller than the metal's skin depth which is the case for the Ag nanoparticles simulated in our device[106]. With the assumed quasi-static approximation we can write the electric field in terms of the potential which must satisfy the Laplace equation:

$$\mathbf{E} = -\nabla\Phi \tag{40}$$

$$\nabla^2\Phi = 0 \tag{41}$$

Where

∇ is the gradient, Φ is the potential and $\mathbf{E}$ is the electric field.

For a spherical nanoparticle, we can rewrite the Laplace equation and its solutions in spherical coordinates as follows:

$$\left(\frac{1}{sin\theta}\frac{\partial^2}{\partial\varphi^2} + sin\theta\frac{\partial}{\partial r}\left(r^2\frac{\partial}{\partial r}\right) + \frac{\partial}{\partial\theta}\left(sin\theta\frac{\partial}{\partial\theta}\right)\right)\frac{\Phi(\varphi,r,\theta)}{r^2 sin\theta} = 0 \tag{42}$$

$$\Phi(\varphi,r,\theta) = \sum_{i,j} k_{i,j}.\,\Phi_{i,j}(\varphi,r,\theta) \tag{43}$$

Applying the boundary conditions and enforcing the continuity requirements of the normal and tangential electric fields, the potential and the electric field inside ($\Phi_1, \boldsymbol{E}_1$) and outside ($\Phi_2, \boldsymbol{E}_2$) the spherical nanoparticles can be determined and we have stated them below based on ref [106]:

$$\Phi_1 = -\mathrm{E_o}(\mathrm{r}\cos\theta)\frac{3\varepsilon_2}{\varepsilon_1 + 2\varepsilon_2} \tag{44}$$

$$\Phi_2 = -E_o r\cos\theta + E_o a^3 \frac{\cos\theta}{r^2}\frac{\varepsilon_1 - \varepsilon_2}{\varepsilon_1 + 2\varepsilon_2} \quad (45)$$

$$\mathbf{E}_1 = \frac{3\varepsilon_2}{\varepsilon_1 + 2\varepsilon_2}\mathbf{n}_x \quad (46)$$

$$\mathbf{E}_2 = E_o\left(\frac{\varepsilon_1 - \varepsilon_2}{\varepsilon_1 + 2\varepsilon_2}\frac{a^3}{r^3}\right)(2\cos\theta\mathbf{n}_r + \sin\theta\,\mathbf{n}_\theta) + E_o(\cos\theta\,\mathbf{n}_r - \sin\theta\,\mathbf{n}_\theta) \quad (47)$$

From Equation 47, it is evident that the first term represents the scattered electric field and that the field inside the nanoparticle is uniformly distributed[106]. The strong field confinement within the surface induces a radiative dipole from which scattering cross-section could be determined[106]. Again, the equation for polarizability, scattering and absorption cross-section are stated below from ref.[106]:

$$\alpha(\omega) = 4\pi\varepsilon_o a^3 \frac{\varepsilon_1(\omega) - \varepsilon_2}{\varepsilon_1(\omega) + 2\varepsilon_2} \quad (48)$$

$$\sigma_{scattering} = \frac{k^4}{6\pi\varepsilon_o^2}|\alpha(\omega)|^2 \quad (49)$$

$$\sigma_{abs} = \frac{k}{\varepsilon_o}\mathrm{Im}(\alpha(\omega)) \quad (50)$$

Where

$\alpha(\omega)$ is the polarizability, σ_{scatt} is the scattering cross-section and σ_{abs} is the absorption cross-section.

Some notable observations from the scattering and absorption equations is the strong dependence on the surrounding material as well as the size of the particle. Absorption is the dominant extinction factor for small particles while scattering dominates for larger particles.

Scattering is enhanced for particles surrounded by a high refractive index as the scattering cross-section scales by the fourth power of the wave vector of the surrounding medium. Beyond the scattering and absorption by the nanoparticles, it is important to note the effect of light coupling between the nanoparticles close to the electrodes into surface SPP waves on the electrode surface[108]–[110]. Nanoparticles acting like strong coupling centers to the electrodes have been shown in many previous studies[111].

4.5 Simulation results of full modulator/encoder

4.5.1 Nanoparticle absorption

To analyze the effects of the nanoparticles on light propagation in the waveguide, we ran a simulation to show field coupling around 5nm nanoparticle injected from a silver electrode within the photonic crystal waveguide. The plot of the field along a cross section in the XZ direction is shown in Fig. 49 for the number of particles ranging from 1 to 1000.

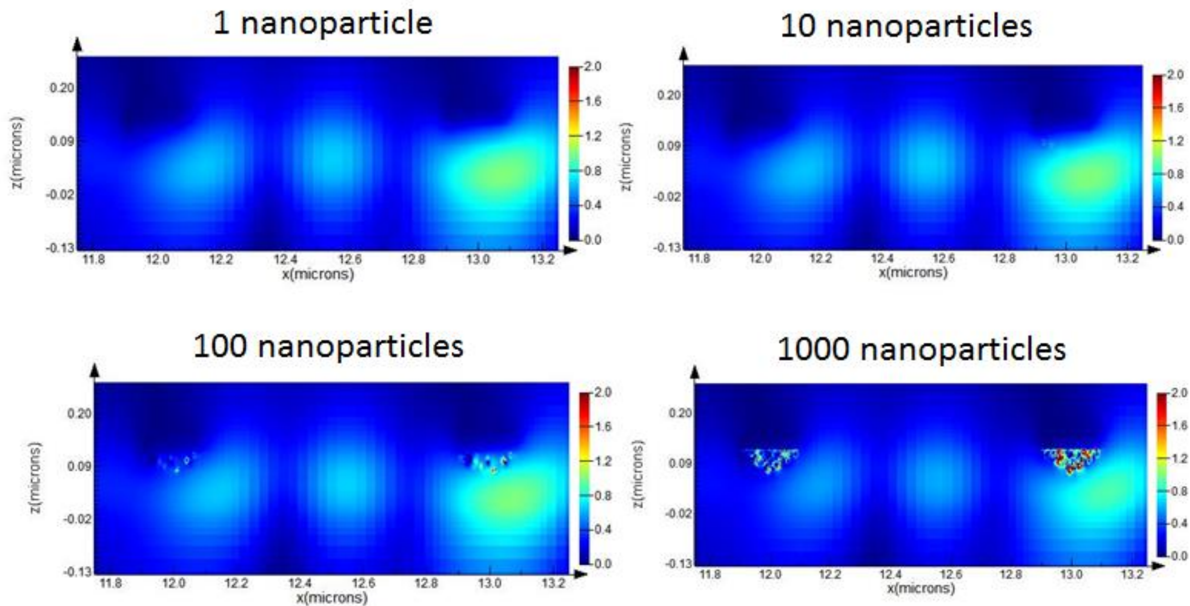

Figure 49: 2D plots of field coupling around 5nm particles embedded in a photonic crystal waveguide. The number of nanoparticles range from 1 to 1000.

From the 2D plots shown in Figure 49, the nanoparticles show very strong coupling effect as expected. The coupling to the individual nanoparticles increases as more particles are injected into the waveguide. This could be due to antenna effect from the other particles where radiating/scattered field from nearby nanoparticle enhance the absorption of its neighbors. From the discussion in the previous section, scattering is enhanced when a particle is surrounded by a high refractive index material. This can explain why the field profile around individual nanoparticles is stronger when surrounded by other nanoparticles. It is interesting to observe that starting from 10 nanoparticles, a noticeable effect is seen in the field profile around the nanoparticles.

4.5.2 Effect of filament size on modulator response

We continue with our device study by simulating the effect of filament/electrode diameter on the transmitted power through the waveguide. Figure 50a shows the different possible memory states “00”, “01”, “10” and “11” for our device. As previously stated, a “zero” represents no active filament and a “one” represents an active filament. For this simulation, the memristors were separated by two lattice constants (2a) from each other. For simplicity and faster simulation, we used Ag cones to represent the filaments. A more realistic simulation was further carried out using 5nm silver nanoparticles as the filament and the results of the two simulations showed reasonable agreement.

Starting with a 100nm filament diameter (Figure 50b) we simulated the four possible memory states. At this filament diameter, there was very small separation between the transmitted optical powers for the four states. The effects increases as the diameter of the filament increases, and in the case of 300nm filament diameter, the “00” state showed clear separation from the other

three states while the “01”, “10” and “11” states remained close to each other as can be observed in Figure 50d. Increasing the filament size to 400nm and 500nm showed very small separation between the states. The optical response for the 400nm and 500nm was one order of magnitude lower than the 100nm, 300nm and 300nm. The 200nm filament diameter had the most distinct separation between the different memory states (Figure 50c). The case of the 200nm filament could be explained as a result of enhanced coupling between the optical waves travelling along the waveguide, the filament and the top electrode since the electrode and filament sizes match the radius of the etched hole of the photonic crystal. We based our design on the 200nm filament size since it had the most desirable optical response compared to the other sizes.

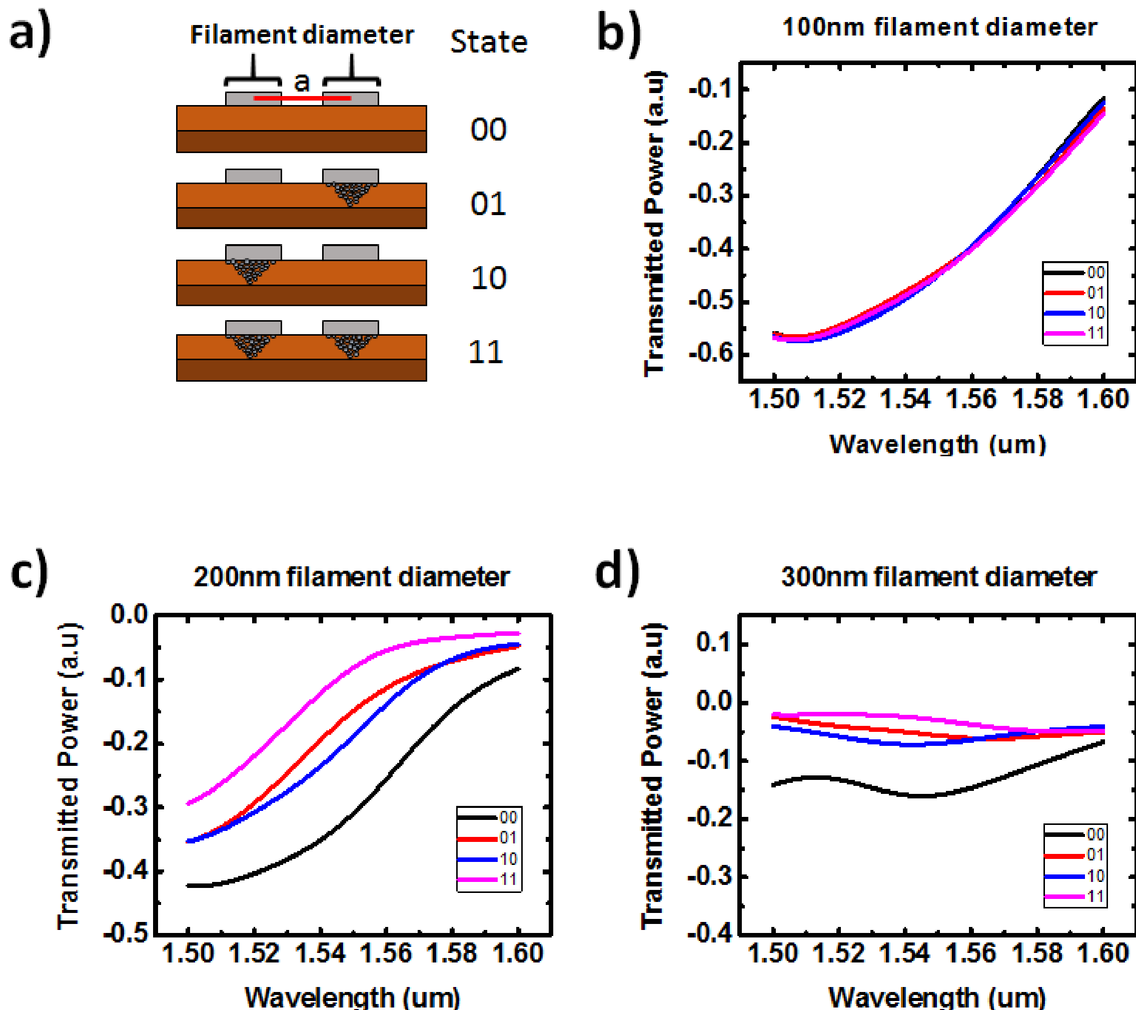

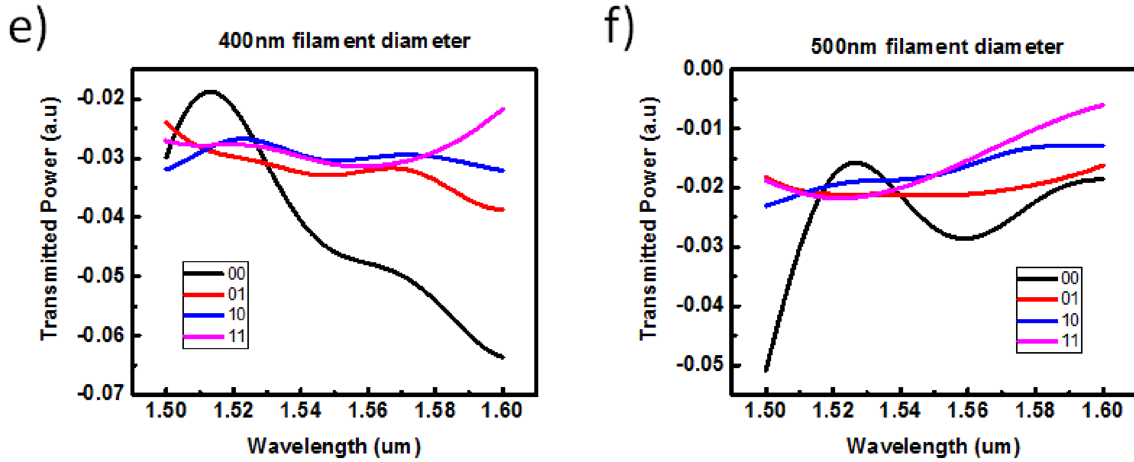

Figure 50: (a) Device schematic showing how the filament size is controlled by the diameter of the silver electrodes. The spacing indicated as "a" corresponds to one lattice length of the photonic crystal. (b)-(f) Plots of the simulated transmitted light through the modulator with respect to wavelength for each of the possible states using a 100nm, 200nm, 300nm, 400nm and 500nm filament sizes.

4.5.3 Effect of filament separation on modulator response

Furthermore, we simulated the effect of the location of the filaments along the waveguide by integer multiples of the lattice constant (1a, 2a) and also by non-integer multiples of the lattice constant (1.5a, 2.5a). We observed that the optical output patterns were similar when the two filaments are at identical lattice points. The plots in Figure 51 clearly shows that Figures 51a and 51c show similar patterns while Figures 51b and 51d show similar patterns. This observation could be very useful to future design engineers because specific modulating response could be attained by choosing the location of the electrodes that form the filaments.

The reason for different optical output patterns when the filament is placed at half lattice points versus full lattice points is due to the different interference patterns at these locations. Mostly uniform local resonance points are formed along the photonic crystal waveguide and these resonances repeat at equal distances from each other. When filaments are placed at points such as

half lattice points or full lattice points away from each other, the light scattering patterns will be similar. This explains the uniformity seen in Figure 51.

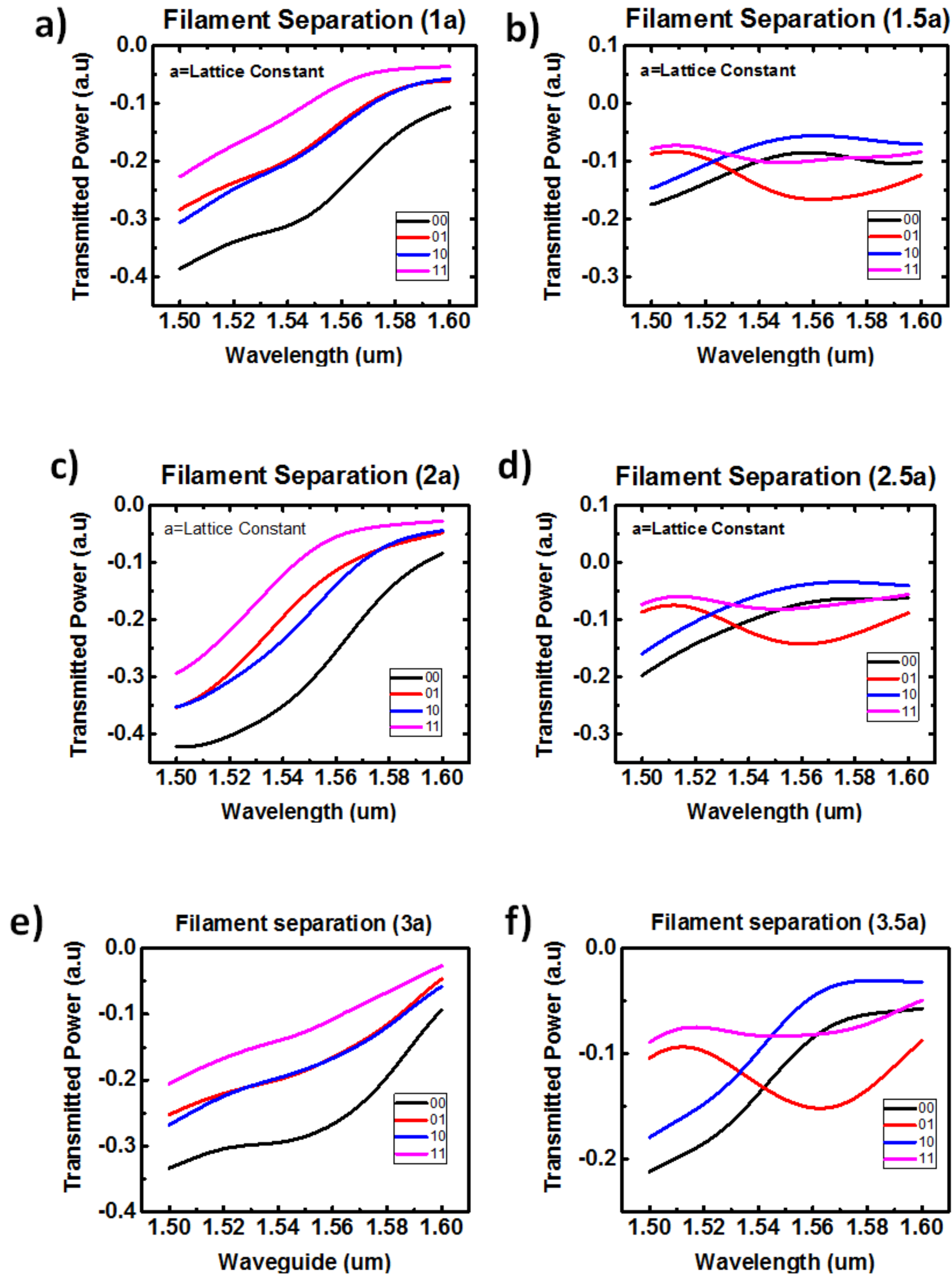

Figure 51: (a), (b), (c) and (d) Plots of transmitted power for different device states (00, 01, 10 and 11) for a filament separation of 1 to 2.5 lattice constant. The 01 and 10 are almost completely coupled for the 1a separation but shows stronger decoupling for the 2a separation. 1a and 2a separations have similar response and the same for 1.5a and 2.5a separations.

4.5.4 Effect of photonic crystal waveguide on state decoupling

Reconsidering Figure 50c, the "01" and "10" states are structurally identical with one filament and two electrodes each. Yet, the optical outputs are different. We tried to explain this observation by carrying out further simulations with a rectangular waveguide. We observed that without the photonic crystal waveguide, the optical output of the "01" and "10" states are almost completely indistinguishable. However, in a photonic crystal waveguide, they become completed decoupled at certain wavelengths. One possible explanation is that the filament interactions within the photonic crystal could be considered as an additional defect within the photonic crystal waveguide and the location of such defect creates special extinction centers that are unique to only that location. Previous works have intentionally created such asymmetric properties in photonic crystal waveguide by adding special defects within the crystal, thereby breaking the spatial symmetry of the structure[100]. The simulated device with and without the photonic crystal waveguide is shown in Figure 52.

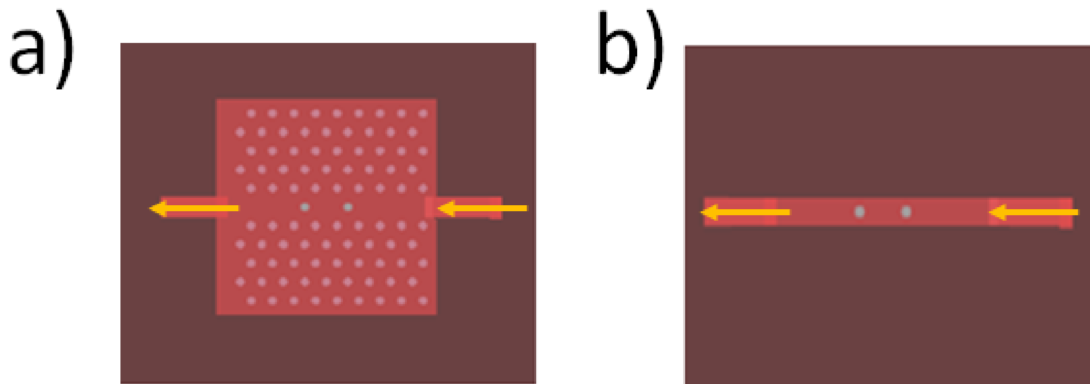

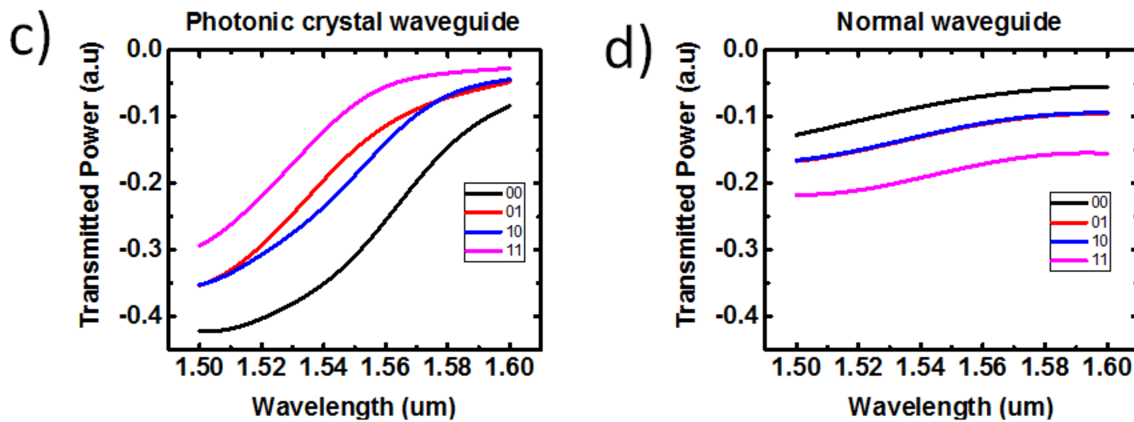

Figure 52: (a) Schematic of the photo crystal waveguide based device. (b) Schematic of the planar rectangular waveguide simulated device. (c) Plot of transmitted power versus wavelength for the photonic crystal waveguide based memristive modulator/encoder. (d) Plot of transmitted power versus wavelength for a rectangular waveguide based modulator/encoder.

4.7 Electrical and optical measurement

Electrical measurements on the devices were performed using the Keithley 4200 semiconductor characterization equipment. The memristor filaments were formed by sweeping the voltage from 0V to 9V while keeping the current compliance to about 0.5uA. To erase the devices, the bias voltage was swept from 0V to -3V. Both the forming and erasing steps may require multiple sweeps. Using the maximum switching voltage of 9V from figure 54 and measured current of 0.5uA, the switching power of the memristors is about 4.5uW. The optical measurement was performed by coupling light from a 1.55um single wavelength laser into a single mode fiber. A polarizing plate was used to linearly polarize the beam in the single mode fiber and the output was coupled through a quarter wave plate into a polarization maintaining fiber terminated by a collimator. The collimated linearly polarized light was incident on the grating coupler of our device at an angle of 13° which is our optimal angle for light coupling into the grating.

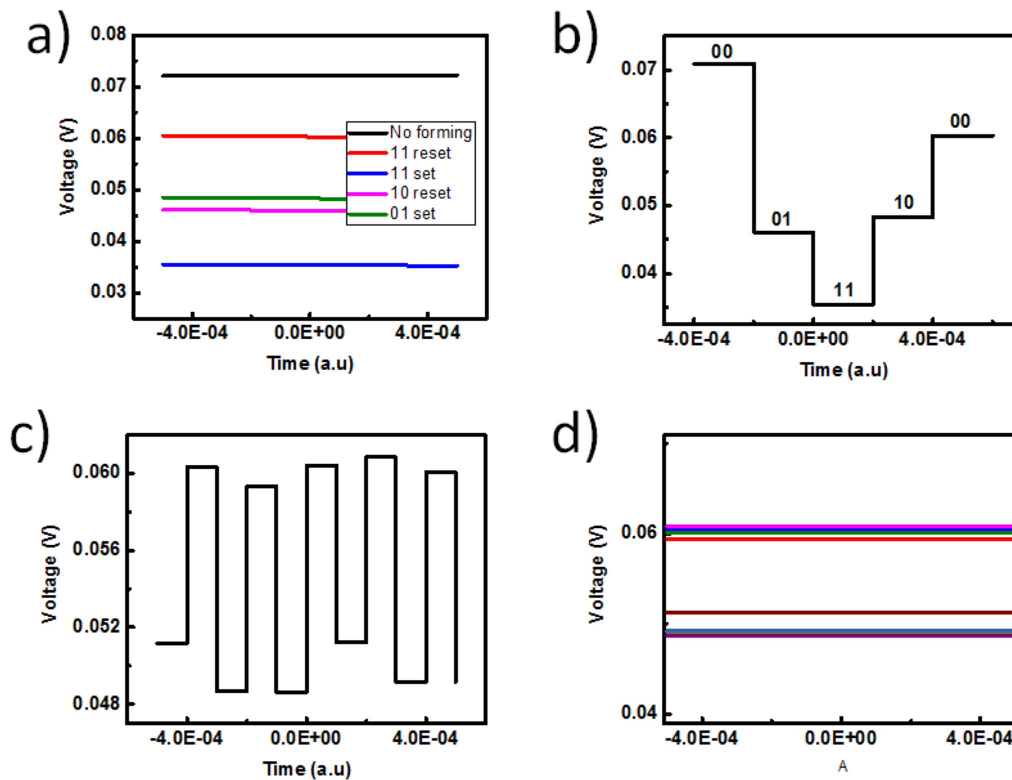

Figure 53: (a)-(d) Plot of measure optical output after each set and reset cycle of the memristor. The measured optical output was converted to current output by the photodetector and measured as voltage levels on the oscilloscope.

The light output from the device was measured to be 7.5uW which corresponds to a measured voltage of 0.072V on the oscilloscope before filament formation. Following the initial optical output, we formed the memristors to the "01" state and measured the optical output again, the voltage dropped to 0.045V. The same procedure was used to measure the "11", "10" and "00" states. The results are summarized in Figure 53. Figures 54a and 54c show the forming of the first and second memristors while Figures 54b and 54d shows the erasing of the first and second memristor to return the two memristor devices back to "00" state (both filaments erased). The memristor I-V plots show clear hysteresis and abrupt resistance changes as expected[101], [103], [112], [113]. The measured optical output showed different measured optical intensities based on

the active filaments of the memristors. However, the separation between the “01” and “10” states were not as large theoretically predicted. After both filaments were erased, the optical output increased but never returned to the pre-forming level. The reason for this observation could be because some of the Ag nanoclusters were not completely extracted out of the optical channel, as has been observed in similar memristor devices [102].

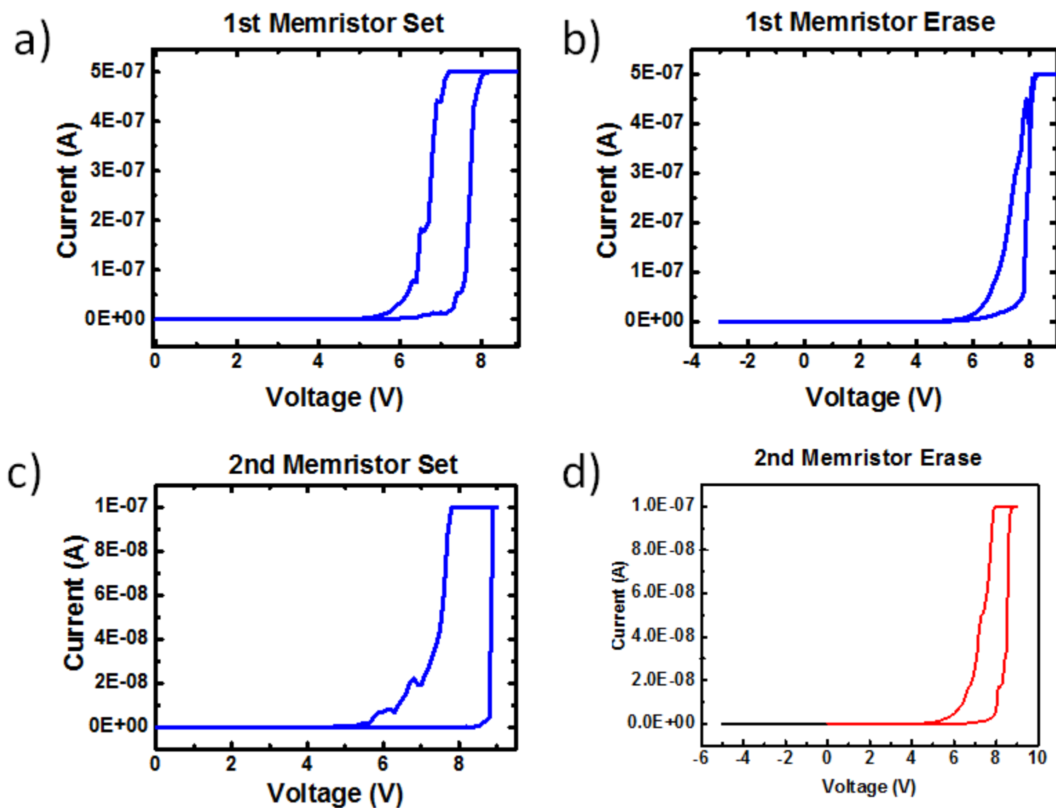

Figure 54: (a) and (c) I-V plot of filament formation for the Memristor which signifies the “01” and “10” state. They show clear hysteresis. (b) I-V plot showing the erase of the two memristor devices.

4.8 Summary

In this chapter we have covered the simulation, physics, fabrication and testing of memristor based optical modulator/encoder. We studied the scattering effect of Ag nanoclusters injected into a-Si photonic crystal waveguide. Among important observations are the enhancement of optical absorption/scattering as the number of nanoclusters increases and the effect of filament separation on optical output patterns. We also observed enhance scattering/absorption as the filament size matches the diameter of the etched holes of the photonic crystal.

From the fabricated device, we observed clear variation of the output optical signal as the filament was formed. The different states “00”, “01”, “10” and “11” were distinguishable. However, the separation between the “01” and “10” states were not as strong as was predicted by the simulation. Also, the device optical output never returned to the pre-filament formation level after multiple filament erase. This implies that some of the nanoclusters were not completely extracted out of the a-Si during the erase stage.

Chapter 5

Conclusion and future work

In this research work, we have demonstrated that Ge nanowires grown on Si substrate can be used to fabricate efficient, nanoscale and CMOS compatible photodetectors with very high current gain and low dark current. Our single nanowire (20nm diameter) photodetector has the highest reported responsivity of any Ge single nanowire detector of similar dimension to the best of my knowledge. We have exploited the effect of surface state on small dimensional structures to achieve very high gain in our detectors. We have shown that our device photocurrent is scalable by the number of active nanowires in the device.

We have also shown that multilevel optical modulator/encoder could be implemented at the device level without the need for complex circuitry. By embedding memristors into a photonic crystal waveguide, it possible to create an asymmetrical device that allows for the decoupling of two coupled optical states, thereby creating an opportunity for future device applications. From the simulation results presented in this thesis, the optical characteristics of a memristive modulator/optical memory readout could be tuned to produce a desired output by simply choosing the location and separation between the memristors along the photonic crystal waveguide. Most importantly, because of the small device dimensions and the low temperature fabrication, this type of optical modulating device could be fabricated from CMOS process for applications in such areas as optical interconnects.

5.1 Nanowire photodetector summary

We fabricated and tested different device structures for Ge nanowire photodetector in the course of our research. Starting with the single nanowire Ge core only device, we were able to demonstrate that efficient photodetectors could be built at scales comparable to current transistor sizes. The most important aspect of the single nanowire device is the possibility of integrating it with other electronic circuits down to the transistor level. Ge is already being used in transistor fabrication and is a well understand material, therefore integration of detectors should be easier to achieve. Another interesting aspect of the single nanowire device is that it outperforms most traditional Ge detectors at 1.55um wavelength. At responsivity of 25A/W, our Ge single nanowire devices can compete favorably with detectors built from exotic materials such as graphene.

Next, we fabricated and tested the Ge/Si core shell device. This device showed enhanced photocurrent about ten times larger than the Ge core only array device. The addition of shell around the Ge nanowire changed the photo detection characteristics of the nanowire. The creation of more surface states from addition of Si shell enhanced the electron trapping effect in the Ge nanowire which led to an increase in the number of free hole carriers with longer lifetime. This increased the performance of the photodetector as is evident in the higher responsivity of 31A/W. However, the increased doping of the nanowires as a result of the Si shell increased the dark current due to tunneling effect at the nanowire/Si substrate heterojunction. We proposed the creation of reduced doping layer at the nanowire/Si heterojunction interface by removing the shell close to junction. We expect this added layer to reduce the leakage current due to tunneling.

Furthermore, we fabricated the P^{+}-Si/P^{+}-Ge/Au (core/shell/Schottky) structure. The reason for this device was to investigate the photo response of Ge nanowire at mid infrared (MIR) frequency range. While the MIR work is still in progress, testing at 1.55um wavelength showed

that this detector has very high photocurrent as well as very high leakage current. The responsivity for this device was extremely high at 539A/W. Due to the very weak Schottky junction at the Ge/Au interface and the biasing condition of this detector, there is a strong field gradient within the entire structure. This made the collection of photo generated carriers more efficient and resulted in the high photocurrent measured from this device. The weak Schottky junction makes this device very leaky and reduces the performance of the detector.

We fabricated and tested the Schottky/Ge hybrid device. Considering the recent demonstration of nanoscale Schottky photodetectors[35], we decided to test the effect of adding Ge nanowires to Schottky photodetectors. The structure was the simplest photodetector we fabricated. We grew Ge nanowires and deposited Ni on top of the nanowires to form both Si/Ge heterojunction and Schottky (Si/Ni) junction. The device structure could be considered as two diodes connected in parallel. What we observed was an increase in photocurrent of close to three orders of magnitude higher than what was measured in the Schottky diode detector. The dark current also increased but the observed photocurrent was more than 3x higher than the dark current. Further optimization could improve the performance of this device.

Lastly, we conducted some experiments to check the contribution of residual absorption in Si substrate to the photocurrent we observed in our devices. First, we built shielded devices where the Si substrate was covered with a thick metal, leaving a small opening for light to pass through. We noticed no change in the performance of the devices before and after the shield was placed. We also built a Schottky diode with platinum metal which forms a barrier of 0.9eV with Si. The metal layer was made thin enough to allow some light to reach the Schottky junction. With the Schottky barrier height higher than the photon energy, any carriers generated must be from the Si substrate and can be extracted by the junction field. The photocurrent from Si absorption was two

orders of magnitude lower than the photocurrent measured in our devices. From these experiments, we conclusively ruled out any significant contribution of the Si substrate to the measured photocurrent.

5.2 Future work

5.2.1 Site controlled nanowire growth

Site controlled Ge nanowire growth without a buffer layer has not been successfully demonstrated. Developing a repeatable site control process that achieves a reasonable nanowire growth yield will be very important not only for integration but also for device engineering in general. For instance, design engineers could easily determine how many nanowires are needed to achieve a particular current level and what the cost is in terms of device area.

We will describe how site controlled nanowire growth can be achieved using the capabilities within an educational research facility. The process could be modified to meet industry fabrication standards. Starting with a clean (111) Si substrate, 10nm of aluminum oxide is deposited as a masking layer. This layer is patterned to create 200nm diameter circular features. The underlying aluminum oxide is wet etched. The proceeding layer is aligned to the previous layer and patterned with 30nm diameter circular features. Using the evaporator and after subsequent BHF dip to remove native oxide, 2nm of Au film is deposited followed by a lift-off. The final result will be patterned 30nm diameter disks that is 2nm thick. Nanowires are grown from the patterned Au film in a CVD chamber. The process flow described is similar to the method used to grow site controlled nanowires in III-V semiconductors.

5.2.2 Ge nanowire modulator

Another interesting work that can be adapted from our current photodetector process is to use the Ge nanowire as a modulator instead of a detector. Considering the large change in the refractive index and absorption coefficient of Ge due to presence of free carries, Ge nanowires grown on Si waveguide will have stronger modulation effect when compared to Si. This is because the absorption coefficient of Ge is already more than two orders of magnitude higher than that of Si at 1.55um wavelength. By injection and extraction of free carriers into the Ge/Si heterojunction by forward/reverse biasing the junction, we might be able to achieve stronger modulation within the silicon waveguide.

Unlike our current photodetector structure, larger Ge nanowires (greater than 100nm diameter) will be required to provide the required absorption volume for reasonable modulation. As a reference to the importance of the proposal here, Si modulators based on free carrier absorption require very long channel in millimeter scale to achieve reasonable light attenuation at 1.55um. For Ge based modulator, this length scale is reduced to about 50um[114] for up to 90% light absorption.

References

[1] G. Chen, H. Chen, M. Haurylau, N. A. Nelson, D. H. Albonesi, P. M. Fauchet, and E. G. Friedman, “Predictions of CMOS compatible on-chip optical interconnect,” *Integr. VLSI J.*, vol. 40, no. 4, pp. 434–446, 2007.

[2] J. Xue, M. Huang, H. Wu, E. Friedman, G. Wicks, D. Moore, A. Garg, B. Ciftcioglu, J. Hu, S. Wang, I. Savidis, M. Jain, R. Berman, and P. Liu, “An intra-chip free-space optical interconnect,” *Proc. 37th Annu. Int. Symp. Comput. Archit. - ISCA ’10*, p. 94, 2010.

[3] K. Ohashi, K. Nishi, T. Shimizu, M. Nakada, J. Fujikata, J. Ushida, S. Toru, K. Nose, M. Mizuno, H. Yukawa, M. Kinoshita, N. Suzuki, A. Gomyo, T. Ishi, D. Okamoto, K. Furue, T. Ueno, T. Tsuchizawa, T. Watanabe, K. Yamada, S. I. Itabashi, and J. Akedo, “On-chip optical interconnect,” *Proc. IEEE*, vol. 97, no. 7, pp. 1186–1196, 2009.

[4] S. Mishra, N. K. Chaudhary, and K. Singh, “Overview of Optical Interconnect Technology,” *Int. J. Sci. Eng. Res.*, vol. 3, no. 4, pp. 1–7, 2012.

[5] I. O’Connor, “Optical solutions for system-level interconnect,” *Proc. 2004 Int. Work. Syst. Lev. interconnect Predict. - SLIP ’04*, p. 79, 2004.

[6] D. R. Selviah, A. C. Walker, D. A. Hutt, K. Wang, A. McCarthy, F. A. Fernández, I. Papakonstantinou, H. Baghsiahi, H. Suyal, M. Taghizadeh, P. Conway, J. Chappell, S. S. Zakariyah, D. Milward, R. Pitwon, K. Hopkins, M. Muggeridge, J. Rygate, J. Calver, W. Kandulski, D. J. Deshazer, K. Hueston, D. J. Ives, R. Ferguson, S. Harris, G. Hinde, M. Cole, H. White, N. Suyal, H. ur Rehman, and C. Bryson, “Integrated optical and electronic interconnect PCB manufacturing research,” *Circuit World*, vol. 36, no. 2, pp. 5–19, 2010.

[7] a. F. Benner, M. Ignatowski, J. a. Kash, D. M. Kuchta, and M. B. Ritter, “Exploitation of optical interconnects in future server architectures,” *IBM J. Res. Dev.*, vol. 49, no. 4, pp. 755–775, 2005.

[8] I. A. Young, E. Mohammed, J. T. S. Liao, A. M. Kern, S. Palermo, B. A. Block, M. R. Reshotko, and P. L. D. Chang, “Optical I/O technology for tera-scale computing,” in *IEEE Journal of Solid-State Circuits*, 2010, vol. 45, no. 1, pp. 235–248.

[9] S. Mishra, N. K. Chaudhary, and K. Singh, “Overview of Optical Interconnect Technology,” *Int. J. Sci. Eng. Res.*, vol. 3, no. 4, pp. 390–396, 2012.

[10] D. Van Thourhout, T. Spuesens, S. K. Selvaraja, L. Liu, G. Roelkens, R. Kumar, G. Morthier, P. Rojo-Romeo, F. Mandorlo, P. Regreny, O. Raz, C. Kopp, and L. Grenouillet, “Nanophotonic devices for optical interconnect,” *IEEE J. Sel. Top. Quantum Electron.*, vol. 16, no. 5, pp. 1363–1375, 2010.

[11] M. Haurylau, G. Chen, H. Chen, J. Zhang, N. A. Nelson, D. H. Albonesi, E. G. Friedman,

and P. M. Fauchet, “On-chip optical interconnect roadmap: Challenges and critical directions,” *IEEE J. Sel. Top. Quantum Electron.*, vol. 12, no. 6, pp. 1699–1704, 2006.

[12] A. Benner, “Optical Interconnect Opportunities in Supercomputers and High End Computing - OSA Technical Digest,” *Opt. Fiber Commun. Conf.*, no. March, p. OTu2B.4, 2012.

[13] R. G. Beausoleil, P. J. Kuekes, G. S. Snider, S. Y. Wang, and R. S. Williams, “Nanoelectronic and nanophotonic interconnect,” *Proc. IEEE*, vol. 96, no. 2, pp. 230–247, 2008.

[14] J. Singh, *Optoelectronics: An introduction to materials and devices*. McGraw-Hill College, 1996.

[15] S. L. Chuang, “Physics of Photonic Devices,” *Phys. Photonic Devices*, p. p.113, 2009.

[16] J. Li, Y. Zhang, S. To, L. You, and Y. Sun, “Effect of nanowire number, diameter, and doping density on nano-FET biosensor sensitivity,” *ACS Nano*, vol. 5, no. 8, pp. 6661–6668, 2011.

[17] J. Appenzeller, J. Knoch, M. T. Björk, H. Riel, H. Schmid, and W. Riess, “Toward nanowire electronics,” *IEEE Trans. Electron Devices*, vol. 55, no. 11, pp. 2827–2845, 2008.

[18] K. Keem, D. Y. Jeong, S. Kim, M. S. Lee, I. S. Yeo, U. I. Chung, and J. T. Moon, “Fabrication and device characterization of omega-shaped-gate ZnO nanowire field-effect transistors,” *Nano Lett.*, vol. 6, no. 7, pp. 1454–1458, 2006.

[19] M. Shin, “Efficient simulation of silicon nanowire field effect transistors and their scaling behavior,” *J. Appl. Phys.*, vol. 101, no. 2, 2007.

[20] Y. Cui, Z. Zhong, D. Wang, W. U. Wang, and C. M. Lieber, “High performance silicon nanowire field effect transistors,” *Nano Lett.*, vol. 3, no. 2, pp. 149–152, 2003.

[21] Z.-M. Liao, K.-J. Liu, J.-M. Zhang, J. Xu, and D.-P. Yu, “Effect of surface states on electron transport in individual ZnO nanowires,” *Phys. Lett. A*, vol. 367, no. 3, pp. 207–210, 2007.

[22] C. Pfüller, O. Brandt, F. Grosse, T. Flissikowski, C. Chèze, V. Consonni, L. Geelhaar, H. T. Grahn, and H. Riechert, “Unpinning the Fermi level of GaN nanowires by ultraviolet radiation,” *Phys. Rev. B - Condens. Matter Mater. Phys.*, vol. 82, no. 4, 2010.

[23] O. Demichel, M. Heiss, J. Bleuse, H. Mariette, and I. A. Fontcuberta Morral, “Impact of surfaces on the optical properties of GaAs nanowires,” *Appl. Phys. Lett.*, vol. 97, no. 20, 2010.

[24] S. Zhao, S. Fathololoumi, K. H. Bevan, D. P. Liu, M. G. Kibria, Q. Li, G. T. Wang, H. Guo, and Z. Mi, “Tuning the surface charge properties of epitaxial InN nanowires,” *Nano Lett.*, vol. 12, no. 6, pp. 2877–2882, 2012.

[25] C. K. Yong, K. Noori, Q. Gao, H. J. Joyce, H. H. Tan, C. Jagadish, F. Giustino, M. B. Johnston, and L. M. Herz, “Strong carrier lifetime enhancement in GaAs nanowires coated

with semiconducting polymer," *Nano Lett.*, vol. 12, no. 12, pp. 6293–6301, 2012.

[26] B. H. Le, S. Zhao, N. H. Tran, T. Szkopek, and Z. Mi, "On the Fermi-level pinning of InN grown surfaces," *Appl. Phys. Express*, vol. 8, no. 6, p. 061001, 2015.

[27] C.-H. Lee, C. S. Ritz, M. Huang, M. W. Ziwisky, R. J. Blise, and M. G. Lagally, "Integrated freestanding single-crystal silicon nanowires: conductivity and surface treatment.," *Nanotechnology*, vol. 22, no. 5, p. 055704, 2011.

[28] C. Y. Chen, J. R. D. Retamal, I. W. Wu, D. H. Lien, M. W. Chen, Y. Ding, Y. L. Chueh, C. I. Wu, and J. H. He, "Probing surface band bending of surface-engineered metal oxide nanowires," *ACS Nano*, vol. 6, no. 11, pp. 9366–9372, 2012.

[29] D. Wang and H. Dai, "Germanium nanowires: From synthesis, surface chemistry, and assembly to devices," *Appl. Phys. A Mater. Sci. Process.*, vol. 85, no. 3, pp. 217–225, 2006.

[30] Z. M. Liao, H. Z. Zhang, Y. B. Zhou, J. Xu, J. M. Zhang, and D. P. Yu, "Surface effects on photoluminescence of single ZnO nanowires," *Phys. Lett. Sect. A Gen. At. Solid State Phys.*, vol. 372, no. 24, pp. 4505–4509, 2008.

[31] E. Stern, G. Cheng, E. Cimpoiasu, R. Klie, S. Guthrie, J. Klemic, I. Kretzschmar, E. Steinlauf, D. Turner-Evans, E. Broomfield, J. Hyland, R. Koudelka, T. Boone, M. Young, a Sanders, R. Munden, T. Lee, D. Routenberg, and M. a Reed, "Electrical characterization of single GaN nanowires," *Nanotechnology*, vol. 16, no. 12, pp. 2941–2953, 2005.

[32] I. Shalish, H. Temkin, and V. Narayanamurti, "Size-dependent surface luminescence in ZnO nanowires," *Phys. Rev. B - Condens. Matter Mater. Phys.*, vol. 69, no. 24, 2004.

[33] C. Soci, A. Zhang, B. Xiang, S. A. Dayeh, D. P. R. Aplin, J. Park, X. Y. Bao, Y. H. Lo, and D. Wang, "ZnO nanowire UV photodetectors with high internal gain," *Nano Lett.*, vol. 7, no. 4, pp. 1003–1009, 2007.

[34] U. Mishra and J. Singh, *Semiconductor Device Physics and Design*. 2007.

[35] "Locally oxidized silicon surface-plasmon Schottky detector for telecom regime.," *Nano Lett.*, vol. 11, no. 6, pp. 2219–2224, 2011.

[36] S. M. Sze and K. K. Ng, *Physics of Semiconductor Devices*. 2007.

[37] A. Yariv and A. Yariv, "Optical Electronics in Modern Communications, 5th ed," *New York Oxford Univ. Press*, pp. 404–407, 1997.

[38] H. Haus, "Waves and Fields in Optoelectronics," *Prentice-Hall*, vol. 32, no. 7. pp. 748–748, 1985.

[39] K. Tharmalingam, "Optical absorption in the presence of a uniform field," *Phys. Rev.*, vol. 130, no. 6, pp. 2204–2206, 1963.

[40] L. . Keldysh, "The effect of a strong electric field on the optical properties of insulating crystals," *Sov. Phys. JETP 34*, pp. 788–790, 1958.

[41] G. T. Reed, G. Mashanovich, F. Y. Gardes, and D. J. Thomson, "Silicon optical

modulators," *Nat. Photonics*, vol. 4, no. 8, pp. 518–526, 2010.

[42] G. V. Treyz, J. M. Halbout, and P. G. May, "Silicon Optical Modulators at 1.3 μm Based on Free-Carrier Absorption," *IEEE Electron Device Lett.*, vol. 12, no. 6, pp. 276–278, 1991.

[43] R. A. Soref and B. R. Bennett, "Electrooptical effects in silicon," *IEEE Journal of Quantum Electronics*, vol. 23, no. 1. pp. 123–129, 1987.

[44] A. Emboras, I. Goykhman, B. Desiatov, N. Mazurski, L. Stern, J. Shappir, and U. Levy, "Nanoscale plasmonic memristor with optical readout functionality," *Nano Lett.*, vol. 13, no. 12, pp. 6151–6155, 2013.

[45] A. H. Kahn, "Theory of the infrared absorption of carriers in germanium and silicon," *Phys. Rev.*, vol. 97, no. 6, pp. 1647–1652, 1955.

[46] W. Kaiser, R. J. Collins, and H. Y. Fan, "Infrared absorption in p-type germanium," *Phys. Rev.*, vol. 91, no. 6, pp. 1380–1381, 1953.

[47] R. Newman and W. W. Tyler, "Effect of impurities on free-hole infrared absorption in p-type germanium," *Phys. Rev.*, vol. 105, no. 3, pp. 885–886, 1957.

[48] J. Tauc, R. Grigorovici, and A. Vancu, "Optical Properties and Electronic Structure of Amorphous Germanium," *Phys. Status Solidi*, vol. 15, no. 2, pp. 627–637, 1966.

[49] "No Title." [Online]. Available: http://www.ioffe.ru/SVA/NSM/Semicond/Ge/Figs/221.gif.

[50] W. Y. Fung, "Applications of Semiconductor Nanowires for Nanoelectronics and Nanoelectromechanical Systems," University of Michigan, 2012.

[51] J. H. Kim, S. R. Moon, H. S. Yoon, J. H. Jung, Y. Kim, Z. G. Chen, J. Zou, D. Y. Choi, H. J. Joyce, Q. Gao, H. H. Tan, and C. Jagadish, "Taper-free and vertically oriented Ge nanowires on Ge/Si substrates grown by a two-temperature process," *Cryst. Growth Des.*, vol. 12, no. 1, pp. 135–141, 2012.

[52] L. Chen, W. Y. Fung, and W. Lu, "Vertical nanowire heterojunction devices based on a clean Si/Ge interface," *Nano Lett.*, vol. 13, no. 11, pp. 5521–5527, 2013.

[53] L. Chen, W. D. Lu, and C. M. Lieber, "Semiconductor Nanowire Growth and Integration," *RSC Smart Mater.*, no. 11, pp. 1–53, 2015.

[54] J. H. Woodruff, J. B. Ratchford, I. A. Goldthorpe, P. C. McIntyre, and C. E. D. Chidsey, "Vertically oriented germanium nanowires grown from gold colloids on silicon substrates and subsequent gold removal," *Nano Lett.*, vol. 7, no. 6, pp. 1637–1642, 2007.

[55] I. A. Goldthorpe, A. F. Marshall, and P. C. McIntyre, "Inhibiting strain-induced surface roughening: Dislocation-free Ge/Si and Ge/SiGe core-shell nanowires references," *Nano Lett.*, vol. 9, no. 11, pp. 3715–3719, 2009.

[56] V. Schmidt, S. Senz, and U. Gösele, "Diameter-dependent growth direction of epitaxial silicon nanowires," *Nano Lett.*, vol. 5, no. 5, pp. 931–935, 2005.

[57] R. P. Prasankumar, S. Choi, S. A. Trugman, S. T. Picraux, and A. J. Taylor, “Ultrafast electron and hole dynamics in germanium nanowires,” *Nano Lett.*, vol. 8, no. 6, pp. 1619–1624, 2008.

[58] P. C. Eng, S. Song, and B. Ping, “State-of-the-art photodetectors for optoelectronic integration at telecommunication wavelength,” *Nanophotonics*, vol. 4, no. 1, pp. 277–302, 2015.

[59] M. Hu, K. P. Giapis, J. V Goicochea, X. Zhang, and D. Poulikakos, “Significant Reduction of Thermal Conductivity in Si/Ge Core- Shell Nanowires,” *Nano Lett.*, vol. 11, no. 2, pp. 618–623, 2010.

[60] D. Li, Y. Wu, R. Fan, P. Yang, and A. Majumdar, “Thermal conductivity of Si/SiGe superlattice nanowires,” *Appl. Phys. Lett.*, vol. 83, no. 15, pp. 3186–3188, 2003.

[61] N. Mingo, L. Yang, D. Li, and A. Majumdar, “Predicting the Thermal Conductivity of Si and Ge Nanowires,” *Nano Lett.*, vol. 3, no. 12, pp. 1713–1716, 2003.

[62] R. Yang, G. Chen, and M. S. Dresselhaus, “Thermal conductivity modeling of core-shell and tubular nanowires,” *Nano Lett.*, vol. 5, no. 6, pp. 1111–1115, 2005.

[63] C. J. Kim, H. S. Lee, Y. J. Cho, K. Kang, and M. H. Jo, “Diameter-dependent internal gain in ohmic Ge nanowire photodetectors,” *Nano Lett.*, vol. 10, no. 6, pp. 2043–2048, 2010.

[64] J. Xiang, W. Lu, Y. Hu, Y. Wu, H. Yan, and C. M. Lieber, “Ge/Si nanowire heterostructures as high-performance field-effect transistors.,” *Nature*, vol. 441, no. 7092, pp. 489–493, 2006.

[65] Z. Sheng, L. Liu, J. Brouckaert, S. He, and D. Van Thourhout, “InGaAs PIN photodetectors integrated on silicon-on-insulator waveguides.,” *Opt. Express*, vol. 18, no. 2, pp. 1756–1761, 2010.

[66] S. Feng, Y. Geng, K. M. Lau, and A. W. Poon, “Epitaxial III-V-on-silicon waveguide butt-coupled photodetectors,” in *IEEE International Conference on Group IV Photonics GFP*, 2012, pp. 51–53.

[67] J. H. Kim, H. T. Griem, R. A. Friedman, E. Y. Chan, and S. Ray, “High-performance back-illuminated InGaAs/InAlAs MSM photodetector with a record responsivity of 0.96 A/W,” *IEEE Photonics Technol. Lett.*, vol. 4, no. 11, pp. 1241–1244, 1992.

[68] Y. Cheng, Y. Ikku, M. Takenaka, and S. Takagi, “InGaAs MSM photodetector monolithically integrated with InP photonic-wire waveguide on III-V CMOS photonics platform,” *IEICE Electron. Express*, vol. 11, no. 16, pp. 1–8, 2014.

[69] T. K. Watanabe I., Sugou S., Ishikawa H., Anan T., Makita K., Tsuji M., “High-speed and low-darkcurrent flip-chip In-AlAs/InAlGaAs quaternary well superlattice APDs with 120 GHz gain-bandwidth produc,” *IEEE Phot. Technol. Lett.*, 1993.

[70] M. Nada, H. Yokoyama, Y. Muramoto, T. Ishibashi, and H. Matsuzaki, “A 50-Gbit/s vertical illumination avalanche photodiode for 400-Gbit/s Ethernet systems,” *Opt. Express*, vol. 22, no. 12, p. 14681, 2014.

[71] D. Ahn, C.-Y. Hong, J. Liu, W. Giziewicz, M. Beals, L. C. Kimerling, J. Michel, J. Chen, and F. X. Kärtner, "High performance, waveguide integrated Ge photodetectors.," *Opt. Express*, vol. 15, no. 7, pp. 3916–3921, 2007.

[72] D. Zhang, C. Xue, B. Cheng, S. Su, Z. Liu, X. Zhang, G. Zhang, C. Li, and Q. Wang, "High-responsivity GeSn short-wave infrared p-i-n photodetectors," *Appl. Phys. Lett.*, vol. 102, no. 14, 2013.

[73] K. D. L. Ang K.W., Zhu S.Y., Wang J., Chua K.T., Yu M.B., Lo G.Q., "Novel Silicon-Carbon (Si:C) Schottky barrier enhancement layer for dark-current suppression in Ge-on-SOI MSM photodetectors," *IEEE Electron Device Lett.*, vol. 7, pp. 704–707, 2008.

[74] N. C. Harris, T. Baehr-Jones, A. E. J. Lim, T. Y. Liow, G. Q. Lo, and M. Hochberg, "Noise characterization of a waveguide-coupled MSM photodetector exceeding unity quantum efficiency," *J. Light. Technol.*, vol. 31, no. 1, pp. 23–27, 2013.

[75] Y. Kang, H.-D. Liu, M. Morse, M. J. Paniccia, M. Zadka, S. Litski, G. Sarid, A. Pauchard, Y.-H. Kuo, H.-W. Chen, W. S. Zaoui, J. E. Bowers, A. Beling, D. C. McIntosh, X. Zheng, and J. C. Campbell, "Monolithic germanium/silicon avalanche photodiodes with 340 GHz gain–bandwidth product," *Nat. Photonics*, vol. 3, no. 1, pp. 59–63, 2009.

[76] I. G. Kim, K. Jang, J. Joo, S. Kim, S. Kim, K. Choi, J. H. Oh, S. A. Kim, and G. Kim, "High-performance photoreceivers based on vertical-illumination type Ge-on-Si photodetectors operating up to 43 Gb/s at λ~1550nm," *Opt. Express*, vol. 21, no. 25, p. 30716, 2013.

[77] M. W. Geis, S. J. Spector, M. E. Grein, J. U. Yoon, D. M. Lennon, and T. M. Lyszczarz, "Silicon waveguide infrared photodiodes with >35 GHz bandwidth and phototransistors with 50 AW-1 response.," *Opt. Express*, vol. 17, no. 7, pp. 5193–5204, 2009.

[78] R. R. Grote, K. Padmaraju, B. Souhan, J. B. Driscoll, K. Bergman, and R. M. Osgood, "10 Gb/s error-free operation of all-silicon ion-implanted-waveguide photodiodes at 1.55 ??m," *IEEE Photonics Technol. Lett.*, vol. 25, no. 1, pp. 67–70, 2013.

[79] T. Baehr-Jones, M. Hochberg, and a Scherer, "Photodetection in silicon beyond the band edge with surface states.," *Opt. Express*, vol. 16, no. 3, pp. 1659–1668, 2008.

[80] H. Chen, X. Luo, and A. W. Poon, "Cavity-enhanced photocurrent generation by 1.55 ??m wavelengths linear absorption in a p-i-n diode embedded silicon microring resonator," *Appl. Phys. Lett.*, vol. 95, no. 17, pp. 2007–2010, 2009.

[81] S. Zhu, G. Q. Lo, M. B. Yu, and D. L. Kwong, "Low-cost and high-gain silicide Schottky-barrier collector phototransistor integrated on Si waveguide for infrared detection," *Appl. Phys. Lett.*, vol. 93, no. 7, pp. 2006–2009, 2008.

[82] M. Casalino, L. Sirleto, M. Iodice, N. Saffioti, M. Gioffr??, I. Rendina, and G. Coppola, "Cu/p-Si Schottky barrier-based near infrared photodetector integrated with a silicon-on-insulator waveguide," *Appl. Phys. Lett.*, vol. 96, no. 24, pp. 2008–2011, 2010.

[83] O. K. Wu, R. D. Rajavel, T. J. De Lyon, J. E. Jensen, M. D. Jack, K. Kosai, G. R. Chapman, S. Sen, B. A. Baumgratz, B. Walker, and B. Johnson, "MBE-grown HgCdTe multi-layer heterojunction structures for high speed low-noise 1.3-1.6 ?m avalanche

photodetectors," *J. Electron. Mater.*, vol. 26, no. 6, pp. 488–492, 1997.

[84] P. Norton, "HgCdTe infrared detectorsTitle," *Opto-electron. Rev*, vol. 10, pp. 159–174, 2002.

[85] F. Xia, T. Mueller, Y. Lin, A. Valdes-Garcia, and P. Avouris, "Ultrafast graphene photodetector," *Nat. Nanotechnol.*, vol. 4, no. 12, pp. 839–843, 2009.

[86] G. Konstantatos, M. Badioli, L. Gaudreau, J. Osmond, M. Bernechea, F. P. G. de Arquer, F. Gatti, and F. H. L. Koppens, "Hybrid graphene–quantum dot phototransistors with ultrahigh gain," *Nat. Nanotechnol.*, vol. 7, no. 6, pp. 363–368, 2012.

[87] C. O. Kim, S. Kim, D. H. Shin, S. S. Kang, J. M. Kim, C. W. Jang, S. S. Joo, J. S. Lee, J. H. Kim, S.-H. Choi, and E. Hwang, "High photoresponsivity in an all-graphene p-n vertical junction photodetector.," *Nat. Commun.*, vol. 5, p. 3249, 2014.

[88] B. C. St-Antoine, D. M??nard, and R. Martel, "Single-walled carbon nanotube thermopile for broadband light detection," *Nano Lett.*, vol. 11, no. 2, pp. 609–613, 2011.

[89] M. S. Arnold, J. D. Zimmerman, C. K. Renshaw, X. Xu, R. R. Lunt, C. M. Austin, and S. R. Forrest, "Broad spectral response using carbon nanotube/organic semiconductor/C60 photodetectors.," *Nano Lett.*, vol. 9, no. 9, pp. 3354–3358, 2009.

[90] G. Konstantatos, I. Howard, A. Fischer, S. Hoogland, J. Clifford, E. Klem, L. Levina, and E. H. Sargent, "Ultrasensitive solution-cast quantum dot photodetectors.," *Nature*, vol. 442, no. 7099, pp. 180–183, 2006.

[91] J. P. Clifford, G. Konstantatos, K. W. Johnston, S. Hoogland, L. Levina, and E. H. Sargent, "Fast, sensitive and spectrally tuneable colloidal-quantum-dot photodetectors.," *Nat. Nanotechnol.*, vol. 4, no. 1, pp. 40–44, 2009.

[92] F. F. Ren, K. W. Ang, J. Song, Q. Fang, M. Yu, G. Q. Lo, and D. L. Kwong, "Surface plasmon enhanced responsivity in a waveguided germanium metal-semiconductor-metal photodetector," *Appl. Phys. Lett.*, vol. 97, no. 9, pp. 1–4, 2010.

[93] M. Gu, P. Bai, H. S. Chu, and E. P. Li, "Design of subwavelength CMOS compatible plasmonic photodetector for nano-electronic-photonic integrated circuits," *IEEE Photonics Technol. Lett.*, vol. 24, no. 6, pp. 515–517, 2012.

[94] F. Wang and N. A. Melosh, "Plasmonic energy collection through hot carrier extraction," *Nano Lett.*, vol. 11, no. 12, pp. 5426–5430, 2011.

[95] J. Kash, "Optical/electrical technologies for high speed signal communications in high performance servers," in *OFC/NFOEC 2008 - 2008 Conference on Optical Fiber Communication/National Fiber Optic Engineers Conference*, 2008.

[96] Y. Tang, K. Shinohara, D. Regan, A. Corrion, D. Brown, J. Wong, A. Schmitz, H. Fung, S. Kim, and M. Micovic, "Ultrahigh-Speed GaN High-Electron-Mobility Transistors With f T / f max of 454/444 GHz," *IEEE Electron Device Lett.*, vol. 36, no. 6, pp. 549–551, 2015.

[97] Y. Li, R. Clady, A. F. Marshall, J. Park, S. V. Thombare, G. Chan, T. W. Schmidt, M. L.

Brongersma, and P. C. McIntyre, “Ultrafast Carrier Dynamics of a Photo-Excited Germanium Nanowire-Air Metamaterial,” *ACS Photonics*, vol. 2, no. 8, pp. 1091–1098, 2015.

[98] A. Emboras, C. Hoessbacher, C. Haffner, W. Heni, U. Koch, P. Ma, Y. Fedoryshyn, J. Niegemann, C. Hafner, and J. Leuthold, “Electrically controlled plasmonic switches and modulators,” *IEEE J. Sel. Top. Quantum Electron.*, vol. 21, no. 4, 2015.

[99] A. Liu, R. Jones, L. Liao, and D. Samara-rubio, “A high-speed silicon optical modulator based on a metal – oxide – semiconductor capacitor,” *Nature*, vol. 427, no. February, pp. 615–619, 2004.

[100] Y. Yu, Y. Chen, H. Hu, W. Xue, K. Yvind, and J. Mørk, “Nonreciprocal transmission in a photonic-crystal Fano structure enabled by symmetry breaking,” p. 1409.3147, 2014.

[101] J. Zhou, F. Cai, Q. Wang, B. Chen, S. Gaba, and W. D. Lu, “Very low-programming-current RRAM with self-rectifying characteristics,” *IEEE Electron Device Lett.*, vol. 37, no. 4, pp. 404–407, 2016.

[102] Y. Yang, P. Gao, S. Gaba, T. Chang, X. Pan, and W. Lu, “Observation of conducting filament growth in nanoscale resistive memories,” *Nat. Commun.*, vol. 3, p. 732, 2012.

[103] K. H. Kim, S. Hyun Jo, S. Gaba, and W. Lu, “Nanoscale resistive memory with intrinsic diode characteristics and long endurance,” *Appl. Phys. Lett.*, vol. 96, no. 5, 2010.

[104] P. B. Johnson and R. W. Christy, “Optical constants of the noble metals,” *Physical Review B*, vol. 6, no. 12. pp. 4370–4379, 1972.

[105] “No Title.” Lumerical Solutions, Inc.

[106] L. Novotny, *Principles of Nano-Optics*, vol. 1, no. 4. 2006.

[107] M. Kerker, *The Scattering of Light and Other Electromagnetic Radiation*, vol. 7. 1969.

[108] B. Hecht, H. Bielefeldt, L. Novotny, Y. Inouye, and D. Pohl, “Local Excitation, Scattering, and Interference of Surface Plasmons,” *Phys. Rev. Lett.*, vol. 77, no. 9, pp. 1889–1892, 1996.

[109] H. Raether, “Surface Plasmons on Smooth and Rough Surfaces and on Gratings,” *Springer Tracts in Modern Physics*, vol. 111. p. 136, 1988.

[110] L. Novotny, B. Hecht, D. W. Pohl, and I. Introduction, “Interference of locally excited surface plasmons,” *J. Appl. Phys.*, vol. 81, no. 1997, pp. 1798–1806, 1997.

[111] D. M. Schaadt, B. Feng, and E. T. Yu, “Enhanced semiconductor optical absorption via surface plasmon excitation in metal nanoparticles,” *Appl. Phys. Lett.*, vol. 86, no. 6, pp. 1–3, 2005.

[112] Y. Dong, G. Yu, M. C. McAlpine, W. Lu, and C. M. Lieber, “Si/a-Si core/shell nanowires as nonvolatile crossbar switches,” *Nano Lett.*, vol. 8, no. 2, pp. 386–391, 2008.

[113] K.-H. Kim, S. Gaba, D. Wheeler, J. M. Cruz-Albrecht, T. Hussain, N. Srinivasa, and W. Lu, “A Functional Hybrid Memristor Crossbar-Array/CMOS System for Data Storage and

Neuromorphic Applications," *Nano Lett.*, vol. 12, no. 1, pp. 389–395, 2011.

[114] R. K. Schaevitz, E. H. Edwards, J. E. Roth, E. T. Fei, Y. Rong, P. Wahl, T. I. Kamins, J. S. Harris, and D. A. B. Miller, "Simple electroabsorption calculator for designing 1310 nm and 1550 nm modulators using germanium quantum wells," *IEEE J. Quantum Electron.*, vol. 48, no. 2, pp. 187–197, 2012.